國立交通大學

物理研究所

博士論文

單層石墨層在調制場之下的電子特性和光學性質

Electronic and Optical Properties of a Single-layer Graphene in Spatially Modulated Fields

研　　究　　生： 邱裕煌 (Yu-Huang Chiu)

指 導　教 授： 褚德三 (Der-San Chuu)

共同指導教授： 林明發 (Ming-Fa Lin)

中華民國九十七年七月二十一日

誌謝

本篇論文的完成要感謝許多人的支持與幫助。首先要感謝褚德三老師在這麼多年以來對我的指導，尤其是他給予我許多包容與耐心，即使在我表現很差的時候，他仍然支持我，依舊相信我有能力完成我的博士論文。其次要感謝成大物理系教授林明發，他給予我論文上面的指導與幫助讓我受益良多，也因為他的鞭策才讓我得以在論文上面有所成就。另外，台南科技大學張振鵬老師以及我的博士班同學林高進博士時常給予我意見和討論，這些寶貴建議也讓我從中獲益許多。交大的夥伴們，岳男、英彥、英瓚、瑞雯、奎霖和光胤，因為你們的陪伴讓我不孤單。彥宏、思超、啟玄、子軒、兆穎、奕豪、琪朗、炯煦、志偉、峻儀以及元正大哥，有你們在成大給予的幫助才能讓我的論文得以順利完成。

最後要感謝我的家人以及身邊的好友們，你們一路的支持與陪伴給予了我莫大的動力。尤其是我的母親，她從小到大對於我所做的一切都盡力支持，也因為她的教導，讓我不至於誤入歧途，讓我能夠有機會完成我的博士學位。在我想放棄的時候，大家給我安慰和鼓勵；在我失意的時候，你們陪我一起度過低潮。博士班的這條路上，沒有你們，我無法順利完成。未來的人生道路上，我仍然需要你們的陪伴。在此，僅以這篇論文獻上我對你們的敬意。

摘要

這篇論文之中，我們以緊束模型及梯度近似法研究單層石墨系統在外加調制磁場和調制電場之下的電子和光譜特性。對於調制磁場而言，電子性質受到它的強烈影響而改變，這些改變包括能帶維度、能量色散關係、新的能量邊界態、能帶非對稱性、能帶簡併度以及能帶的非等方性特質。在能帶結構中，費米能為零的地方將會有局部平坦的能帶出現，而在其他能量對應的則是一維的拋物線能帶。這兩種能帶在態密度中分別造成零維對稱和一維非對稱的發散峰。對於每一條拋物線能帶而言，它具有一個原始邊界態和四個額外邊界態。這些邊界態所對應的能量和調制週期以及調制磁場強度之間的關係都有詳細的討論與分析。另外，在光學吸收譜中的吸收峰主要來自於原始邊界態和額外邊界態所產生。這兩種邊界態對應的吸收峰分別遵守不同的光學選擇律，其主要原因是由於它們的波函數擁有不同的特徵所造成。特別值得注意的是，光學吸收譜可以反應出調制磁場方向以及外加光的極化方向所造成的非等方性特質。對於調制電場而言，電子特性以及光學特性也會受到強烈的影響。在能帶結構中，靠近原始邊界態的能帶具有數個額外邊界態，並且展現出震盪行為和色散關係。另外，原本在沒有外加場之下的雙重簡併拋物線能帶變成沒有簡併的震盪能帶。態密度中所產生的一維非對稱峰主要是來自於額外邊界態。值得一提的是，態密度中對應費米能為零的有限值代表著自由電子的存在。換句話說，藉由調制電場的影響可以將單層石墨系統從半導體性變成金屬性的系統。對於光學性質而言，同樣的也展現了許多來自於額外邊界態所產生的吸收峰。然而，這些吸收峰並沒有展現出一個明確的光學選擇律。

Abstract

The π-electronic structures and optical absorption spectra of a single-layer graphene in spatially modulated magnetic and electric fields are studied by the tight-binding model and gradient approximation. For modulated magnetic fields, they could strongly affect the low-energy electronic properties, i.e., the dimensionality, energy dispersions, extra band-edge states, asymmetry, state degeneracy, and anisotropy of energy bands. There are partial flat bands at E_F=0 and one-dimensional parabolic bands at others. The two kinds of bands make density of states (DOS) exhibit a delta-function-like structure and asymmetric prominent peaks, respectively. Each parabolic band owns one original (k_y^{pp}) and four extra (k_y^{sp}'s) band-edge states, and their energy dependences on the period and strength are investigated in detail. In the optical absorption spectra, the absorption peaks originating in k_y^{pp} and k_y^{sp}'s obey different selection rules because their wave functions present different features. It is noted that the anisotropic absorption spectra are induced by different modulated directions and electric polarization directions. For modulated electric fields, they could drastically change the low-frequency electronic and optical properties. Each energy band displays oscillatory energy dispersions and several band-edge states near k_y^{pp}. The doubly degenerate parabolic bands become nondegenerate. DOS shows many prominent asymmetric peaks mainly owing to the band-edge states. The finite DOS at E_F =0 means that there are free carriers, i.e., a modulated electric field could change a semiconducting graphene into a semimetallic one. The optical absorption spectra demonstrate rich peaks resulting from band-edge states, and reveal the anisotropy in the modulated direction. Such absorption peaks could not be ascribed to an obvious selection rule.

TABLE OF CONTENTS

Chapter 1

Introduction

The bulk graphite is extensively studied in both theoretical calculations [1-4] and experimental measurements [5-9]. Recently, few-layer graphenes with two-dimensional (2D) hexagonal symmetry and nanoscaled thickness have been produced by the mechanical friction [10,11] and thermal decomposition [12,13]. Such systems are very appropriate in studying 2D physical properties. They have aroused a lot of investigations on band structures [14-31], electronic excitations [32-35], phonon [36], transport properties [37-44], and optical spectra [14,45-51].

The geometric symmetry configurations have a profound influence on the electronic properties of few-layer graphenes. The honeycomb structure causes a single-layer graphene to exhibit two linear bands intersecting at the Fermi level $E_F = 0$. The low-energy bands could be described by the fermion Dirac equation [16]. Energy bands are isotropic at low energy ($\leq$ 0.5 eV) [1], and so are the low-frequency physical properties (e.g. Coulomb excitations) [32,34]. The vanishing density of states (DOS) at the Fermi level means that a graphene monolayer is an exotic zero-gap semiconductor. The massless Dirac electrons have been examined by using a combination of optical microscopy, scanning electron microscopy and atomic-force microscopy [11], and by the angle-resolved photoelectron spectroscopy [52].

The external electric [10,11] and magnetic fields [10,11,13,14,29,31,45,47,51] strongly affect the electronic properties of a graphene monolayer. A uniform perpendicular magnetic field makes the low-frequency energy bands become the dispersionless Landau levels (LLs),

and thus induces the novel half-integer quantum Hall effect [11,37]. The low-energy LLs can be represented by a simple square-root form $E_n \propto \sqrt{|n|\, B_0}$ (n the integer quantum and B_0 the field strength) [16,53]. The dependence on B_0 has been identified by the magneto-optical experiments of cyclotron resonance [47]. Meanwhile, an inhomogeneous magnetic field might also strongly influence the essential physical properties. Haldane, for example, concluded that a 2D graphene could exhibit magnetoconductance in the presence of a vanishing net magnetic field [54].

There are several studies on the optical absorption spectra of a graphene monolayer. The low-energy absorption spectra do not exhibit any absorption peaks by the theoretical prediction [14], which is dominated by the density of states. On the other hand, a uniform perpendicular magnetic field could lead to many delta-function-like absorption peaks originating in LLs at low energy. These peaks result from the vertical excitations between the nth ($(n+1)$th) occupied LLs and the $(n+1)$th (nth) unoccupied LLs. Such peaks obey the specific selection rule $|\triangle n| = 1$ because the wave functions (Ψ_n's) own the spatial symmetry configuration [16]. Ψ_n is characterized by the product of the nth order Hermite polynomial and Gaussian function, as seen in a two-dimensional electron gas (2DEG). The optical selection has been confirmed by the far infrared transmission experiments [45].

The physical properties of a 2DEG in the presence of a spatially modulated magnetic field have been attracted numerous experimental [55-58] and theoretical [59-67] investigations. These works primarily focus on the transport properties [55-57,59,60], energy bands [61-63], electronic excitations [64-67], and optical spectra [58]. The transport measurements reveal the oscillatory magnetoresistance [55,56]. Energy bands of a 2DEG in the absence of external fields have parabolic energy dispersions. A periodic magnetic field results in

drastic changes in the state degeneracy, band-edge states, and curvatures. In contrast, only few examine the physical properties of a single-layer graphene under a modulated magnetic field. Given the gap, we are motivated to investigate the magnetoelectronic and magneto-optical properties of a graphene monolayer in a modulated magnetic field.

The purpose of this dissertation is to investigate how modulated fields affect the physical properties of a single-layer graphene. At first, for modulated magnetic fields, the magnetoelectronic properties are calculated by the Peierls tight-binding model. The influence of such fields, including the energy dispersions, reduction of dimensionality, creation of extra band-edge states, change of state degeneracy, anisotropy at low energy, and asymmetry of energy bands, are studied (Chapter 2). Next, after obtaining the magnetoelectronic properties, the magneto-optical absorption spectra are figured out by the gradient approximation [14,68-70]. The characteristics of wave functions, and the dependence of absorption peaks on the period, field strength, modulation direction, and electric polarization direction are discussed in detail (Chapter 3). In addition to modulated magnetic fields, the effects of modulated electric fields on the electronic and optical properties are further studied (Chapter 4). Finally, chapter 5 presents the summary and future research directions. The abstracts of chapters 2-4 are as follows.

The subject of chapter 2 is "**Electronic structure of a two-dimensional graphene monolayer in a spatially modulated magnetic field: Peierls tight-binding model**". The magnetoelectronic properties of a 2D monolayer graphene are investigated by the Peierls tight-binding model. They are dominated by the period, strength, and direction of a spatially modulated magnetic field. Such a field could induce the reduction in dimensionality, change of energy dispersions, anisotropy at low energy, composite behavior

in state degeneracy, extra band-edge states, and asymmetry of energy bands. There are partial flat bands at the Fermi level and 1D parabolic bands at others, which make density of states exhibit delta-function-like structure and asymmetric prominent peaks. Energies of the extra band-edge states strongly depend on the period, while those of the original band-edge states exhibit little dependence. Both of them grow as the strength increases. The modulated and uniform magnetic fields differ from each other in energy dispersion, state degeneracy, and dimensionality. Important differences between a monolayer graphene and a 2D electron gas are also found.

The subject of chapter 3 is "**Low-frequency magneto-optical excitations in a graphene monolayer**". The low-frequency optical excitations of a monolayer graphene in a periodic magnetic field are calculated by the gradient approximation. The original and extra band-edge states make the optical absorption spectra exhibit a lot of asymmetric prominent peaks, which, respectively, lead to the principal peaks and subpeaks. The two kinds of peaks obey two different selection rules because their wave functions present different features. The intensity, frequency, and number of the absorption peaks are related to the period, strength, direction of a modulated magnetic field, and the electric polarization direction. The anisotropic absorption spectra are induced by the different modulated directions and electric polarization directions. The above mentioned results could be verified by the optical measurements.

The subject of chapter 4 is "**Electronic properties and optical absorption spectra of a graphene monolayer in the modulated electric field**". The electronic structure and optical absorption spectra of a monolayer graphene in the presence of a modulated electric field are investigated by the tight-binding model and gradient approximation. The

low-energy electronic properties and optical absorption spectra are strongly affected by the period, field strength, and modulated direction. Such a field strongly influences the energy dispersions, state degeneracy, dimensionality, band-edge states, and asymmetry of energy bands. It should be noticed that there are many extra Fermi-momentum states at $E_F = 0$. The density of states (DOS) exhibits many prominent asymmetric peaks mainly owing to the band-edge states. The finite DOS at the Fermi level means that there are free carriers, i.e., a modulated electric field could change a semiconducting graphene into a semimetallic one. The dependence of the energies related to the band-edge states on the period and field strength is investigated in detail. The optical absorption spectra display rich peaks and they vanish at $\omega = 0$. Such absorption peaks could not be ascribed to an obvious selection rule. In addition, the high-frequency energy bands are hardly affected by the modulated electric potential, and neither are the DOS and optical absorption spectra. It is worth noting that the electronic properties and optical absorption spectra could show anisotropic features in the different modulated directions. The predicted results could be verified by the experimental measurements.

References

[1] P. R. Wallace, Phys. Rev. **71**, 622 (1947).

[2] F. L. Shyu, and M. F. Lin, J. Phys. Soc. Jpn. **69**, 607 (2000).

[3] E. J. Duplock, M. Scheffler, P. J. D. Lindan, Phys. Rev. Lett. **92**, 225502 (2004).

[4] F. Ortmann, W. G. Schmidt, F. Bechstedt, Phys. Rev. Lett. **95**, 186101 (2005).

[5] J. M. D. Coey, M. Venkatesan, C. B. Fitzgerald, A. P. Douvalis, and I. S. Sanders, Nature **420**, 156 (2002).

[6] A. Hashimoto, K. Suenaga, A. Gloter, K. Urita, S. Iijima, Nature **430**, 870 (2004).

[7] E. T. Jesen, R. E. Palmer, W. Allison, and J. F. Annett, Phys. Rev. Lett. **66**, 492 (1991).

[8] H. Kempa, P. Esquinazi, and Y. Kopelevich, Phys. Rev. B **65**, 241101 (2002).

[9] Y. Zhang, J. P. Small, M. E. S. Amori, and P. Kim, Phys. Rev. Lett. **94**, 176803 (2005).

[10] K. S. Novoselov, A. K. Geim, S. V. Morozov, D. Jiang, Y. Zhang, S. V. Dubonos, I. V. Grigorieva, A. A. Firsov, Science **306**, 666 (2004).

[11] K. S. Novoselov, A. K. Geim, S. V. Morozov, D. Jiang, M. I. Katsnelson, I. V. Grigorieva, S. V. Dubonos, and A. A. Firsov, Nature **438**, 197 (2005).

[12] C. Berger, Z. M. Song, T. B. Li, X. B. Li, A. Y. Ogbazghi, R. Feng, Z. T. Dai, A. N. Marchenkov, E. H. Conrad, P. N. First, and W. A. de Heer, J. Phys. Chem. B **108**, 19912 (2004).

[13] C. Berger, Z. Song, X. Li, X. Wu, N. Brown, C. Naud, D. Mayou, T. Li, J. Hass, A. N. Marchenkov, E. H. Conrad, P. N. First, and W. A. de Heer, Science **312**, 1191 (2006).

[14] C. P. Chang, C. L. Lu, F. L. Shyu, R. B. Chen, Y. K. Fang and M. F. Lin, Carbon **42**, 2975 (2004).

[15] S. Latil and L. Henrard, Phys. Rev. Lett. **97**, 036803 (2006).

[16] Y. Zheng and T. Ando, Phys. Rev. B **65**, 245420 (2002).

[17] E. McCann, Phys. Rev. B **74**, 161403 (2006).

[18] C. L. Lu, C. P. Chang, Y. C. Huang, J. M. Lu, C. C. Hwang, and M. F. Lin, Journal of Physics: Condensed Matter **18**, 5849 (2006).

[19] F. Guinea, A. H. C. Neto, and N. M. R. Peres, Phys. Rev. B **73**, 245426 (2006).

[20] E. McCann, K. Kechedzhi, V. I. Falko, H. Suzuura, T. Ando, and B. L. Altshuler, Phys. Rev. Lett. **97**, 146805 (2006).

[21] B. Partoens and F. M. Peeters, Phys. Rev. B **74**, 075404 (2006).

[22] M. Koshino and T. Ando, Phys. Rev. B **76**, 085425 (2007)

[23] C. L. Lu, C. P. Chang, J. H. Ho, C. C. Tsai, and M. F. Lin, Physica E **32**, 585 (2006).

[24] J. H. Ho, Y. H. Lai, S. J. Tsai, J. S. Hwang, C. P. Chang, and M. F. Lin, J. Phys. Soc. Jpn. **75**, 114703 (2006).

[25] E. McCann and V. I. Fal'ko, Phys. Rev. Lett. **96**, 086805 (2006).

[26] J. M. Pereira, F. M. Peeters, and P. Vasilopoulos, Phys. Rev. B **76**, 115419 (2007).

[27] N. Nemec and G. Cuniberti, Phys. Rev. B **75**, 201404 (2007).

[28] J. H. Ho, Y. H. Lai, Y. H. Chiu, and M. F. Lin, Nanotechnology **19**, 035712 (2008).

[29] Y. H. Chiu, Y. H. Lai, J. H. Ho, D. S. Chuu, and M. F. Lin, Phys. Rev. B **77**, 045407 (2008).

[30] E. V. Castro, K. S. Novoselov, S. V. Morozov, N. M. R. Peres, J. M. B. Lopes dos Santos, J. Nilsson, F. Guinea, A. K. Geim, and A. H. Castro Neto, Phys. Rev. Lett. **99**, 216802 (2007).

[31] Y. H. Lai, J. H. Ho, C. P. Chang, and M. F. Lin, Phys. Rev. B **77**, 085426 (2008).

[32] F. L. Shyu and M. F. Lin, J. Phys. Soc. Jpn. **69**, 607 (2000).

[33] J. H. Ho, C. P. Chang and M. F. Lin, Phys. Lett. A **352**, 446 (2006).

[34] J. H. Ho, C. L. Lu, C. C. Hwang, C. P. Chang and M. F. Lin, Phys. Rev. B **74**, 085406 (2006).

[35] X. F. Wang and T. Chakraborty, Phys. Rev. B **75**, 041404 (2007).

[36] A. H. Castro Neto and F. Guinea, Phys. Rev. B **75**, 045404 (2007).

[37] Y. Zhang, Y. W. Tan, H. L. Stormer, and P. Kim, Nature **438**, 201 (2005).

[38] K. S. Novoselov, Z. Jiang, Y. Zhang, S. V. Morozov, H. L. Stormer, U. Zeitler, J. C. Maan, G. S. Boebinger, P. Kim, and A. K. Geim, Science **315**, 1379 (2007).

[39] K. S. Novoselov, E. McCann, S. V. Morozov, V. I. Fal'ko, M. I. Katsnelson, U. Zeitler, D. Jiang, F. Schedin, and A. K. Geim, Nat. Phys. **2**, 177 (2006).

[40] V. P. Gusynin and S. G. Sharapov, Phys. Rev. B **73**, 245411 (2006).

[41] V. P. Gusynin, V. A. Miransky, S. G. Sharapov, and I. A. Shovkovy, Phys. Rev. B **74**, 195429 (2006).

[42] M. Koshino and T. Ando, Phys. Rev. B 73, 245403 (2006).

[43] J. Nilsson, A. H. Castro Neto, F. Guinea, and N. M. R. Peres, Phys. Rev. Lett. **97**, 266801 (2006).

[44] N. M. R. Peres, F. Guinea, and A. H. Castro Neto, Phys. Rev. B **73**, 125411 (2006).

[45] M. L. Sadowski, G. Martinex, and M. Potemski, C. Berger, and W. A. de Heer, Phys. Rev. Lett. **97**, 266405 (2006).

[46] D. S. L. Abergel and Vladimir I. Fal'ko, Phys. Rev. B **75**, 155430 (2007).

[47] R. S. Deacon, K.-C. Chuang, R. J. Nicholas, K. S. Novoselov, and A. K. Geim, Phys. Rev. B **76**, 081406 (2007).

[48] D. S. L. Abergel, A. Russell, and Vladimir I. Fal'ko, Appl. Phys. Lett. **91**, 063125 (2007).

[49] C. L. Lu, C. P. Chang, Y. C. Huang, R. B. Chen, and M. F. Lin, Phys. Rev. B **73**, 144427 (2006).

[50] C. L. Lu, H. L. Lin, C. C. Hwang, J. Wang, C. P. Chang, and M. F. Lin, Appl. Phys. Lett. **89**, 221910 (2006).

[51] Z. Jiang, E. A. Henriksen, L. C. Tung, Y.-J. Wang, M. E. Schwartz, M. Y. Han, P. Kim, and H. L. Stormer, Phys. Rev. Lett. **98**, 197403 (2007).

[52] S. Y. Zhou, G.-H. Gweon, J. Graf, A. V. Fedorov, C. D. Spataru, R. D. Diehl, Y. Kopelevich, D.-H. Lee, Steven G. Louie, and A. Lanzara, Nature. Physics **2**, 595 (2006).

[53] J. W. McClure, Phys. Rev. **104**, 666 (1956).

[54] F. D. Haldane, Phys. Rev. Lett. **61**, 2015 (1988).

[55] S. P. Beaumont and M. G. Blamire, Phys. Rev. Lett. **74**, 3009 (1995).

[56] P. D. Ye, D. Weiss, R. R. Gerhardts, M. Seeger, K. von Klitzing, K. Eberl and H. Nickel, Phys. Rev. Lett. **74**, 3013 (1995).

[57] Mayumi Kato, Akira Endo, Makoto Sakairi, Shingo Katsumoto and Yasuhiro Iye, Journal of the physical society of Japan **68**, 1492 (1999).

[58] S. Cina, D. M. Whittaker, D. D. Arnone, T. Burke, H. P. Hughes, M. Leadbeater, M. Pepper and D. A. Ritchie, Phys. Rev. Lett. **83**, 4425 (1999).

[59] P. Vasilopoulos and F. M. Peeters, Superlattices and Microstructures **7**, 393 (1990).

[60] F. M. Peeters and P. Vasilopoulos, Phys. Rev. B **47**, 1466 (1993).

[61] I. S. Ibrahim and F. Peeters, Phys. Rev. B **52**, 17321 (1995).

[62] Andrey Krakovsky, Phys. Rev. B **53**, 8469 (1996).

[63] A. Y. Rom, Phys. Rev. B **55**, 11025 (1997).

[64] J. M. Luttinger, Phys. Rev. **84**, 814 (1951).

[65] S. M. Stewart and C. Zhang, Semicond. Sci. Technol. **10**, 1541 (1995).

[66] S. M. Stewart and C. Zhang, Phys. Rev. B **52**, R17036 (1995).

[67] S. M. Stewart and C. Zhang, Condens. Matter **8**, 6019 (1996).

[68] M. F. Lin and Kenneth W.-K. Shung, Phys. Rev. B **50**, 17744 (1994).

[69] Y. C. Huang, M. F. Lin, and C. P. Chang, J. App. Phy. **103**, 073709 (2008).

[70] J. Blinowski, N. H. Hau, C. Rigaux, J. P. Vieren, R. L. Toullee, G. Furdin, A. Herold, and J. Melin, J. Phys. (Paris) **41**, 47 (1980).

Chapter 2

Electronic structure of a two-dimensional graphene monolayer in a spatially modulated magnetic field: Peierls tight-binding model

2.1 Introduction

Condensed-matter systems, such as diamond, layered graphenes, carbon nanotubes, carbon tori, C_{60}-related fullerenes, and carbon onions, are purely made up of carbon atoms. Such systems have very special symmetric configurations, and their dimensionalities vary from 3D to 0D. They could exhibit rich electronic properties, e.g., a wide-gap diamond, a semimetallic bulk graphite, a zero-gap monolayer graphene, a metallic armchair carbon nanotube, and a small-gap nonarmchair carbon nanotube. Recently, few-layer graphenes with 2D hexagonal symmetry and nanoscaled thickness could be produced by controlling film thickness with single-atom accuracy [1]. A lot of researches have been strongly motivated, such as growth [2], phonon [3], band structure [4-7], electronic excitations [8-11], optical spectra [12,13], and transport properties [14-20]. These experimental [14-18] and theoretical [19,20] studies show that they display the novel quantum Hall effect.

A 2D monolayer graphene owns linear bands intersecting at the Fermi level $E_F = 0$. Energy bands are isotropic at low energy ($\lesssim$0.5 eV) [21], and so are the low-frequency physical properties (e.g., Coulomb excitations) [8,10]. They produce a vanishing density of states at $E_F = 0$, which makes a monolayer graphene an exotic zero-gap semiconductor. The two important characteristics, isotropy and semiconductor, originate from the hexagonal symmetric configuration. Electronic properties are completely changed by applying

a uniform perpendicular magnetic field. Most of energy bands become the dispersionless Landau levels. The effective-mass model predicts that energies of the low Landau levels are proportional to the square root of field strength and quantum number [22]. These theoretical predictions have been verified by experimental measurements on transport properties [16] and optical spectra [12]. An inhomogeneous magnetic field might also strongly affect the essential physical properties. Haldane first investigated whether a 2D graphene could exhibit the special magnetoconductance in the presence of a vanishing net magnetic field [23]. In this work, we mainly focus on the effects of a periodic magnetic field on electronic properties.

There are numerous experimental [24-27] and theoretical [28-36] researches for a 2D electron gas (2DEG) under a spatially modulated magnetic field. These works primarily analyze the transport properties [24-26,28,29], energy bands [30-32], electronic excitations [33-36], and optical spectra [27]. The transport measurements [24,25] manifest the oscillatory magnetoresistance. Energy bands of a 2DEG have parabolic energy dispersions. A periodic magnetic field leads to the drastic changes in electronic properties, e.g., the changes in state degeneracy, band-edge states, and curvatures.

The Peierls tight-binding model is used to calculate the electronic structure of a 2D graphene in a spatially modulated magnetic field. The Hamiltonian is a huge Hermitian matrix for a large modulation period ($\gtrsim$1000 Å). The numerical techniques are developed to attain a band-like Hamiltonian matrix. The dependence of electronic properties on the direction, period, and strength of the modulated magnetic field would be investigated in detail, e.g., energy dispersions, state degeneracy, band-edge states, symmetry of energy bands, and density of states. A comparison with those of a uniform magnetic field is made.

The important differences between a monolayer graphene and a 2DEG are also discussed.

This paper is organized as follows. The band-like Hamiltonian matrix in a periodic magnetic field is derived in Sec. II. The main characteristics of the π-electronic structures are discussed in Sec. III. Finally, Sec. IV contains concluding remarks.

2.2 Peierls Hamiltonian band matrix

The tight-binding model with nearest-neighbor interactions is used to calculate the π-electronic structure of $2p_z$ orbitals. In the honeycomb structure of a 2D single-layer graphene in the absence of an external field, there are two kinds of carbon atoms, a and b, in a primitive unit cell. The wave function consisting of the two linear tight-binding functions from periodic $2p_z$ orbitals is expressed as $|\Psi_{\mathbf{k}}\rangle = C_{a\mathbf{k}}|a_{\mathbf{k}}\rangle + C_{b\mathbf{k}}|b_{\mathbf{k}}\rangle$, where $|a_{\mathbf{k}}\rangle = \sum_i e^{i\mathbf{k}\cdot\mathbf{R}_i}|a_{i\mathbf{k}}\rangle$ and $|b_{\mathbf{k}}\rangle = \sum_j e^{i\mathbf{k}\cdot\mathbf{R}_j}|b_{j\mathbf{k}}\rangle$. The Hamiltonian built from $|a_{\mathbf{k}}\rangle$ and $|b_{\mathbf{k}}\rangle$ is a 2×2 Hermitian matrix . The site energies are vanishing ($\langle a_{i\mathbf{k}}|H_0|a_{i\mathbf{k}}\rangle = \langle b_{i\mathbf{k}}|H_0|b_{i\mathbf{k}}\rangle = 0$), and the nearest-neighbor hopping integral is given by

$$\langle b_{j\mathbf{k}}|H_0|a_{i\mathbf{k}}\rangle = \gamma_0 \exp[\, i\mathbf{k}\cdot(\mathbf{R}_i - \mathbf{R}_j)\,], \tag{2.1}$$

where γ_0(=2.56 eV) [21] is the atom-atom interaction between two neighboring atoms at $\mathbf{R}_i$ and $\mathbf{R}_j$.

A monolayer graphene is assumed to exist in a spatially modulated magnetic field $\mathbf{B} = B\sin(Kx)\hat{z}$ along the armchair direction (the x-axis in Fig. 2.1(a)), and the periodic length is $l_B = 2\pi/K = 3b'R_B$, where parameter R_B is useful in describing the dimensionality of the Hamiltonian matrix. The magnetic flux, product of the field strength and the hexagonal area in the unit of flux quantum ($\Phi_0 = hc/e = 4.1356\times 10^{-15}\,[T/m^2]$), is $\Phi = (3\sqrt{3}Bb'^2/2)/\Phi_0$. b'=1.42 Å is the C-C bond length. The modulated magnetic field that

leads to the Peierls phase is characterized by the vector potential $\mathbf{A} = -[B\cos(Kx)]/K\hat{y}$. The nearest-neighbor hopping integral becomes

$$\langle b_{j\mathbf{k}}|H_{\mathbf{B}}|a_{i\mathbf{k}}\rangle = \gamma_0 \exp\{i[\,\mathbf{k}\cdot(\mathbf{R}_i - \mathbf{R}_j) + \frac{2\pi}{\Phi_0}\int_{\mathbf{R}_i}^{\mathbf{R}_j}\mathbf{A}\cdot d\mathbf{r}\,]\}. \tag{2.2}$$

For three nearest-neighbor atoms, their hopping integrals are, respectively, $t_{1\mathbf{k}}(n) = \gamma_0 \exp[\,(ik_x b'/2 + ik_y\sqrt{3}b'/2) + G_n\,]$, $t_{2\mathbf{k}}(n) = \gamma_0 \exp[\,(ik_x b'/2 - ik_y\sqrt{3}b'/2) - G_n\,]$, and $t_{3\mathbf{k}}(n) = \gamma_0 \exp(-ik_x b'\,)$, where $G_n = -i[6(R_B)^2\Phi/\pi]\cos[\pi(n-5/6)/R_B]\sin(\pi/6R_B)\,]$. The modulation period causes the periodic boundary conditions along the x-axis so that the corresponding Peierls phase is periodic in a period $2R_B$. An enlarged rectangular unit cell includes $4R_B$ carbon atoms. The wave function and the Hamiltonian matrix element are, respectively, given by

$$|\Psi_{\mathbf{k}}\rangle = \sum_{n=1}^{2R_B} C^n_{a\mathbf{k}}|a_{n\mathbf{k}}\rangle + C^n_{b\mathbf{k}}|b_{n\mathbf{k}}\rangle; \tag{2.3a}$$

$$\langle b_{m\mathbf{k}}|H_{\mathbf{B}}|a_{n\mathbf{k}}\rangle = [t_{1\mathbf{k}}(n) + t_{2\mathbf{k}}(n)]\delta_{m,n} + t_{3\mathbf{k}}(n)\delta_{m,n-1}. \tag{2.3b}$$

$C^n_{a\mathbf{k}} = C^{n+2R_B}_{a\mathbf{k}}$ and $C^n_{b\mathbf{k}} = C^{n+2R_B}_{b\mathbf{k}}$ are derived because of the periodical boundary condition. To solve the complicated calculations of the huge Hamiltonian matrix, the base functions are chosen as the following sequence $\{|a_{1\mathbf{k}}\rangle,\ |b_{2R_B\mathbf{k}}\rangle,\ |b_{1\mathbf{k}}\rangle,\ |a_{2R_B\mathbf{k}}\rangle,\ |a_{2\mathbf{k}}\rangle,\ |b_{2R_B-1\mathbf{k}}\rangle,\ |b_{2\mathbf{k}}\rangle,\ |a_{2R_B-1\mathbf{k}}\rangle,\ \ldots\ |a_{R_B-1\mathbf{k}}\rangle,\ |b_{R_B+2\mathbf{k}}\rangle,\ |b_{R_B-1\mathbf{k}}\rangle,\ |a_{R_B+2\mathbf{k}}\rangle,\ |a_{R_B\mathbf{k}}\rangle,\ |b_{R_B+1\mathbf{k}}\rangle,\ |b_{R_B\mathbf{k}}\rangle;\ |a_{R_B+1\mathbf{k}}\rangle\}$.

The Hamiltonian matrix could be expressed as a $4R_B \times 4R_B$ band-like Hermitian matrix

$$\begin{pmatrix} 0 & q^* & p_1^* & 0 & \dots & \dots & 0 & 0 \\ q & 0 & 0 & p_{2R_B} & 0 & \dots & \dots & 0 \\ p_1 & 0 & 0 & 0 & q & 0 & \dots & 0 \\ 0 & p_{2R_B}^* & 0 & 0 & 0 & q^* & 0 & 0 \\ \vdots & \ddots & q^* & 0 & 0 & \ddots & \ddots & 0 \\ \vdots & \dots & \ddots & q & \ddots & \ddots & 0 & p_{R_B+1} \\ 0 & \vdots & \vdots & \ddots & \ddots & 0 & \ddots & q \\ 0 & 0 & 0 & 0 & 0 & p_{R_B+1}^* & q^* & 0 \end{pmatrix}, \tag{2.4}$$

where $p_n \equiv t_{1\mathbf{k}}(n) + t_{2\mathbf{k}}(n)$ and $q \equiv t_{3\mathbf{k}}$. Because the range of k_x is much smaller than that of k_y for a large R_B, it is sufficient just to consider 1D energy dispersions along k_y. That is to say, a modulated magnetic field could effectively reduce the dimensionality by one.

The π-electronic structure strongly depends on the direction of the modulated magnetic field, mainly owing to the anisotropic structure of a 2D monolayer graphene. For the zigzag direction (Fig. 2.1(b)), the similar calculations could also be done. By the detailed derivations, the three hopping integrals are $t'_{1\mathbf{k}}(n) = \gamma_0 \exp[\,(ik_x\sqrt{3}b'/2 + ik_y b'/2) + G'_n]$, $t'_{2\mathbf{k}}(n) = \gamma_0 \exp[\,(-ik_x\sqrt{3}b'/2 + ik_y b'/2) - G'_{n-1}]$, and $t'_{3\mathbf{k}}(n) = \gamma_0 \exp[\,(-ik_y b') + G''_n\,]$, where $G'_n = -i[2(R_B)^2\Phi/3\pi]\cos[\pi(n-1/2)/R_B]\sin(\pi/2R_B)$ and $G''_n = -i[(2R_B\Phi/3)\cos[(n-1)\pi/R_B]\,]$. The Hamiltonian matrix element is further given by

$$\langle b_{m\mathbf{k}}|H_{\mathbf{B}}|a_{n\mathbf{k}}\rangle = t'_{1\mathbf{k}}(n)\delta_{m,n+1} + t'_{2\mathbf{k}}(n)\delta_{m,n-1} + t'_{3\mathbf{k}}(n)\delta_{m,n}. \tag{2.5}$$

With the base functions $\{|a_{1\mathbf{k}}\rangle, |b_{2R_B\mathbf{k}}\rangle, |b_{1\mathbf{k}}\rangle, |a_{2R_B\mathbf{k}}\rangle, |b_{2\mathbf{k}}\rangle, |a_{2R_B-1\mathbf{k}}\rangle, |a_{2\mathbf{k}}\rangle, |b_{2R_B-1\mathbf{k}}\rangle, \dots$ $|b_{R_B-1\mathbf{k}}\rangle, |a_{R_B+2\mathbf{k}}\rangle, |a_{R_B-1\mathbf{k}}\rangle, |b_{R_B+2\mathbf{k}}\rangle, |a_{R_B\mathbf{k}}\rangle, |b_{R_B+1\mathbf{k}}\rangle, |b_{R_B\mathbf{k}}\rangle; |a_{R_B+1\mathbf{k}}\rangle\}$, the $4R_B \times 4R_B$

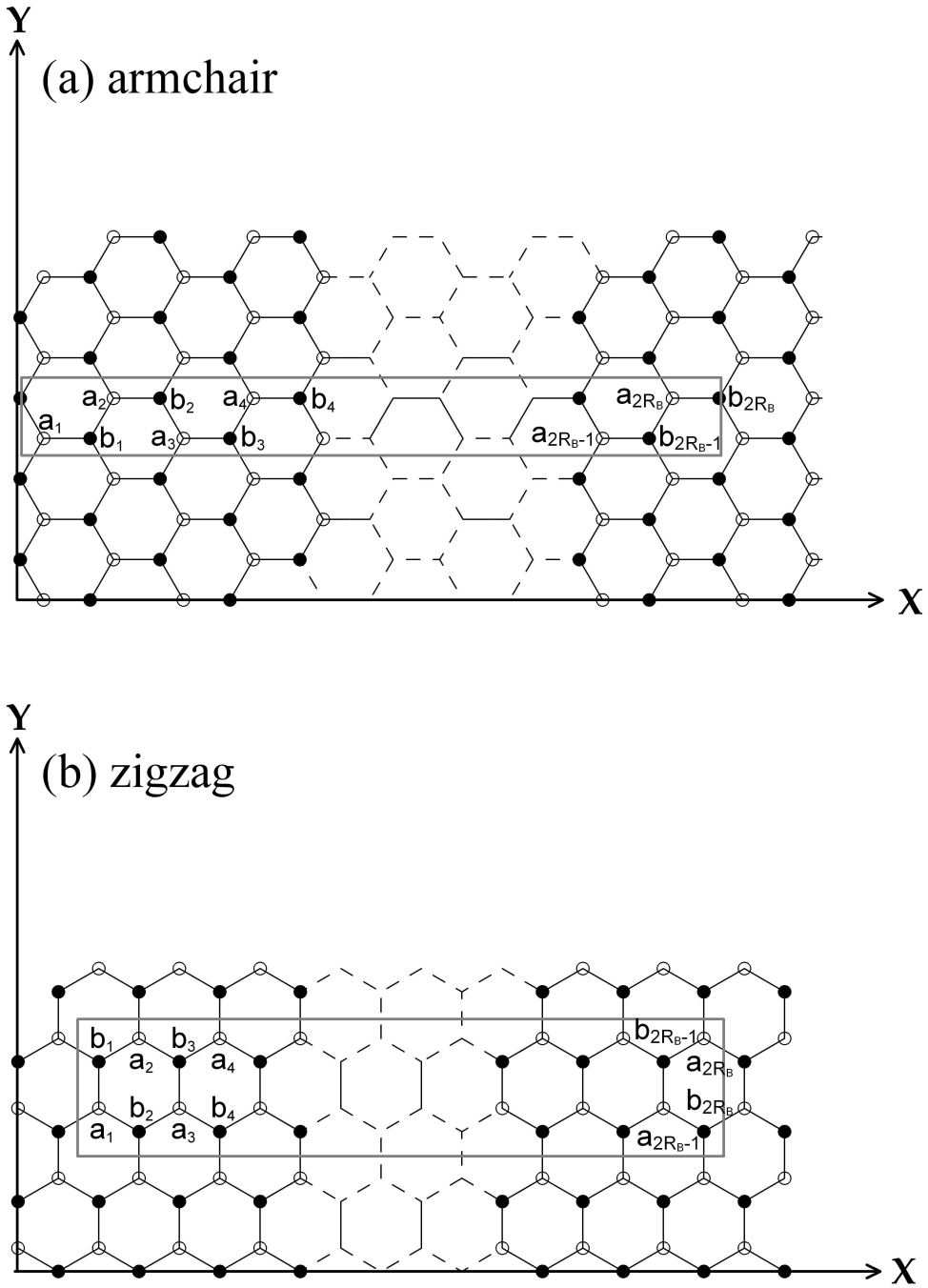

Figure 2.1. The primitive unit cell of a monolayer graphene in the spatially modulated magnetic field with period R_B along (a) the armchair direction and (b) zigzag direction.

band-like Hamiltonian matrix for the zigzag direction is

$$\begin{pmatrix}
0 & u^*_{2R_B} & v^*_1 & 0 & s^*_1 & 0 & \dots & 0 & 0 & 0 \\
u_{2R_B} & 0 & 0 & v_{2R_B} & 0 & s_{2R_B-1} & 0 & 0 & 0 & 0 \\
v_1 & 0 & 0 & s_{2R_B} & \ddots & \ddots & \ddots & \ddots & 0 & 0 \\
0 & v^*_{2R_B} & s^*_{2R_B} & 0 & \ddots & & & \ddots & 0 & \vdots \\
s_1 & 0 & \ddots & \ddots & \ddots & & & \ddots & s^*_{R_B-1} & 0 \\
0 & s^*_{2R_B-1} & \ddots & & & \ddots & \ddots & \ddots & 0 & s_{R_B+1} \\
\vdots & 0 & \ddots & & & \ddots & 0 & s^*_{R_B} & v^*_{R_B} & 0 \\
0 & 0 & \ddots & \ddots & \ddots & \ddots & s_{R_B} & 0 & 0 & v_{R_B+1} \\
0 & 0 & 0 & 0 & s_{R_B-1} & 0 & v_{R_B} & 0 & 0 & u_{R_B} \\
0 & 0 & 0 & \dots & 0 & s^*_{R_B+1} & 0 & v^*_{R_B+1} & u^*_{R_B} & 0
\end{pmatrix}, \tag{2.6}$$

where $s_n \equiv t'_{1\mathbf{k}}(n)$, $u_n \equiv t'_{2\mathbf{k}}(n)$ and $v_n \equiv t'_{3\mathbf{k}}(n)$. The Hamiltonian matrices in Eqs. (2.4) and (2.6), respectively, have two and three independent matrix elements.

2.3 Magnetoelectronic properties

The unoccupied conduction bands (E^c's) are symmetric to the occupied valence bands (E^ν's) about the Fermi level $E_F = 0$. Only the former are discussed in this work. We first look at the low energy bands resulting from the modulated magnetic field with period $R_B = 1000$ along the armchair direction. At $B = 0$, most of energy bands are parabolic dispersions with the double degeneracy except two nondegenerate linear bands intersecting at $E_F = 0$ (the solid circles in Fig. 2.2(a)). There is only one band-edge state in each energy band; furthermore, all the band-edge states are located at $k_y^{pp} = 2\pi/3\sqrt{3}b'$ (the original band-edge states). The modulated magnetic field leads to drastic changes in band-

edge states and energy dispersions, as shown in Fig. 2.2(a) by the open circles at $B = 20$ T. The range of k_y, where electronic states could exist, becomes large. The linear bands are changed into partial flat bands at $E_F = 0$. Also noted that this result is similar to that of carbon nanotubes in magnetic fields perpendicular to the symmetry axis [37]. The doubly degenerate parabolic bands have weak energy dispersions or low curvatures at k_y^{pp}, and their number is largely reduced. Such effects suggest that a magnetic field could make electronic states flock together. The modulation effects of $\mathbf{B}$ on parabolic energy bands result in four extra band-edge states at k_y^{sp}'s, the strong energy dispersions close to k_y^{sp}'s, and the destruction of the double degeneracy. The two extra band-edge states at the left- and right-hand sites of k_y^{pp} might have different energies; that is, one side of the parabolic bands might be asymmetric to the other about the original band-edge states. Each parabolic band exhibits the composite behavior in state degeneracy, the single and double degeneracies near k_y^{sp} and k_y^{pp} respectively.

The number of subbands grows quickly as state energy E^c increases from zero. There are many middle energy bands near $E^c \simeq \gamma_0$, as shown in Fig. 2.2(b). At $B = 0$, they include complete flat bands at $E^c = \gamma_0$ and parabolic bands at the others. Both are doubly degenerate. The parabolic bands have a low curvature at $k_y^{pp} = \pi/2\sqrt{3}b'$ and the high curvature at $k_y^{sp} = 0$ (not shown). Moreover, in the small or large k_y, the modulated magnetic field could destroy double degeneracy and create extra band-edge states. It modifies the band curvatures at k_y^{pp}, and makes the complete flat bands change into the partial flat bands.

The subband number decreases gradually with the further increase of state energy. The high energy bands, as shown in Fig. 2.2(c) for $B = 0$, are parabolic dispersions with the

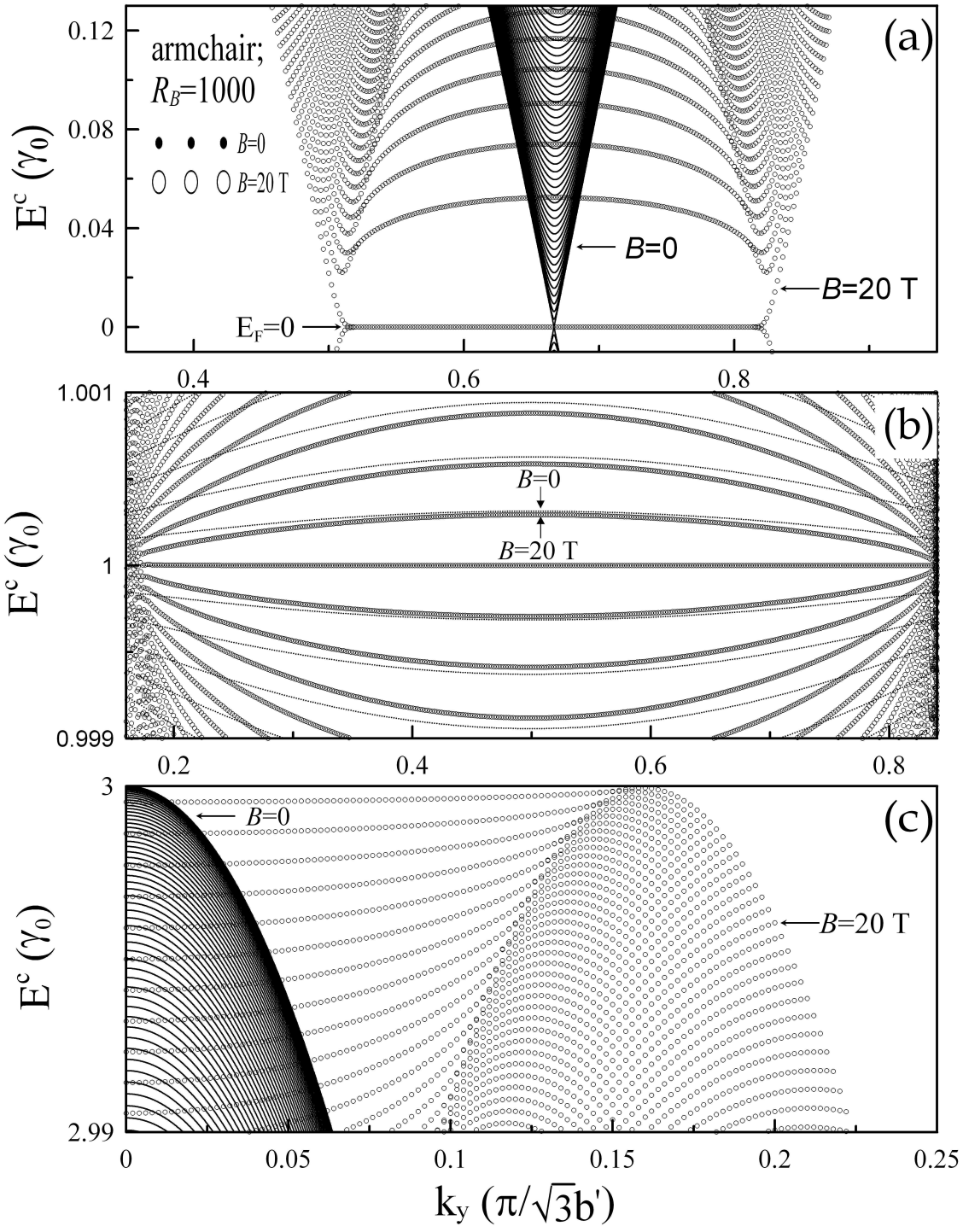

Figure 2.2. Energy bands near (a) $E^c = 0$, (b) $E^c = \gamma_0$, and (c) $E^c = 3\gamma_0$ for the armchair modulation direction at ($R_B = 1000$ and $B = 20$ T). Those without B are also shown for comparison.

double degeneracy and one band-edge state at $k_y^{pp} = 0$. All the k_y^{pp} states remain unchanged in the presence of $\mathbf{B}$, as seen in low and middle energy bands. However, the modulated magnetic field could reduce the number of subbands or widen the range of k_y, produce the extra band-edge states at $k_y^{sp} \neq 0$, and induce the composite behavior of the single and double degeneracies.

The strength, period, and direction of the modulated magnetic field strongly affect the electronic structure, as shown in Figs. 2.3(a)-2.3(b) for the low energy bands. The range of partial flat bands increases with the increasing B, while their number and curvatures exhibit the opposite behavior (Figs. 2.3(a) and 2.2(a)). These results further demonstrate that the ability to flock electronic states is enhanced by the increasing field strength. The longer the period is, the larger the effective range of k_y is (Figs. 2.3(b) and 2.2(a)). The period could alter state energies and curvatures of extra band-edge states at k_y^{sp}'s. It is also worth noting that $k_y^{pp} = 2\pi/3\sqrt{3}b'$ of the doubly degenerate parabolic bands is independent of period and strength. When the spatially modulated direction is along the zigzag structure, there are two partial flat bands at $E_F = 0$ and many parabolic bands at the others (Fig. 2.3(c)). The former are doubly degenerate; the later are fourfold degenerate near $k_y^{pp} = 0$ and doubly degenerate near k_y^{sp}. That state degeneracy, subband number, k_y's of band-edge states, and range of partial flat bands depend on the modulation direction directly reflects the anisotropic characteristic of a graphene geometry. In addition, the similar effects could also be found in moderate and high energy bands.

Density of states (DOS), which is closely related to essential features of the electronic

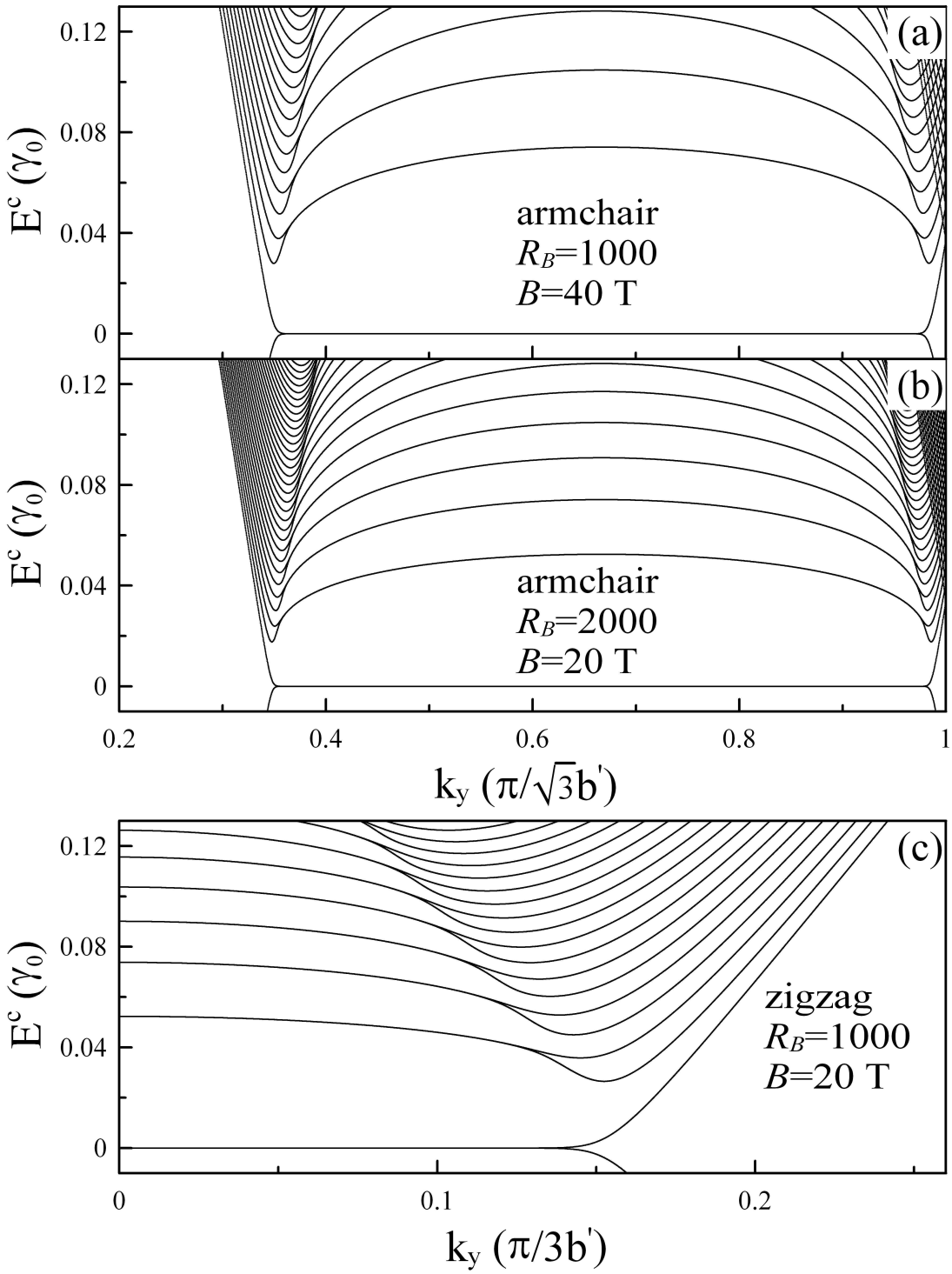

Figure 2.3. The low energy bands along the armchair direction at (a) ($R_B = 1000$, $B = 40$ T) & (b) ($R_B = 2000$, $B = 20$ T), and those along (c) the zigzag direction at ($R_B = 1000$, $B = 20$ T).

structure, is defined as

$$D(\omega) = \sum_{\sigma,h=c,\nu} \int_{1stBZ} \frac{dk_x dk_y}{(2\pi)^2} \frac{\Gamma}{\pi} \frac{1}{[E^h(k_x,k_y)-\omega]^2+\Gamma^2}. \tag{2.7}$$

$\Gamma(=10^{-4}\ \gamma_0)$ is a phenomenological broadening parameter. The integration on k_x could be roughly neglected because of the very small range of k_x. The low-frequency DOS at $B = 0$ is proportional to ω, as shown in Fig. 2.4(a). It vanishes at $\omega = 0$ and has no special structures. However, the modulated magnetic field leads to a symmetric delta-function-like peak at $\omega = 0$ (inset in Fig. 2.4(a)) and considerable asymmetric square-root divergent peaks. The former comes from the two partial flat bands at $E_F = 0$, and its height grows with the increasing field strength. The latter are dominated by the band-edge states of the 1D parabolic dispersions along $\widehat{k}_y$ (Fig. 2.2(a)). The asymmetric pronounced peaks could be further divided into weak subpeaks and strong principal peaks. They are, respectively, due to the band-edge states at k_y^{sp}'s and k_y^{pp}. There are many pairs of subpeaks, and each pair of subpeaks is associated with the asymmetry of the 1D parabolic bands about the k_y^{pp} states (discussed earlier in Fig. 2.2(a)). The number, frequencies, and heights of the asymmetric prominent peaks are sensitive to the changes in the strength, period, and modulation direction. The peak number decreases with the increase of the strength, while the peak frequencies exhibit a different behavior (Fig. 2.4(a)). The number of subpeaks increases as the period grows (Fig. 2.4(b)), while it is the other way around as the frequencies of subpeaks increase. The main features of principal peaks have the weak dependence on the period. When the modulation direction is orientated relatively close to the zigzag structure, more principal peaks with lower frequencies are observed (comparison between the heavy and light solid curves in Fig. 2.4(b)). Density of states could display the high anisotropy even at very low frequency ($\omega \to 0$ in the inset of Fig.

2.4(b)). However, the low-frequency physical properties without $\mathbf{B}$ are anisotropic only for $\omega \gtrsim 0.25\ \gamma_0$, e.g., electronic excitations and absorption spectra [9]. This result indicates that the anisotropy of the low-frequency electronic properties could be induced by means of a spatially modulated magnetic field.

The frequencies of prominent peaks in DOS deserve a closer investigation. Fig. 2.5(a) shows the relation between the frequencies (ω_{sp}'s) of the first six subpeaks and the period at $B = 20$ T. These peaks correspond to the extra band-edge states at the left-hand neighborhood of k_y^{pp} (Fig. 2.2(a)). ω_{sp}'s decline quickly as R_B increases. As to the frequencies of principal peaks (ω_{pp}'s), their dependence on the period is minor for a sufficient large R_B ($\gtrsim 1000$), as shown in Fig. 2.5(b). Both ω_{sp}'s and ω_{pp}'s are largely enhanced by the increasing field strength (Figs. 2.5(c) and 2.5(d)). There exists a special square-root relation between ω_{pp} and B, i.e., $\omega_{pp} \propto \sqrt{B}$. In addition, the low-energy flat Landau levels due to a uniform magnetic field ($\mathbf{B}_0$) also exhibit the square-root dependence on the field strength [22]. The band-edge state energies are closely related to the magneto-optical absorption frequencies. The predicted results could be verified by the optical spectroscopy.

A uniform magnetic field differs from a spatially modulated magnetic field in the low-energy magnetoelectronic structures. In terms of the ability in flocking electronic states, the former is much stronger than the latter. A uniform magnetic field could make linear or parabolic bands convert into the dispersionless Landau levels. Such levels are fourfold degenerate for each k_y state. All the Landau states could be regarded as the band-edge states. They would exhibit zero-dimensional features, but not one-dimensional features. For example, the magneto-optical absorption spectra display the symmetric and asymmetric prominent peaks in cases $\mathbf{B}_0$ and $\mathbf{B}$, respectively.

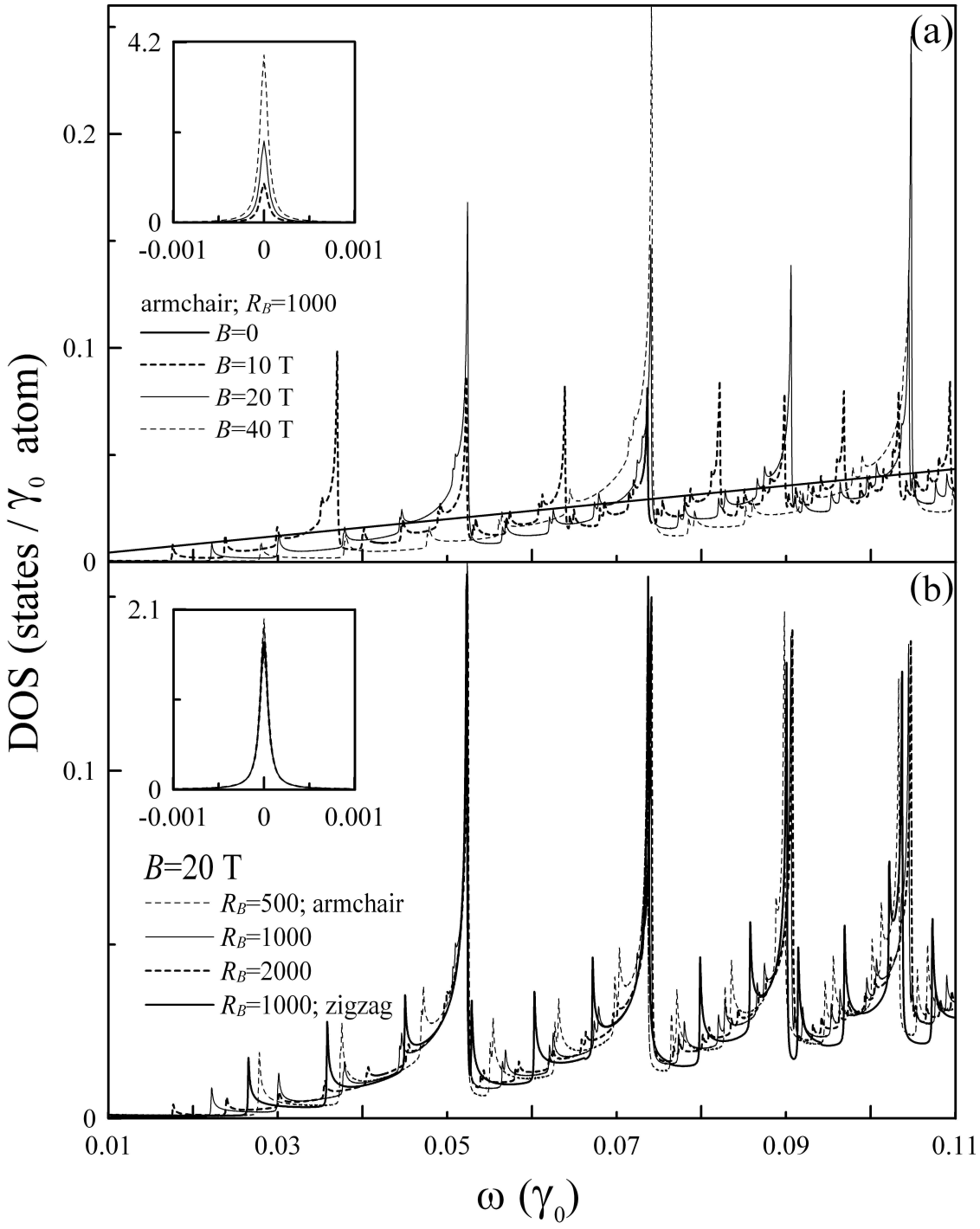

Figure 2.4. The low-frequency density of states (a) along the armchair direction at $R_B = 1000$ and different B's; (b) at $B = 20$ T and different R_B's or directions. The insets show those near $E_F = 0$.

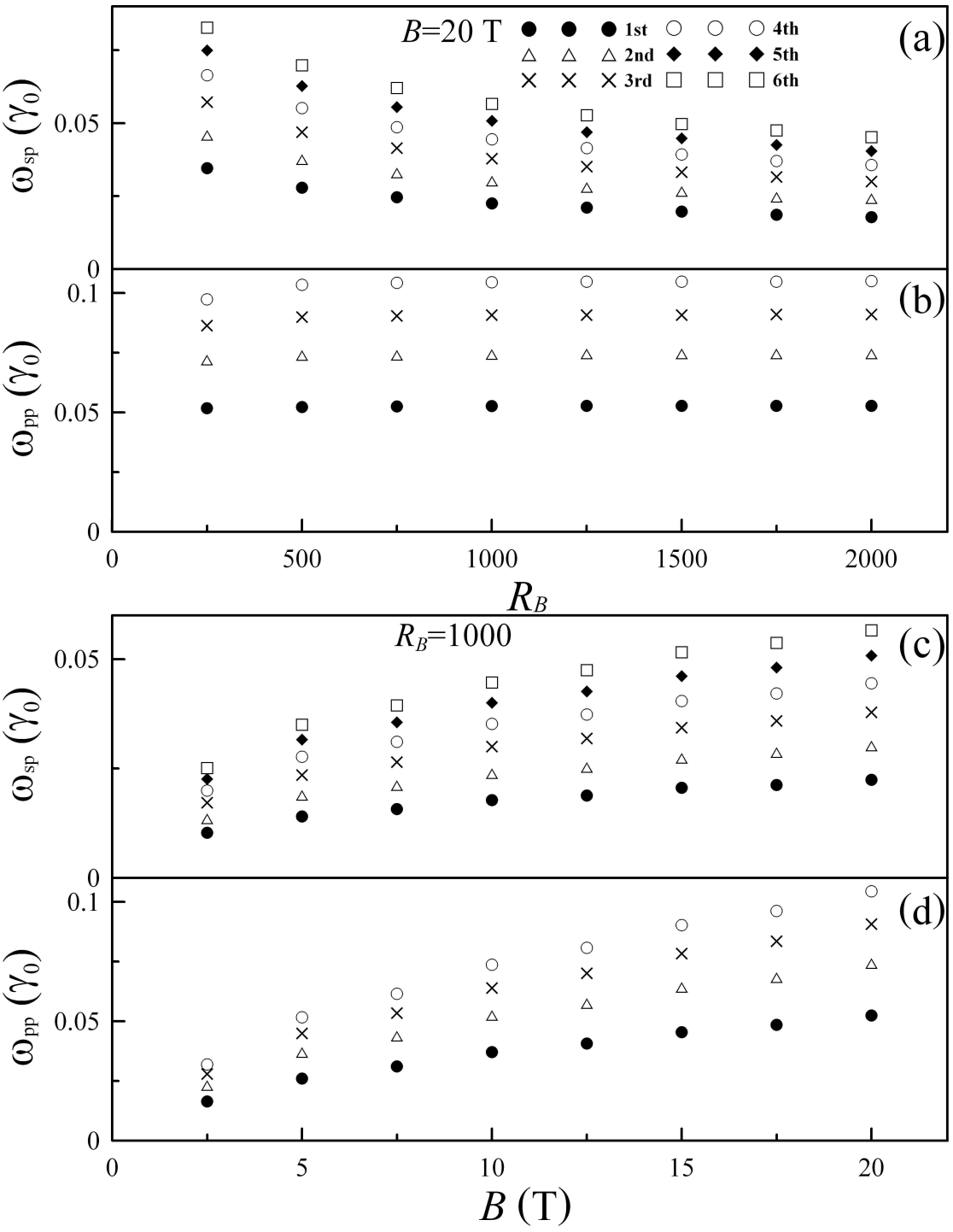

Figure 2.5. Energies (ω_{sp}'s) of extra band-edge states at the left-hand neighborhood of k_y^{pp} and those (ω_{pp}'s) of the original band-edge states. (a) and (b) are their dependence on the period; (c) and (d) correspond to the dependence on the strength.

The electronic structure of a 2DEG could be strongly affected by a spatially modulated magnetic field [20-32]. It also displays the similar behaviors to a monolayer graphene, such as the composite behavior in state degeneracy, creation of extra band-edge states, and change of curvatures. However, there are three significant differences between a 2DEG and a monolayer graphene. A 2DEG does not exhibit partial flat bands at zero energy. Its magnetoelectronic structure is independent of the modulation direction. Moreover, the wave vectors of extra band-edge states are approximately close to $k_y = 0$ and hardly depend on the state energy. The above-mentioned differences mainly come from the hexagonal structure of a monolayer graphene.

2.4 Concluding remarks

In summary, the magnetoelectronic structure of a 2D monolayer graphene is studied by the Peierls tight-binding model. The specific base functions are chosen to solve a huge Hamiltonian matrix. The strength, period, and direction of a spatially modulated magnetic field dominate the main features of electronic properties. Such a field could reduce dimensionality by one, alter energy dispersions, cause anisotropy at low energy, induce composite behavior in state degeneracy (the composite behavior of single and double degeneracies for the armchair direction), produce extra band-edge states, and destroy the symmetry of energy bands about the original band-edge states. Energies of the extra band-edge states strongly rely on the period, while the opposite is true for those of the original band-edge states. Both of them grow with the increase of the strength. Density of states owns many asymmetric prominent peaks, mainly owing to the band-edge states in 1D parabolic bands. The partial flat bands also make DOS display delta-function-like structures at the Fermi

level. A spatially modulated magnetic field contrasts sharply with a uniform magnetic field in energy dispersion, state degeneracy, and dimensionality. The important differences between a monolayer graphene and a 2DEG arise from the hexagonal symmetry. They are the existence of the partial flat bands at zero energy, dependence on the modulation direction, and wave vectors of the band-edge states. The experimental measurements on the magneto-optical absorption spectra could be utilized to examine the predicted electronic properties.

References

[1] K. S. Novoselov, A. K. Geim, S. V. Morozov, D. Jiang, Y. Zhang, S. V. Dubonos, I. V. Grigorieva and A. A. Firsov, Science **306**, 666 (2004).

[2] C. Berger, Z. Song, T. Li, X. Li, A. Y. Ogbazghi, R. Feng, Z. Dai, A. N. Marchenkov, E. H. Conrad, P. N. First and W. A. de Heer, J. Phys. Chem. B **108**, 19912 (2004).

[3] A. H. Castro Neto and F. Guinea, Phys. Rev. B **75**, 045404 (2007).

[4] C. P. Chang, C. L. Lu, F. L. Shyu, R. B. Chen, Y. K. Fang and M. F. Lin, Carbon **42**, 2975 (2004).

[5] F. Guinea, A. H. Castro Neto and N. M. R. Peres, Phys. Rev. B **73**, 245426 (2006).

[6] S. Latil and L. henrard, Phys. Rev. Lett. **97**, 036803 (2006).

[7] E. McCann, Phys. Rev. B **74**, 161403 (2006).

[8] F. L. Shyu and M. F. Lin, J. Phys. Soc. Jpn. **69**, 607 (2000).

[9] J. H. Ho, C. P. Chang and M. F. Lin, Phys. Lett. A **352**, 446 (2006).

[10] J. H. Ho, C. L. Lu, C. C. Hwang, C. P. Chang and M. F. Lin, Phys. Rev. B 74, 085406 (2006).

[11] X. F. Wang and T. Chakraborty, Phys. Rev. B **75**, 041404 (2007).

[12] M. L. Sadowski, G. Martinez, M. Potemski, C. Berger and W. A. de Heer, Phys. Rev. Lett. **97**, 266405 (2006).

[13] A. C. Ferrari, J. C. Meyer, V. Scardaci, C. Casiraghi, M. Lazzeri, F. Mauri, S. Piscanec, D. Jiang, K. S. Novoselov, S. Roth and A. K. Geim, Phys. Rev. Lett. **97**, 187404 (2006).

[14] J. S. Bunch, Y. Yaish, M. Brink, K. Bolotin and P. L. McEuen, Nano Lett. **5**, 287 (2005).

[15] K. S. Novoselov, E. McCann, S. V. Morozov, V. I. Fal'ko, M. I. Katsnelson, U. Zeitler, D. Jiang, F. Schedin and A. K. Geim, Nature Physics **2**, 177 (2006).

[16] K. S. Novoselov, A. K. Geim, S. V. Morozov, D. Jiang, M. I. Katsnelson, I. V. Grigorieva, S. V. Dubonos and A. A. Firsov, Nature **438**, 197 (2005).

[17] Y. Zhang, Y. W. Tan, H. L. Stormer and P. Kim, Nature **438**, 201 (2005).

[18] K. S. Novoselov, Z. Jiang, Y. Zhang, S. V. Morozov, H. L. Stormer, U. Zeitler, J. C. Maan, G. S. Boebinger, P. Kim and A. K. Geim, Science **315**, 1379 (2007).

[19] V. P. Gusynin and S. G. Sharapov, Phys. Rev. Lett. **95**, 146801 (2005).

[20] E. McCann and V. I. Fal'ko, Phys. Rev. Lett. **96**, 086805 (2006).

[21] P. R. Wallace, Phys. Rev. **71**, 622 (1947).

[22] J. W. McClure, Phys. Rev. **104**, 666 (1956).

[23] F. D. Haldane, Phys. Rev. Lett. **61**, 2015 (1988).

[24] S. P. Beaumont and M. G. Blamire, Phys. Rev. Lett. **74**, 3009 (1995).

[25] P. D. Ye, D. Weiss, R. R. Gerhardts, M. Seeger, K. von Klitzing, K. Eberl and H. Nickel, Phys. Rev. Lett. **74**, 3013 (1995).

[26] Mayumi Kato, Akira Endo, Makoto Sakairi, Shingo Katsumoto and Yasuhiro Iye, Journal of the physical society of Japan **68**, 1492 (1999).

[27] S. Cina, D. M. Whittaker, D. D. Arnone, T. Burke, H. P. Hughes, M. Leadbeater, M. Pepper and D. A. Ritchie, Phys. Rev. Lett. **83**, 4425 (1999).

[28] P. Vasilopoulos and F. M. Peeters, Superlattices and Microstructures **7**, 393 (1990).

[29] F. M. Peeters and P. Vasilopoulos, Phys. Rev. B **47**, 1466 (1993).

[30] I. S. Ibrahim and F. Peeters, Phys. Rev. B **52**, 17321 (1995).

[31] Andrey Krakovsky, Phys. Rev. B **53**, 8469 (1996).

[32] A. Y. Rom, Phys. Rev. B **55**, 11025 (1997).

[33] J. M. Luttinger, Phys. Rev. **84**, 814 (1951).

[34] S. M. Stewart and C. Zhang, Semicond. Sci. Technol. **10**, 1541 (1995).

[35] S. M. Stewart and C. Zhang, Phys. Rev. B **52**, R17036 (1995).

[36] S. M. Stewart and C. Zhang, Condens. Matter **8**, 6019 (1996).

[37] H. Ajiki and T. Ando, J. Phys. Soc. Jpn. **64**, 260 (1995).

Chapter 3

Low-frequency magneto-optical excitations in a graphene monolayer

3.1 Introduction

Recently, the few-layer graphenes have been produced by the mechanical friction [1, 2] and thermal decomposition [3, 4]. They have attracted a lot of theoretical and experimental investigations on band structures [5-22], optical spectra [5, 23-29], electronic excitations [30-33], phonon spectra [34], and transport properties [35-42]. It is very appropriate to use these systems to study two-dimensional (2D) physical phenomena. A monolayer graphene is an exotic zero-gap semiconductor with a vanishing density of states (DOS) at the Fermi level $E_F = 0$, mainly owing to the hexagonal symmetry configuration. The massless Dirac electrons have been inspected by using a combination of optical microscopy, scanning electron microscopy and atomic-force microscopy [2], and by the angle-resolved photoelectron spectroscopy [43]. The electronic properties of a monolayer graphene could be effectively tuned by external electric [1, 2] and magnetic fields [1, 2, 4, 5, 20, 22, 23, 25, 29]. A uniform perpendicular magnetic field ($\mathbf{B}_0$) creates many Landau levels (LLs) and thus induces the novel half-integer quantum Hall effect [2, 35]. In this work, we mainly study the low-frequency optical excitations of a monolayer graphene in a spatially modulated magnetic field ($\mathbf{B}$). The dependence on $\mathbf{B}$ (period, strength; direction) and the polarization of an electromagnetic field is investigated. The comparison with the absorption spectra resulting from $\mathbf{B}_0$ is also made.

A 2D monolayer graphene owns many doubly degenerate parabolic bands except two nondegenerate linear bands intersecting at $E_F = 0$. Energy bands are isotropic at low energy ($\lesssim 0.5$ eV) [44], and so are the other physical properties [5]. Moreover, there is only one band-edge state in each energy dispersion. Electronic properties are strongly affected by the uniform and periodic magnetic fields. The low-energy LLs due to $\mathbf{B}_0$ display the novel dependence on the quantum number (n) and field strength (B_0); that is, their energies obey the square root form $E_n \propto \sqrt{|n|\, B_0}$. The dependence on B_0 has been identified by the magneto-optical experiments of cyclotron resonance [25]. Compared to a uniform magnetic field, the ability of a periodic magnetic field in flocking electronic states together is weaker. However, the latter could induce the rich magnetoelectronic structures [20]. The linear bands are changed into the partial flat bands at $E_F = 0$. The energy dispersions of the low-energy parabolic bands around the original band-edge state would become weaker. Each parabolic band shows four extra band-edge states and the composite behavior in state degeneracy (the double and single degeneracies at different wave vectors). The low-energy bands depend on the modulated direction of $\mathbf{B}$; furthermore, they belong to the one-dimensional energy dispersions. The main features of magnetoelectronic properties are expected to be directly reflected in optical excitations.

There are several studies on optical absorption spectra of a monolayer graphene. From the theoretical prediction, the linear valence and conduction bands do not exhibit any absorption peaks at low frequency [5]. This result is dominated by the DOS. On the other hand, the low-energy LLs in a uniform magnetic field could lead to a number of prominent symmetric absorption peaks [5]. Each peak comes from the vertical transition between the occupied LL of n $(n+1)$ and the unoccupied LL of $n+1$ (n). The magneto-optical

excitations need to obey the specific selection rule $|\Delta n| = 1$, since the magnetoelectronic wave functions (Ψ_n's) own the spatial symmetry configuration. Ψ_n is characterized by the Hermite polynomial, as seen in a 2D electron gas (2DEG). The optical selection rule has been verified by the far infrared transmission measurements [23]. Whether $|\Delta n| = 1$ is destroyed by a spatially modulated magnetic field will be examined in this work.

The Peierls tight-binding model, with the nearest-neighbor atomic interactions, is used to calculate the π-electronic structure of a monolayer graphene in a periodic magnetic field [20]. To explain the selection rules of optical excitations, the characteristics of magnetoelectronic wave functions are analyzed in detail. The optical transition elements are evaluated by the gradient approximation [5, 45-47]. This work shows that the magneto-optical absorption spectra present a lot of asymmetric pronounced peaks. Such peaks result from the original and extra band-edge states of parabolic bands. Their characters are closely related to the polarization direction and the strength, period and direction of $\mathbf{B}$. There exist some important differences for the absorption spectra in the presence of $\mathbf{B}$ and $\mathbf{B}_0$. The predicted results could be examined by the optical absorption spectroscopy.

In the next section, the π-electronic wave functions in the presence of a spatially modulated magnetic field are studied by the Peierls tight-binding model. In Sec. 3.3, the magneto-absorption spectra are calculated at different polarization directions. Meanwhile, the effects due to the field strength, period and direction are also discussed. Finally, concluding remarks are presented in Sec. 3.4.

3.2 π-electronic wave functions

A monolayer graphene is assumed to exist in a periodic magnetic field $\mathbf{B} = B\sin(Kx)\hat{z}$

along the armchair direction (the x-axis in Fig. 3.1(a)). The periodic length in a unit of the lattice constant at $B = 0$ ($3b'$) is $l_B = 2\pi/K = 3b'R_B$, where $b' = 1.42$ $\mathring{A}$ is the C-C bond length. There are $4R_B$ carbon atoms in a primitive unit cell ($2R_B$ a atoms and $2R_B$ b atoms). The magnetoelectronic structure formed by the $2p_z$ orbitals is described by the $4R_B$ tight-binding functions. $|a_{m\mathbf{k}}\rangle$ and $|b_{m\mathbf{k}}\rangle$ for $m = 1, 2...2R_B$ are, respectively, those associated with the periodical a and b atoms. The π-electronic wave function is expressed as

$$|\Psi^{c,v}_{\mathbf{k}}\rangle = \sum_{m=1}^{2R_B-1} (A^{c,v}_o|a_{m\mathbf{k}}\rangle + B^{c,v}_o|b_{m\mathbf{k}}\rangle) + \sum_{m=2}^{2R_B} (A^{c,v}_e|a_{m\mathbf{k}}\rangle + B^{c,v}_e|b_{m\mathbf{k}}\rangle)\,, \tag{3.1}$$

where o (e) represents an odd (even) integer. The superscripts c and v indicate the unoccupied conduction band and occupied valence band, respectively. $A^{c,v}_o$ ($B^{c,v}_o$) is the amplitude of the tight-binding function due to the a (b) atoms with odd indices. The Hamiltonian matrix in the subspace spanned by the tight-binding functions is a $4R_B \times 4R_B$ band-like Hermitian matrix. Only the nearest-neighbor atomic hopping integrals γ_0 (=2.56 eV) [44] is taken into account. The magnetic field would induce an extra Peierls phase between two nearest-neighbor atoms at $\mathbf{R}_{m'}$ and $\mathbf{R}_m$. Such a phase is defined as $\frac{2\pi}{\Phi_0}\int_{\mathbf{R}_{m'}}^{\mathbf{R}_m} \mathbf{A}\cdot d\mathbf{r}$, where $\mathbf{A} = -B\cos(Kx)/K\hat{y}$ is the vector potential, and $\Phi_0 = h/e$ is the flux quantum. To get the band-like Hamiltonian matrix, the $4R_B$ tight-binding functions are arranged as the following sequence $\{|a_{1\mathbf{k}}\rangle, |b_{2R_B\mathbf{k}}\rangle, |b_{1\mathbf{k}}\rangle, |a_{2R_B\mathbf{k}}\rangle, |a_{2\mathbf{k}}\rangle, |b_{2R_B-1\mathbf{k}}\rangle, |b_{2\mathbf{k}}\rangle, |a_{2R_B-1\mathbf{k}}\rangle, \ldots$ $|a_{R_B-1\mathbf{k}}\rangle,\ |b_{R_B+2\mathbf{k}}\rangle, |b_{R_B-1\mathbf{k}}\rangle, |a_{R_B+2\mathbf{k}}\rangle, |a_{R_B\mathbf{k}}\rangle, |b_{R_B+1\mathbf{k}}\rangle, |b_{R_B\mathbf{k}}\rangle; |a_{R_B+1\mathbf{k}}\rangle\}$. By the detailed calculations, the nonvanishing Hamiltonian matrix elements are

$$\langle b_{m'\mathbf{k}}|H_{\mathbf{B}}|a_{m\mathbf{k}}\rangle = [t_{1\mathbf{k}}(m) + t_{2\mathbf{k}}(m)]\delta_{m',m} + t_{3\mathbf{k}}\delta_{m',m-1}. \tag{3.2}$$

The three hopping integrals are, respectively, $t_{1\mathbf{k}}(m) = \gamma_0 \exp[\ (ik_x b'/2 + ik_y\sqrt{3}b'/2) + G_m\ ]$, $t_{2\mathbf{k}}(m) = \gamma_0 \exp[\ (ik_x b'/2 - ik_y\sqrt{3}b'/2) - G_m\ ]$, and $t_{3\mathbf{k}} = \gamma_0 \exp(-ik_x b'\ )$ ($G_m = -i[6(R_B)^2\Phi/\pi]\cos[\pi(m-5/6)/R_B]\sin(\pi/6R_B)$). The similar equations could be obtained for the periodic magnetic field along the zigzag direction.

The energy dispersions $E^{c,v}(\mathbf{k},\widetilde{n})$'s are obtained by diagonalizing the Hamiltonian, where $\widetilde{n}$ represents the subband index measured from the Fermi level. The low-energy bands are drastically changed by the modulated magnetic field, as shown in Fig. 3.1(b) at $R_B = 750$ and $B = 4$ T along the armchair direction. The unoccupied conduction bands are symmetric to the occupied valence bands about $E_F = 0$. The dependence of energy bands on k_x is negligible compared with that on k_y. A periodic magnetic field, with a sufficient large period, could effectively reduce the dimensionality by one. The k_y-dependent energy bands exhibit partial flat bands at $E_F = 0$ and parabolic bands at others. Each parabolic band owns one original band-edge state (k_y^{pp}) and four extra band-edge states (k_y^{sp}'s). The former is situated at the fixed wave vector $k_y^{pp} = 2\pi/3\sqrt{3}b'$, which is the same with that in the $\mathbf{B} = 0$ case [20]. However, the latter depend on the period and strength of $\mathbf{B}$. The parabolic bands close to k_y^{pp} and k_y^{sp}'s are, respectively, doubly degenerate and nondegenerate. The very weak energy dispersions near k_y^{pp} mean that the ability of the periodic and uniform magnetic fields in flocking electronic states together is similar. Such energy bands could be regarded as the quasi-Landau levels (QLLs), as indicated from the characteristics of wave functions.

The main features of wave functions could be utilized to define the quantum number of QLLs. Carbon atoms, with odd and even indices, make equal contributions to wave functions. The tight-binding functions associated with these atoms in Eq. (3.1) have

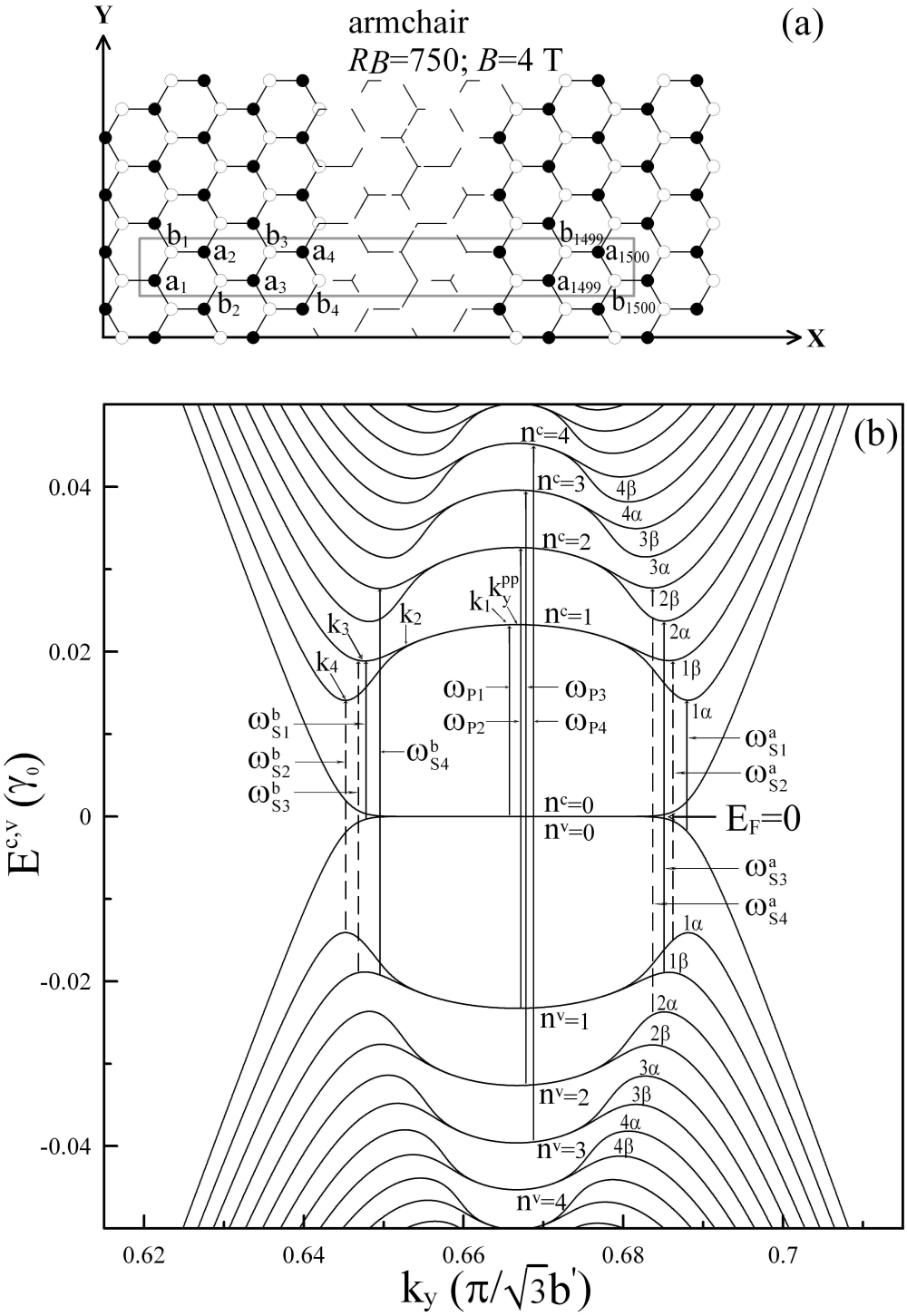

Figure 3.1. (a) The primitive unit cell of a monolayer graphene in a periodic magnetic field with a period $R_B = 750$ along the armchair direction. (b) The energy bands for the field strength $B = 4$ T.

the opposite amplitudes; that is, $A_o^{c,v} = -A_e^{c,v}$ and $B_o^{c,v} = -B_e^{c,v}$. Only discussing the amplitudes $A_o^{c,v}$ and $B_o^{c,v}$ is appropriate in understanding the wave functions. We first see the wave function of the lowest unoccupied QLL ($\widetilde{n} = 1$ or $n^c = 0$) at k_y^{pp}. The position-dependent A_o^c and B_o^c, as shown in Figs. 3.2(a) and 3.2(g) by the solid circles, mainly come from the $2p_z$ orbitals centered at one-fourth ($x_1 = a_m/2R_B = 1/4$) and three-fourths ($x_2 = b_m/2R_B = 3/4$) of a primitive unit cell, respectively. The positions x_1 and x_2 correspond to the maximum field strength. The wave function of the lowest unoccupied QLL is similar to that of the highest occupied QLL ($n^v = 0$ by the open circles in Figs. 3.2(a) and 3.2(g)). Their main difference lies in the interchange of the localization positions of $A_o^{c,v}$ and $B_o^{c,v}$. Such interchange might include the sign change of the values. The distribution width of the localization function (l_B), that is, the full width at half-maximum, is comparable to the magnetic length ($\sqrt{\hbar/eB}$), e.g., $l_B \approx 200$ $\mathring{A}$ at $B = 4$ T. Also note that the two LLs at $E_F = 0$ due to a uniform magnetic field could display the similar characteristics [22].

There are two important differences between the second and first (lowest) unoccupied QLLs at k_y^{pp}. The former, as shown in Figs. 3.2(b) and 3.2(h), is doubly degenerate. Moreover, it is composed of two tight-binding functions centered at x_1 and x_2. A_o^c (B_o^c) has two subenvelope functions $A_o^c(x_1)$ ($B_o^c(x_1)$) and $A_o^c(x_2)$ ($B_o^c(x_2)$) located at $x_1 = 1/4$ and $x_2 = 3/4$, respectively. The oscillatory $A_o^c(x_1)$ ($B_o^c(x_2)$) owns one zero point, while the monotonic $A_o^c(x_2)$ ($B_o^c(x_1)$) has none zero point. Their contributions to wave functions are nearly comparable. The number of zero point (n), which stands for the spatial symmetry of the carrier density, could be chosen to characterize the wave functions. The effective quantum number (n^c) is defined by the larger number of zero point; that is, $n^c = 1$

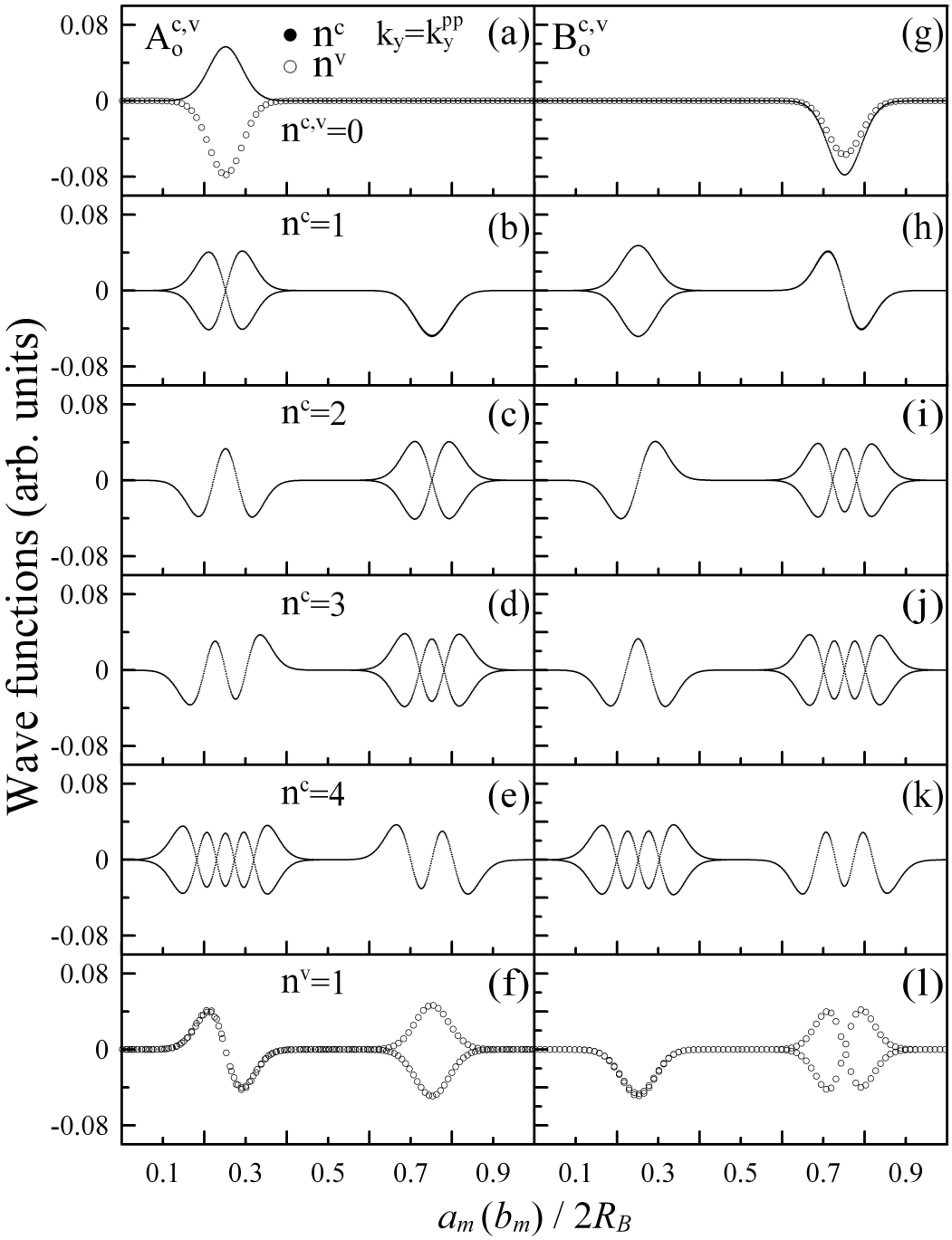

Figure 3.2. The wave functions contributed by the (a)∼(f) $A_o^{c,v}$ and (g)∼(l) $B_o^{c,v}$ atoms with odd integer indices for original band-edge states of the low-energy bands.

is chosen for the second unoccupied QLL. Such a choice does not influence the specific selection rules of the optical absorption spectra. In addition, the twofold degenerate QLLs have the similar wave functions, their difference is only the sign change of the subenvelope functions. By the definition of n^c, the first unoccupied QLL without zero point is thus defined as the $n^c = 0$ state. The number of zero point will become larger with the increase of state energy, i.e., n^c also increases gradually as the unoccupied QLLs are away from $E_F = 0$ (Figs. 3.2(a)$\sim$3.2(e), and 3.2(g)$\sim$3.2(k)). The $\widetilde{n}$th unoccupied QLL owns two modes of subenvelope functions with $n = \widetilde{n} - 1$ and $n = \widetilde{n} - 2$, respectively. That n^c is just equal to $\widetilde{n} - 1$ is very convenient in defining the unoccupied QLLs (Fig. 3.1(b)). Furthermore, the second occupied QLL could also reveal the similar features to those in the second unoccupied QLL, as shown in Figs. 3.2(f) and 3.2(l). They have the same effective quantum number ($n^v = n^c = 1$) and localization positions. Their main difference is the same as that of $n^c = 0$ case. The other $\widetilde{n}$th occupied and unoccupied QLLs also demonstrate the similar behavior. Accordingly, it is reasonable only to discuss the $\widetilde{n}$th unoccupied QLLs.

The monolayer graphene owns many low-energy dispersionless LLs in the presence of a uniform perpendicular magnetic field. The wave functions of LLs could be represented by the linear combination of those from the harmonic oscillator [7, 46]. After the well fitting, the $\widetilde{n}$th QLLs and LLs show the similar characteristics, e.g., the same oscillatory behavior, effective quantum number, and distribution width. Such similarities imply that the wave functions of the former could be approximately expressed as those of the latter. Therefore,

$A_o^{c,v}$ and $B_o^{c,v}$ of the $\widetilde{n}$th QLL in Eq. (3.1) are written as

$$A_o^{c,v} \propto e^{\pm ik_y y}\varphi_0(x_1)\,;\; B_o^{c,v} \propto e^{\pm ik_y y}\varphi_0(x_2) \;\text{ for } \widetilde{n}=1. \tag{3.3a}$$

$$A_o^{c,v} \propto e^{\pm ik_y y}\left[\varphi_{n^{c,v}}(x_1) \pm \varphi_{n^{c,v}-1}(x_2)\right]\,;\; B_o^{c,v} \propto e^{\pm ik_y y}\left[\varphi_{n^{c,v}-1}(x_1) \pm \varphi_{n^{c,v}}(x_2)\right] \;\text{ for } \widetilde{n}>1. \tag{3.3b}$$

The subenvelope function $\varphi_n(x)$ is the product of the nth-order Hermite polynomial and Gaussian function [7, 46].

The wave functions would be strongly modified as the wave vectors gradually move away from the original band-edge state. The wave functions at the left- and right-side wave vectors around k_y^{pp} have the similar characteristics, and thus only the former are discussed in the following part. For example, $A_o^c(x_1)$ ($B_o^c(x_1)$) and $A_o^c(x_2)$ ($B_o^c(x_2)$) of the second unoccupied QLL at k_1 (indicated in Fig. 3.1(b)) are centered at, respectively, $x_1 = 3/10$ and $x_2 = 7/10$, as shown in Figs. 3.3(a) and 3.3(i). They still maintain the same characteristics with those at k_y^{pp}, while the distance between them ($|x_1 - x_2| = 2/5$) is shorter than that ($|x_1 - x_2| = 1/2$) at k_y^{pp}. At $k_y = k_2$, the doubly degenerate QLL is going to separate into two subbands. $x_1 \approx 7/20$ and $x_2 \approx 13/20$ are so close that $A_o^c(x_1)$ ($B_o^c(x_1)$) and $A_o^c(x_2)$ ($B_o^c(x_2)$) nearly overlap, as shown in Figs. 3.3(b) and 3.3(j). Besides, one of the tight-binding functions has the opposite sign to that at k_1, i.e., A_o^c (B_o^c) might change its sign at some appropriate wave vectors. k_3 and k_4 are, respectively, the band-edge states (k_y^{sp}'s) of the higher and lower subbands. Their wave functions display the similar behavior (Figs. 3.3(c) and 3.3(k); 3.3(d) and 3.3(l)). The second unoccupied QLL at k_3 is divided into two nondegenerate subbands, i.e., the 1α and 1β subbands. The subenvelope functions of the 1α state, as shown in Figs. 3.3(c) and 3.3(k) by the solid circles, exhibit more overlap behavior. It implies that there would be strong overlap in the subenvelope

functions at k_y^{sp}'s. Such a behavior would dominate the optical excitation strength. The centered positions x_1 and x_2 are close to half of a primitive unit cell, i.e., they correspond to the nearly zero magnetic field strength. In other words, the carriers will move from the position of the maximum magnetic field strength to that of the minimum magnetic field strength. The 1β (the open circles in Figs. 3.3(c) and 3.3(k)) and 1α subbands have the similar overlap behavior. However, $A_o^c(x_1)$ ($B_o^c(x_1)$) and $A_o^c(x_2)$ ($B_o^c(x_2)$) of the former display the stronger overlap than those of the latter. It results from the fact that k_3 is the extra band-edge state of the 1β subband, but not that of the 1α subband. Furthermore, the two states reveal the different linear combinations of $A_o^c(x_1)$ ($B_o^c(x_1)$) and $A_o^c(x_2)$ ($B_o^c(x_2)$). A_o^c (B_o^c) of the 1α and 1β states could be roughly regarded as, respectively, the combination of $\varphi_1(x_1) - \varphi_0(x_2)$ ($\varphi_0(x_1) + \varphi_1(x_2)$) and of $\varphi_1(x_1) + \varphi_0(x_2)$ ($\varphi_0(x_1) - \varphi_1(x_2)$); that is, they might show the different spatial symmetries. The wave functions of the extra band-edge states have the dissimilar characteristics to those of the original band-edge state. Since the former exhibit the overlap behavior, the localized feature of QLLs is thoroughly destroyed at k_y^{sp}'s. Such properties would be reflected on the optical absorption spectra. The wave functions of the 2α (2β) subband (Figs. 3.3(g), 3.3(h), 3.3(o), and 3.3(p)) also display the similar features as those of the 1α (1β) subband, i.e., the similar localization positions, linear combination, and the overlap behavior of the subenvelope functions. The other $\widetilde{n}$th α and β subbands also present the similar characteristics. The above-mentioned characteristics of wave functions could be utilized to investigate the selection rules of the optical absorption spectra.

3.3 Magneto-optical absorption spectra

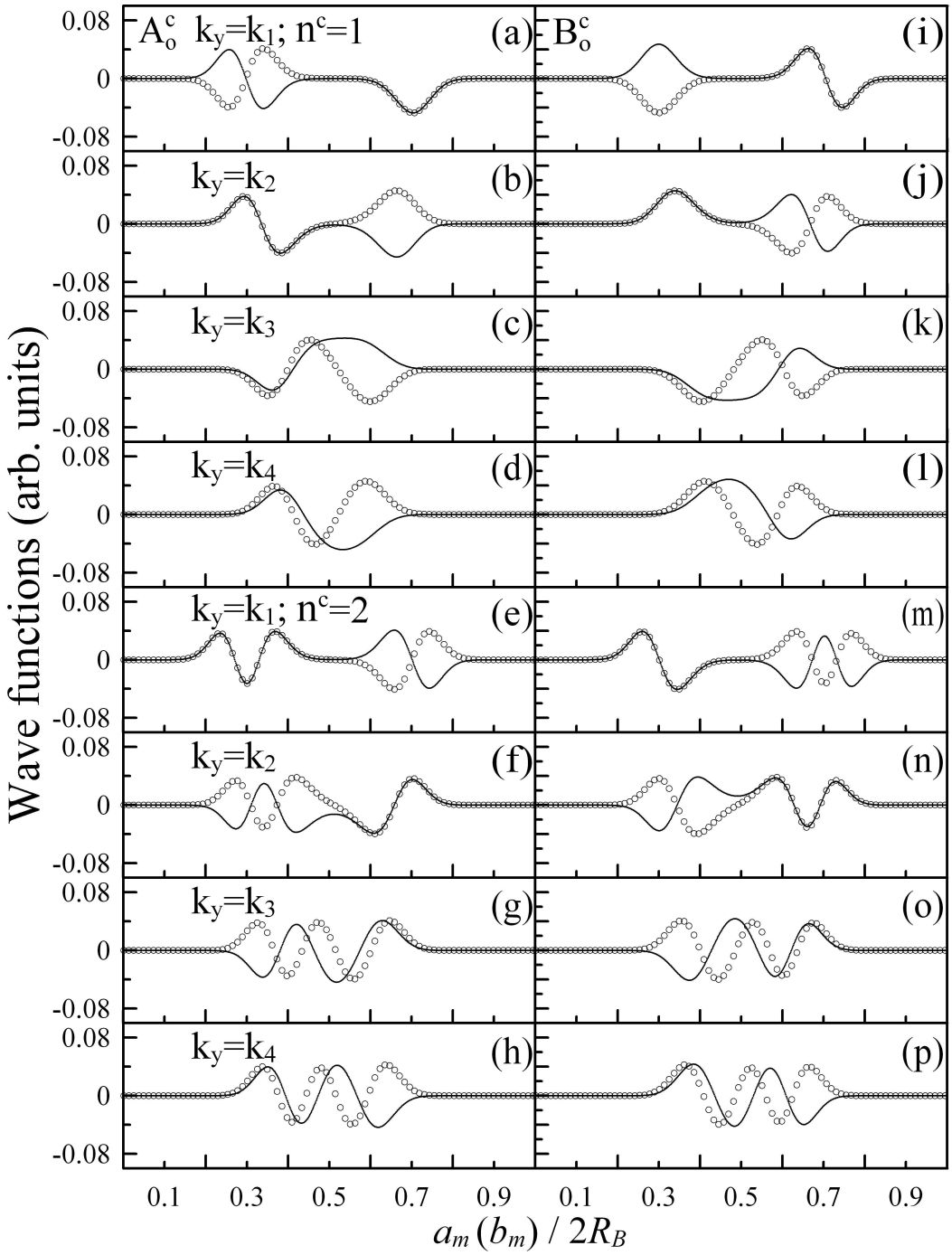

Figure 3.3. Same plots as Fig. 2, but shown for the second and third conduction bands at different k_y's.

The main features of electronic properties can be directly manifested by the optical excitations. When a monolayer graphene is excited from the occupied valence to unoccupied conduction bands (the inter-π-band excitation) by an electromagnetic field, there are only inter-π-band excitations at zero temperature. The optical selection rules $\Delta \mathbf{k}_x = \mathbf{0}$ and $\Delta \mathbf{k}_y = \mathbf{0}$ due to the vertical transitions are mainly determined by the zero momentum of photon. Based on the Fermi's golden rule, the optical absorption function is given by

$$A(\omega) \propto \sum_{c,v,\widetilde{n},\widetilde{n}'} \int_{1stBZ} \frac{d\mathbf{k}}{(2\pi)^2} \left| \left\langle \Psi^c(\mathbf{k},\widetilde{n}) \left| \frac{\widehat{\mathbf{E}} \cdot \mathbf{P}}{m_e} \right| \Psi^v(\mathbf{k},\widetilde{n}') \right\rangle \right|^2 \times Im \left[\frac{f(E^c(\mathbf{k},\widetilde{n})) - f(E^v(\mathbf{k},\widetilde{n}'))}{E^c(\mathbf{k},\widetilde{n}) - E^v(\mathbf{k},\widetilde{n}') - \omega - i\Gamma} \right], \tag{3.4}$$

where $f(E(\mathbf{k},\widetilde{n}))$ is the Fermi-Dirac distribution function. $\widehat{\mathbf{E}}$ is the unit vector of an electric polarization. The parallel and perpendicular polarization directions, $\widehat{\mathbf{E}} \parallel \widehat{x}$ and $\widehat{\mathbf{E}} \perp \widehat{x}$, are taken into account. The velocity matrix element $M^{cv} = \left\langle \Psi^c(\mathbf{k},\widetilde{n}) \left| \widehat{\mathbf{E}} \cdot \mathbf{P}/m_e \right| \Psi^v(\mathbf{k},\widetilde{n}') \right\rangle$ is calculated from the gradient approximation. It is approximated by taking the gradient of the Hamiltonian matrix element versus the wave vector k_x or k_y. Similar approximations have been successful in studying the optical properties of the carbon nanotubes [45], nanographite ribbons [46], graphite [5], and graphite intercalation compounds [47]. Moreover, by substituting Eq. (3.1) into the velocity matrix element, M^{cv} is expressed as

$$\sum_{m,m'=1}^{2R_B} \left[(A_o^c + A_e^c)^* \times (B_{o'}^v + B_{e'}^v) + (B_o^c + B_e^c)^* \times (A_{o'}^v + A_{e'}^v) \right] \nabla_k \langle a_{m\mathbf{k}} | H_B | b_{m'\mathbf{k}} \rangle . \tag{3.5}$$

The indices o (e) and o' (e') are, respectively, the odd (even) integers of m and m'. For convenience, the value of $(A_o^c + A_e^c)^* \times (B_{o'}^v + B_{e'}^v) + (B_o^c + B_e^c)^* \times (A_{o'}^v + A_{e'}^v)$ is represented

by M_{AB}^{cv}. The absolute values of $\nabla_k \langle a_{m\mathbf{k}} | H_B | b_{m'\mathbf{k}} \rangle$ for two polarization directions are

$$M_x^{cv} = \left| b'\gamma_0 \left[\cos\left(\sqrt{3}b'k_y/2 + G_m \right) - 1 \right] \right| \text{ for } \widehat{\mathbf{E}} \parallel \widehat{x}; \tag{3.6a}$$

$$M_y^{cv} = \left| \sqrt{3}b'\gamma_0 \sin\left(\sqrt{3}b'k_y/2 + G_m \right) \right| \text{ for } \widehat{\mathbf{E}} \perp \widehat{x}. \tag{3.6b}$$

The optical properties are closely related to the number and strength of excitation channels. The joint density of states (D_J) reflects the number of excitation channels. D_J is defined by setting the velocity matrix element in Eq. (3.4) to one. When the optical excitations come from the band-edge states, D_J would exhibit the prominent peak structures. The low-frequency D_J at $B = 0$ has no special structures. It vanishes at $\omega = 0$ and linearly grows with the increasing frequency (not shown; [5]). The low-energy 2D linear bands do not induce any optical absorption peaks. D_J is strongly affected by the periodic magnetic field. Fig. 3.4(a) shows D_J's for $R_B = 750$ and different field strengths along the armchair direction. They display a lot of peak structures. The peak height is enhanced with the increase of the field strength. The peaks at $\omega = 0$ mainly result from the excitation channel between the two QLLs at $E_F = 0$. The other peaks are dominated by the excitation channels from the original band-edge and extra band-edge states. The similar results for different R_B's and the zigzag direction at $B = 4$ T are also shown in Fig. 3.4(b).

The optical absorption spectrum quite differs from the joint density of states after introducing the velocity matrix element. The low-frequency spectral functions for $R_B = 750$ at different B's along the armchair direction with $\widehat{\mathbf{E}} \parallel \widehat{x}$ are shown in Fig. 3.5(a). The periodic magnetic field has a strong effect on the spectral function. Each $A(\omega)$ exhibits rich asymmetric peaks (in the square-root divergent form at $\Gamma \to 0$). These peaks could

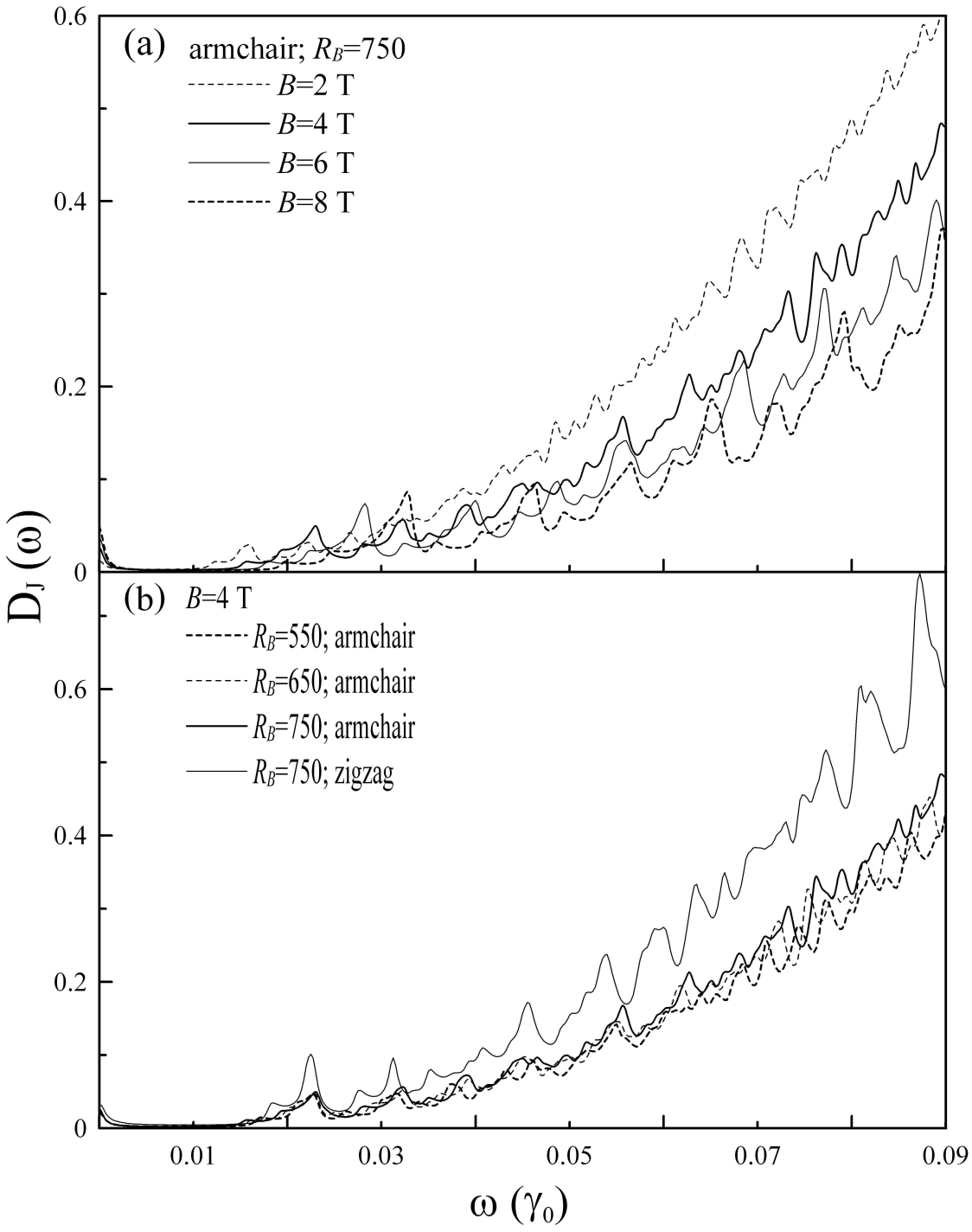

Figure 3.4. The optical joint density of states for a spatially modulated magnetic field along the armchair direction at (a) $R_B = 750$ and different B's; (b) $B = 4$ T and different R_B's. That along the zigzag direction at $B = 4$ T and $R_B = 750$ is also shown in (b).

be further divided into the principal peaks (ω_P's) and the subpeaks (ω_S's) according to the optical excitations resulting from the original band-edge and extra band-edge states, respectively. As the field strength rises, the peak height and frequency of the principal peaks (subpeaks) increase, and the peak number decreases. These results mean that the ability in flocking electronic states together is enhanced as the field strength grows. What is worth mentioning is that ω_S's could be further classified into two subgroups ω_S^a's and ω_S^b's because of the two kinds of subbands α and β. ω_S^a's and ω_S^b's primarily come from the excitations of α (β) to β (α) and α (β) to α (β), respectively. The peak heights of the former are very low compared with those of the latter. The zero velocity matrix elements between two QLLs at $E_F = 0$ make $A(\omega)$ vanish at $\omega = 0$. The optical excitation channel caused by the two QLLs is forbidden.

In addition to the field strength, the optical absorption spectrum is also influenced by the modulated period. Fig. 3.5(b) shows the optical spectra of $B = 4$ T for different R_B's along the armchair direction. The subpeaks ω_S^a's (ω_S^b's) strongly depend on the period, i.e., they present different peak heights and frequencies at different R_B's. Concerning the case of principal peaks, their peak heights rise with the increase of the period, and their frequencies present the weak dependence on R_B. As the period grows, the electronic states tend to flock together in QLLs, and some states of the nondegenerate subbands become QLLs. Moreover, the energy dispersions of QLLs near k_y^{pp} and the energy difference between two subbands near k_y^{sp}'s are reduced. The changes of energy bands could account for the dependence of optical absorption peaks on R_B.

The low-energy optical absorption spectra could exhibit the anisotropic feature in the presence of a modulated magnetic field. $A(\omega)$ of $R_B = 750$ at $B = 4$ T along the zigzag

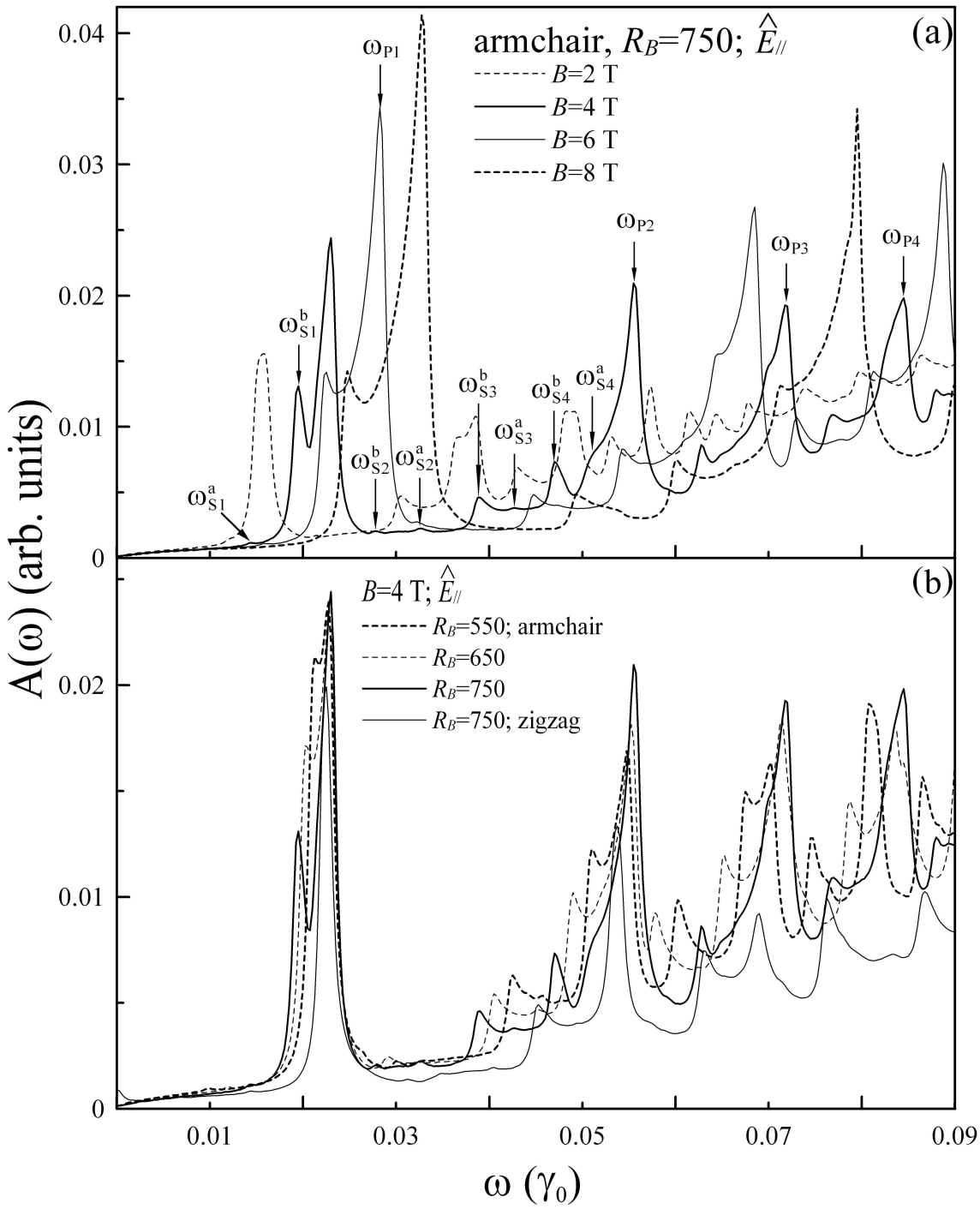

Figure 3.5. The optical absorption spectra with the electric polarization parallel to the modulated direction. They are calculated for the armchair direction at (a) $R_B = 750$ and different B's; (b) $B = 4$ T and different R_B's. That for the zigzag direction is also evaluated at (b) $B = 4$ T and $R_B = 750$.

direction is shown in Fig. 3.5(b) by the thin solid curve. ω_{P1}'s of the two modulated directions own the same energy, while the other ω_{Pn}'s do not (Fig. 3.5(b)). The peak height of each principal peak from the zigzag direction is lower than that from the armchair direction. As to the subpeaks, their peak heights and frequencies are dissimilar to those from the armchair direction. The above-mentioned differences directly reflect the fact that the energy bands of the two modulated directions are anisotropic [20], and the ability in flocking electronic states together for the armchair direction is stronger than that for the zigzag direction at the same period and field strength. These important differences imply that the low-frequency optical absorption spectra in a modulated magnetic field could induce the anisotropic behavior. This result quite differs from those of a monolayer graphene in the absence of an external field [5] or in the presence of a uniform perpendicular magnetic field [5].

Besides the field strength, period, and direction of a modulated magnetic field, the polarization direction of an EM wave also affects the optical absorption spectra. $A(\omega)$'s of the perpendicular polarization direction reveal somewhat different characteristics from those of the parallel polarization direction, especially in the subpeaks. Fig. (3.6) shows the similar plots to $\widehat{\mathbf{E}} \perp \widehat{x}$ as those of $\widehat{\mathbf{E}} \parallel \widehat{x}$ in Fig. (3.5). The principal peaks which correspond to two polarization directions display similar features at the same R_B's and B's, e.g., approximately the same absorption frequency, peak height, and peak number. That is to say, ω_P's show very weak dependence on the electric polarization direction. However, the intensity of subpeaks relies strongly on the polarization direction. As to $\widehat{\mathbf{E}} \perp \widehat{x}$, the subpeaks of ω_S^a's are much stronger than those of ω_S^b's. The opposite is true for the $\widehat{\mathbf{E}} \parallel \widehat{x}$ case. Such an important difference might be attributed to the characteristics of

the velocity matrix elements, which will be discussed in the following paragraph.

The optical excitations of each low-energy absorption peak could be clearly identified. For example, the transition channels of the first four principal peaks resulting from the original band-edge state denoted as ω_{P1},$\cdots$, and ω_{P4} in Figs. (3.5) and (3.6) are indicated in Fig. 3.1(b). Each prominent peak comes from two different excitation channels. The first peak ω_{P1} is mainly due to the transition from the first occupied QLL of $n^v = 0$ to the second unoccupied QLL of $n^c = 1$. Peaks ω_{P2}, ω_{P3}, and ω_{P4} correspond to the excitations of $n^v = 1$ to $n^c = 2$, $n^v = 2$ to $n^c = 3$, and $n^v = 3$ to $n^c = 4$, respectively. Because of the symmetry between the conduction and valence bands about the Fermi level, another kind of excitation channel, $n^v = n+1$ to $n^c = n$, exhibits the same optical absorption spectrum. As a result, the selection rule could be simply represented by $|\Delta n| = |n^c - n^v| = 1$. It means that the two kinds of transitions originating in QLLs, $n^v = n-1$ to $n^c = n$ and $n^v = n$ to $n^c = n-1$ at k_y^{pp}, lead to the nth principal peak with frequency ω_{Pn}.

The subpeaks originating in the extra band-edge states display more complex behavior. The excitation channels of the first eight subpeaks (ω_{S1}^a,$\cdots$, ω_{S4}^a; ω_{S1}^b,$\cdots$, ω_{S4}^b in Figs. (3.5) and (3.6)) are shown in Fig. 3.1(b). ω_S^a and ω_S^b could be further divided into two classes in terms of the difference between n^c and n^v. For example, the peak ω_{S1}^a is primarily due to the transition from the first occupied QLL (the occupied 1α subband) to the unoccupied 1α subband (the first unoccupied QLL) at $k_y^{sp,1\alpha}$. $k_y^{sp,n\alpha}$ ($k_y^{sp,n\beta}$) is the band-edge state of the nth α (β) subband. The peak ω_{S3}^a mainly comes from the excitations of 1α to 2β (2β to 1α) at $k_y^{sp,1\alpha}$ and $k_y^{sp,2\beta}$, and the excitations of 1β to 2α (2α to 1β) at $k_y^{sp,1\beta}$ and $k_y^{sp,2\alpha}$. The difference between n^c and n^v of ω_{S1}^a (ω_{S3}^a) is $|\Delta n| = 1$, and such a difference is also observed in the principal peaks. The transitions from 1α to 1β (1β to 1α) at $k_y^{sp,1\alpha}$

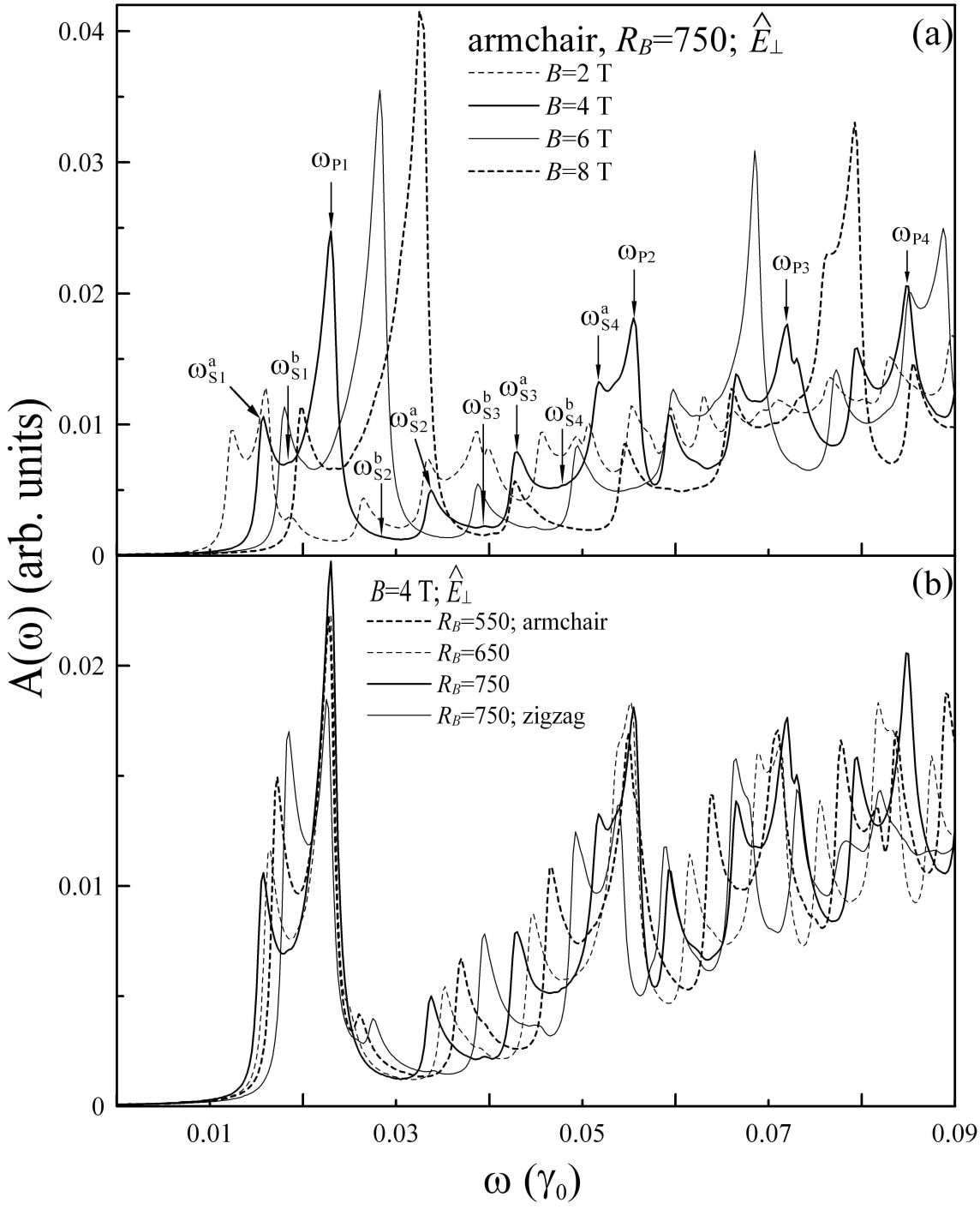

Figure 3.6. Same plot as Fig. 5, but shown for the electric polarization perpendicular to the modulated direction.

and $k_y^{sp,1\beta}$ and from 2α to 2β (2β to 2α) at $k_y^{sp,2\alpha}$ and $k_y^{sp,2\beta}$, lead to, respectively, the peaks ω_{S2}^a, and ω_{S4}^a. n^c and n^v of the peak ω_{S2}^a (ω_{S4}^a) own the same effective quantum number, i.e., $|\Delta n| = 0$, which is very distinct from the selection rule of the principal peaks. The excitation frequencies of $n\alpha$ to $n\beta$ ($n\alpha$ to $(n+1)\,\beta$; $n\beta$ to $(n+1)\,\alpha$) are identical to those of $n\beta$ to $n\alpha$ ($(n+1)\,\beta$ to $n\alpha$; $(n+1)\,\alpha$ to $n\beta$) at the same band-edge state. This is caused by the symmetry between the conduction and valence bands about $E_F = 0$. It is worth noting that, in the low-energy spectra, the transition channels of $n\alpha$ to $n\beta$ at two band-edge states $k_y^{sp,n\alpha}$ and $k_y^{sp,n\beta}$ ($n\alpha$ to $(n+1)\,\beta$ at $k_y^{sp,n\alpha}$ and $k_y^{sp,n+1\beta}$; $n\beta$ to $(n+1)\,\alpha$ at $k_y^{sp,n\beta}$ and $k_y^{sp,n+1\alpha}$) have nearly the same excitation frequencies. Therefore, the peaks corresponding to these excitations are undistinguishable in Figs. (3.5) and (3.6). Furthermore, the transition channels of ω_S^a's could be divided into two classes. They are the excitations of α (β) to β (α) subbands with $|\Delta n| = 1$ and $|\Delta n| = 0$ except for the first peak ω_{S1}^a originating in the transition channel from the first occupied QLL (the occupied 1α subband) to the unoccupied 1α subband (the first unoccupied QLL).

ω_S^b's also present the similar behavior as that of ω_S^a's. The peak ω_{S1}^b is mainly due to the transition from the first occupied QLL (the occupied 1β subband) to the unoccupied 1β subband (the first unoccupied QLL) at $k_y^{sp,1\beta}$. The excitation of 1α to 1α at $k_y^{sp,1\alpha}$ results in the peak ω_{S2}^b. The excitation energy of 1α to 2α (2α to 1α) at $k_y^{sp,1\alpha}$ almost equals that of 1α to 2α (2α to 1α) at $k_y^{sp,2\alpha}$ and of 1β to 1β at $k_y^{sp,1\beta}$. These transition channels with approximately the same energy lead to the peak ω_{S3}^b. The peak ω_{S4}^b comes from the excitations of 1β to 2β (2β to 1β) at $k_y^{sp,1\beta}$ and $k_y^{sp,2\beta}$ and from the excitations of 2α to 2α at $k_y^{sp,2\alpha}$. ω_S^b's are also simply classified into two categories. They mainly originate in the transition channels from α to α (β to β) with $|\Delta n| = 1$ and $|\Delta n| = 0$ except for the

first peak ω_{S1}^{b} corresponding to the excitation of the first occupied QLL (the occupied 1β subband) to the unoccupied 1β subband (the first unoccupied QLL). The excitations of the two subgroups ω_{S}^{a}'s and ω_{S}^{b}'s form all transition channels with $|\Delta n| = 1$ and $|\Delta n| = 0$. That is to say, the selection rule of subpeaks is characterized by $|\Delta n| = 1$ and $|\Delta n| = 0$. Such a rule quite differs from that of principal peaks. The reason could be ascribed to the overlap behavior of wave functions at the extra band-edge states.

The velocity matrix element could govern the transition channels of the optical absorption spectra, i.e., the selection rules might be determined by the characteristics of M^{cv}. In Eq. (3.5), M^{cv} is decided by the product of M_{AB}^{cv} and $\nabla_k \langle a_{m\mathbf{k}} | H_B | b_{m'\mathbf{k}} \rangle$. M_{AB}^{cv} depends on the effective quantum number, not on the polarization direction. The value of $\nabla_k \langle a_{m\mathbf{k}} | H_B | b_{m'\mathbf{k}} \rangle$ (Eqs. (3.6a) and (3.6b)), on the other hand, is strongly related to the polarization direction. In the case of principal peaks, $A_{o,e}^{c,v}(x_1)$ ($A_{o,e}^{c,v}(x_2)$) and $B_{o,e}^{c,v}(x_1)$ ($B_{o,e}^{c,v}(x_2)$) of the nth QLLs own the effective quantum number $n-1$ ($n-2$) and $n-2$ ($n-1$), respectively, as shown in Fig. (3.2). As for the nth occupied and unoccupied QLLs, M_{AB}^{cv} is proportional to $[\varphi_{n-1}(x_1) + \varphi_{n-2}(x_2) \times \varphi_{n-2}^{*}(x_1) + \varphi_{n-1}^{*}(x_2)]$ (by the definition of Eq. (3.3)). Its value vanishes because of the orthogonality of $\varphi_n(x)$. The optical excitations between the occupied and unoccupied QLLs with the same effective quantum number at k_y^{pp} are forbidden. $A_{o,e}^{c,v}(x_1)$ of the nth QLL ($A_{o,e}^{c,v}(x_2)$ of the $(n+1)$th QLL) and $B_{o,e}^{c,v}(x_1)$ of the $(n+1)$th QLL ($B_{o,e}^{c,v}(x_2)$ of the nth QLL) exhibit the same effective quantum number. M_{AB}^{cv} has a finite value between the nth occupied and $(n+1)$th ($(n-1)$th) unoccupied QLLs. In addition, by the numerical analysis, the absolute values of $\nabla_k \langle a_{m\mathbf{k}} | H_B | b_{m'\mathbf{k}} \rangle$ at k_y^{pp} for two polarization directions are almost equal. It indicates that the principal peaks of $\widehat{\mathbf{E}} \perp \widehat{x}$ and $\widehat{\mathbf{E}} \parallel \widehat{x}$ have nearly the same peak height under $|\Delta n| = 1$. Concerning other

$|\Delta n|$ cases, all the values of M^{cv} for both polarization directions are disappeared due to the orthogonality of $\varphi_n(x)$. The selection rule is thus simply expressed as $|\Delta n| = 1$. This consequence is as same as that of the LLs originating in a uniform perpendicular magnetic field [7, 23, 25]. That the main features of wave functions at k_y^{pp} resemble those of $\mathbf{B}_0$ is the most important reason. However, there are certain important differences between QLLs and LLs. The former show the asymmetric square-root peaks, and the latter own the symmetric delta-function-like peaks. The peak height of QLLs is lower than that of LLs. The peak frequency of QLLs is weakly dependent on the modulated period. Furthermore, the low-frequency optical absorption spectra of QLLs could reveal the anisotropic features in the different modulated directions.

The velocity matrix elements at extra band-edge states display different characteristics from those at k_y^{pp} based on the overlap behavior of wave functions. At k_y^{sp}'s, $A_{o,e}^{c,v}(x_1)$ ($B_{o,e}^{c,v}(x_1)$) and $A_{o,e}^{c,v}(x_2)$ ($B_{o,e}^{c,v}(x_2)$) have the partial overlap (Fig. (3.3)). $A_{o,e}^{c,v}(x_1)$ ($A_{o,e}^{c,v}(x_2)$) and $B_{o,e}^{c,v}(x_1)$ ($B_{o,e}^{c,v}(x_2)$) of the nth QLLs own the effective quantum number $n-1$ ($n-2$) and $n-2$ ($n-1$), respectively. M_{AB}^{cv} of $|\Delta n| = 0$ does not disappear because of $\varphi_{n-1}(x_1) \times \varphi_{n-1}^*(x_2) \neq 0$ and $\varphi_{n-2}(x_1) \times \varphi_{n-2}^*(x_2) \neq 0$. Thus the optical absorption spectra present the subpeaks with $|\Delta n| = 0$. Obviously, such peaks are mainly owing to the overlap behavior of wave functions at extra band-edge states. M_{AB}^{cv} also has a finite value for $|\Delta n| = 1$, while it vanishes in the $|\Delta n| \neq 0$ and $|\Delta n| \neq 1$ cases. In addition to the value of M_{AB}^{cv}, that of $\nabla_k \langle a_{m\mathbf{k}} | H_B | b_{m'\mathbf{k}} \rangle$ also dominates the subpeak intensity. It strongly depends on the polarization direction, i.e., the peak height of $\widehat{\mathbf{E}} \parallel \widehat{x}$ is very different from that of $\widehat{\mathbf{E}} \perp \widehat{x}$. Eqs. (3.6a) and (3.6b) are the absolute values of $\nabla_k \langle a_{m\mathbf{k}} | H_B | b_{m'\mathbf{k}} \rangle$ for $\widehat{\mathbf{E}} \parallel \widehat{x}$ and $\widehat{\mathbf{E}} \perp \widehat{x}$, respectively. By the numerical calculation, M_x^{cv} is much larger than

M_y^{cv} ($M_y^{cv} \simeq 0$) between the occupied α (β) to unoccupied α (β) states with $|\Delta n| = 0$ and $|\Delta n| = 1$. However, M_x^{cv} and M_y^{cv} display the opposite behavior for the transition channels from the occupied α (β) to unoccupied β (α) states with $|\Delta n| = 0$ and $|\Delta n| = 1$. The difference might be ascribed to the fact that M_x^{cv} and M_y^{cv} are the sine and cosine functions, respectively. M_x^{cv}'s (M_y^{cv}'s) of the excitation channels from α (β) to α (β) and from α (β) to β (α) at extra band-edge states have, respectively, the maximum (minimum) and minimum (maximum) values. That makes ω_S^a's and ω_S^b's exhibit different peak heights for two polarization directions. The subpeaks could reflect the anisotropic feature of the electric polarization direction, while the opposite is true for the principal peaks.

The frequency of principal peaks in the optical absorption spectra deserves a closer investigation. The relation between the frequencies of the first four principal peaks and the period along the armchair direction is shown in Fig. 3.7(a). Energies of ω_P's present very weak dependence on the period as R_B becomes large enough. However, ω_P's strongly rely on the field strength, i.e., their energies grow with the increase of B, as shown in Fig. 3.7(b). As to the zigzag direction, ω_P's exhibit different frequencies from those of the armchair direction, i.e., they have the anisotropic behavior in the modulated direction. However, they display similar dependence of energies on the field strength and period (not shown in the zigzag direction). The predicted results could be verified by the optical spectroscopy [23, 25, 29].

3.4 Summary and conclusions

A monolayer graphene is assumed to exist in a periodic magnetic field. The low-frequency optical absorption spectra are studied by the Peierls tight-binding model and

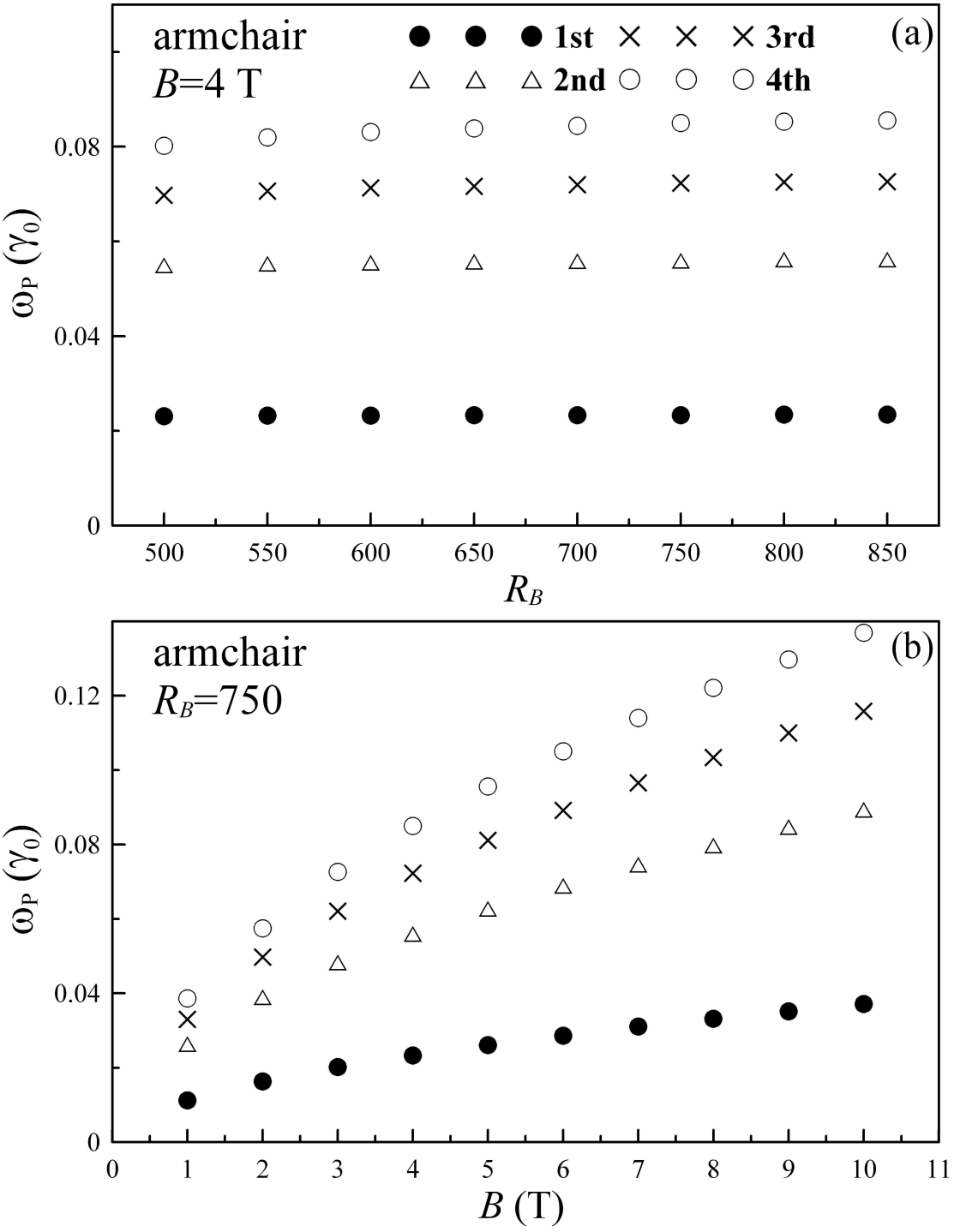

Figure 3.7. The optical absorption frequencies from original band-edge states for a spatially modulated magnetic field along the armchair direction. Their dependences on (a) the period and (b) the field strength.

gradient approximation. The low-energy bands are drastically changed by the modulated magnetic field. They display the partial flat bands at $E_F = 0$ and parabolic bands at others. Each parabolic band owns one original band-edge state and four extra band-edge states. Such electronic states could induce the asymmetric prominent peaks in the optical absorption spectra. The parabolic bands close to k_y^{pp} and k_y^{sp}'s are, respectively, doubly degenerate and nondegenerate. The former could be regarded as the quasi-Landau levels based on the characteristics of wave functions. The latter are divided into two different kinds of subbands, i.e., the α and β subbands. Their wave functions display different features from those of QLLs. The wave functions associated with the carbon atoms a (b) of the first QLL have one tight-binding function $A_{o,e}^{c,v}(x_1)$ ($B_{o,e}^{c,v}(x_2)$) centered at x_1 (x_2). The other QLLs exhibit two tight-binding functions $A_{o,e}^{c,v}(x_1)$ ($B_{o,e}^{c,v}(x_1)$) and $A_{o,e}^{c,v}(x_2)$ ($B_{o,e}^{c,v}(x_2)$) situated at x_1 and x_2. The two positions $x_1 = 1/4$ and $x_2 = 3/4$ correspond to the maximum field strength. The wave functions of QLLs present the similar characteristics to those of LLs which result from a uniform magnetic field, e.g., the same oscillatory behavior, effective quantum number, and distribution width. However, the wave functions at k_y^{sp}'s display different features. The α and β subbands own the different spatial symmetries, and their two tight-binding functions exhibit overlap behavior. The different spatial symmetries and overlap behavior would induce the anisotropic features and extra excitations in the optical absorption spectra.

The optical absorption spectra reveal a plenty of prominent asymmetric peaks. These peaks could be further divided into the principal peaks ω_P's and subpeaks ω_S's, which mainly come from the excitations of the original band-edge and extra band-edge states, respectively. The optical absorption spectra are strongly affected by the periodic magnetic

field and the polarization direction of an EM wave. The peak height of principal peaks grows as the field strength and period increase. The energy of each ω_P rises with the increase of B, and it would be weakly dependent on the period as R_B becomes large enough. As to the subpeaks, ω_S's could be classified into two subgroups, ω_S^a's and ω_S^b's, because of the two kinds of subbands α and β. They originate in the excitations of α (β) to β (α) and α (β) to α (β), respectively. Both of them strongly rely on the field strength and period. Furthermore, the optical absorption spectra could reveal the anisotropic behavior in the modulated and polarization directions. The principal peaks of the armchair and zigzag directions exhibit somewhat different frequencies, and the peak height of the former is higher than that of the latter. However, they display weak dependence on the polarization direction. Concerning the subpeaks, their peak heights and frequencies present strong dependence on both the modulated and polarization directions. Such anisotropy of the optical absorption spectra could reflect the anisotropic behavior of energy bands along the two different modulated directions and the different spatial symmetries of wave functions at the extra band-edge states. ω_P's and ω_s's obey the different selection rules. The former is simply represented by $|\Delta n| = 1$, and this result is the same with that of the LLs originating in a uniform perpendicular magnetic field. The most important reason is that the main features of wave functions at k_y^{pp} resemble those of $\mathbf{B}_0$. Nevertheless, the low-energy absorption spectra of QLLs and LLs still have some different characteristics. The former show the asymmetric square-root peaks, and the latter own the delta-function-like peaks. The peak frequency of QLLs is weakly dependent on the modulated period. The peak intensity of LLs is stronger than that of QLLs. Moreover, the low-frequency optical absorption spectra of QLLs could exhibit the anisotropic features in the different modulated directions. As to the subpeaks,

ω_s's display a different selection rule from that of principal peaks, i.e., $|\Delta n| = 1$ and $|\Delta n| = 0$. Such an important difference mainly comes from the overlap behavior of the wave functions at k_y^{sp}'s. The overlap behavior induces the excitations with $|\Delta n| = 0$, which is forbidden in the principal peaks. Besides, the subpeaks present the anisotropy in both modulated direction and electric polarization direction. The selection rule and anisotropic features of optical absorption spectra originating in a modulated magnetic field are very different from those in a uniform perpendicular magnetic field or in the absence of an external field. Such important differences could be verified by the optical measurements.

References

[1] K. S. Novoselov, A. K. Geim, S. V. Morozov, D. Jiang, Y. Zhang, S. V. Dubonos, I. V. Grigorieva and A. A. Firsov 2004 *Science* **306** 666

[2] K. S. Novoselov, A. K. Geim, S. V. Morozov, D. Jiang, M. I. Katsnelson, I. V. Grigorieva, S. V. Dubonos, and A. A. Firsov 2005 *Nature* **438** 197

[3] C. Berger, Z. M. Song, T. B. Li, X. B. Li, A. Y. Ogbazghi, R. Feng, Z. T. Dai, A. N. Marchenkov, E. H. Conrad, P. N. First, and W. A. de Heer 2004 *J. Phys. Chem.* B **108** 19912

[4] C. Berger, Z. Song, X. Li, X. Wu, N. Brown, C. Naud, D. Mayou, T. Li, J. Hass, A. N. Marchenkov, E. H. Conrad, P. N. First, and W. A. de Heer 2006 *Science* **312** 1191

[5] C. P. Chang, C. L. Lu, F. L. Shyu, R. B. Chen, Y. K. Fang and M. F. Lin 2004 *Carbon* **42** 2975

[6] S. Latil and L. Henrard 2006 *Phys. Rev. Lett.* **97** 036803

[7] Y. Zheng and T. Ando 2002 *Phys. Rev.* B **65** 245420

[8] E. McCann 2006 *Phys. Rev.* B **74** 161403

[9] C. L. Lu, C. P. Chang, Y. C. Huang, J. M. Lu, C. C. Hwang, and M. F. Lin 2006 *Journal of Physics: Condensed Matter* **18** 5849

[10] F. Guinea, A. H. C. Neto, and N. M. R. Peres 2006 Phys. Rev. B **73** 245426

[11] E. McCann, K. Kechedzhi, V. I. Falko, H. Suzuura, T. Ando, and B. L. Altshuler 2006 *Phys. Rev. Lett.* **97** 146805

[12] B. Partoens and F. M. Peeters 2006 *Phys. Rev.* B **74** 075404

[13] M. Koshino and T. Ando 2007 *Phys. Rev.* B **76** 085425

[14] C. L. Lu, C. P. Chang, J. H. Ho, C. C. Tsai, and M. F. Lin 2006 *Physica* E **32** 585

[15] J. H. Ho, Y. H. Lai, S. J. Tsai, J. S. Hwang, C. P. Chang, and M. F. Lin 2006 *J. Phys. Soc. Jpn.* **75** 114703

[16] E. McCann and V. I. Fal'ko 2006 *Phys. Rev. Lett.* **96** 086805

[17] J. M. Pereira, F. M. Peeters, and P. Vasilopoulos 2007 *Phys. Rev. B* **76** 115419

[18] N. Nemec and G. Cuniberti 2007 *Phys. Rev.* B **75** 201404

[19] J. H. Ho, Y. H. Lai, Y. H. Chiu, and M. F. Lin 2008 *Nanotechnology* **19** 035712

[20] Y. H. Chiu, Y. H. Lai, J. H. Ho, D. S. Chuu, and M. F. Lin 2008 *Phys. Rev.* B **77** 045407

[21] E. V. Castro, K. S. Novoselov, S. V. Morozov, N. M. R. Peres, J. M. B. Lopes dos Santos, J. Nilsson, F. Guinea, A. K. Geim, and A. H. Castro Neto 2007 *Phys. Rev. Lett.* **99** 216802

[22] Y. H. Lai, J. H. Ho, C. P. Chang, and M. F. Lin 2008 *Phys. Rev.* B **77** 085426

[23] M. L. Sadowski, G. Martinex, and M. Potemski, C. Berger, and W. A. de Heer 2006 *Phys. Rev. Lett.* **97** 266405

[24] D. S. L. Abergel and Vladimir I. Fal'ko 2007 *Phys. Rev.* B **75** 155430

[25] R. S. Deacon, K.-C. Chuang, R. J. Nicholas, K. S. Novoselov, and A. K. Geim 2007 *Phys. Rev.* B **76** 081406

[26] D. S. L. Abergel, A. Russell, and Vladimir I. Fal'ko 2007 *Appl. Phys. Lett.* **91** 063125

[27] C. L. Lu, C. P. Chang, Y. C. Huang, R. B. Chen, and M. F. Lin 2006 *Phys. Rev.* B **73** 144427

[28] C. L. Lu, H. L. Lin, C. C. Hwang, J. Wang, C. P. Chang, and M. F. Lin 2006 *Appl. Phys. Lett.* **89** 221910

[29] Z. Jiang, E. A. Henriksen, L. C. Tung, Y.-J. Wang, M. E. Schwartz, M. Y. Han, P. Kim, and H. L. Stormer 2007 *Phys. Rev. Lett.* **98** 197403

[30] F. L. Shyu and M. F. Lin 2000 *J. Phys. Soc. Jpn.* **69** 607

[31] J. H. Ho, C. P. Chang and M. F. Lin 2006 *Phys. Lett. A* **352** 446

[32] J. H. Ho, C. L. Lu, C. C. Hwang, C. P. Chang and M. F. Lin 2006 *Phys. Rev. B* **74** 085406

[33] X. F. Wang and T. Chakraborty 2007 *Phys. Rev. B* **75** 041404

[34] A. H. Castro Neto and F. Guinea 2007 *Phys. Rev.* B **75** 045404

[35] Y. Zhang, Y. W. Tan, H. L. Stormer, and P. Kim 2005 *Nature* **438** 201

[36] K. S. Novoselov, Z. Jiang, Y. Zhang, S. V. Morozov, H. L. Stormer, U. Zeitler, J. C. Maan, G. S. Boebinger, P. Kim, and A. K. Geim 2007 *Science* **315** 1379

[37] K. S. Novoselov, E. McCann, S. V. Morozov, V. I. Fal'ko, M. I. Katsnelson, U. Zeitler, D. Jiang, F. Schedin, and A. K. Geim 2006 *Nat. Phys.* **2** 177

[38] V. P. Gusynin and S. G. Sharapov 2006 *Phys. Rev.* B **73** 245411

[39] V. P. Gusynin, V. A. Miransky, S. G. Sharapov, and I. A. Shovkovy 2006 *Phys. Rev.* B **74** 195429

[40] M. Koshino and T. Ando 2006 *Phys. Rev.* B **73** 245403

[41] J. Nilsson, A. H. Castro Neto, F. Guinea, and N. M. R. Peres 2006 *Phys. Rev. Lett.* **97** 266801

[42] N. M. R. Peres, F. Guinea, and A. H. Castro Neto 2006 *Phys. Rev.* B **73** 125411

[43] S. Y. Zhou, G.-H. Gweon, J. Graf, A. V. Fedorov, C. D. Spataru, R. D. Diehl, Y. Kopelevich, D.-H. Lee, Steven G. Louie, and A. Lanzara 2006 *Nature Physics* **2** 595

[44] P. R. Wallace 1947 *Phys. Rev.* **71** 622

[45] M. F. Lin and Kenneth W.-K. Shung 1994 *Phys. Rev.* B **50** 17744

[46] Y. C. Huang, M. F. Lin, and C. P. Chang 2008 *J. App. Phy.* **103** 073709

[47] J. Blinowski, N. H. Hau, C. Rigaux, J. P. Vieren, R. L. Toullee, G. Furdin, A. Herold, and J. Melin 1980 *J. Phys.* (Paris) **41** 47

Chapter 4

Electronic properties and optical absorption spectra of a graphene monolayer in the modulated electric field

4.1 Introduction

The bulk graphite is one of the most extensively studied materials in both theoretical [1-4] and experimental [5-9] fields. Recently, the few-layer graphenes have been successfully produced [10-13]. Such systems are very appropriate in studying the two-dimensional physical properties. They have given rise to amounts of investigations, e.g., band structure [14-31], electronic excitations [32-35], transport properties [36-43], and optical spectra [14, 44-50]. A graphene monolayer is an exotic zero-gap semiconductor with a vanishing density of states at the Fermi level $E_F = 0$, which mainly originates in the hexagonal honeycomb structure [1]. The low-energy optical absorption spectrum of a single-layer graphene in the absence of an external field does not exhibit any absorption peaks. The low-frequency electronic structures and optical absorption spectra could be drastically changed by applying a modulated magnetic field [28,29]. Such a field could alter energy dispersions, create extra band-edge states, induce composite behavior in state degeneracy, destroy the symmetry of energy bands about the original band-edge state, and cause anisotropy at low energy [29]. The optical absorption spectra could reveal two kinds of selection rule at the original band-edge and extra band-edge states, which is primarily owing to the characteristics of their wave functions [29]. In addition, the optical absorption spectra might display the anisotropic behavior in the modulation direction and electric polarization.

In this work, the π-electronic structure and optical absorption spectra of a graphene monolayer in a spatially modulated electric field are studied by the tight-binding model and gradient approximation [14, 51-53]. The dependence of the low-energy electronic properties on the period, field strength, and modulation direction would be investigated in detail, such as energy dispersions, state degeneracy, band-edge states, and density of states. The relation between the optical absorption spectra and the modulated electric field is also studied.

This paper is composed of five sections. The band-like Hamiltonian matrix in a modulated electric potential is obtained in Sec. II. The main features of the electronic properties and of the optical absorption spectra are, respectively, discussed in Secs. III. and IV. Finally, Sec. V involves concluding remarks.

4.2 Hamiltonian matrix

The π-electronic structure of $2p_z$ orbitals is calculated by the tight-binding model with nearest-neighbor interactions. In the absence of an external field, there are two carbon atoms, a and b, in a primitive unit cell of a single-layer graphene. The π-electronic Bloch function consisting of the two linear tight-binding functions is expressed as $|\Psi_{\mathbf{k}}\rangle = C_{a\mathbf{k}}|a_{\mathbf{k}}\rangle + C_{b\mathbf{k}}|b_{\mathbf{k}}\rangle$, where $|a_{\mathbf{k}}\rangle = \sum_i e^{i\mathbf{k}\cdot\mathbf{R}_m}|a_{m\mathbf{k}}\rangle$ and $|b_{\mathbf{k}}\rangle = \sum_j e^{i\mathbf{k}\cdot\mathbf{R}_n}|b_{n\mathbf{k}}\rangle$. The Hamiltonian built from $|a_{\mathbf{k}}\rangle$ and $|b_{\mathbf{k}}\rangle$ is a 2×2 Hermitian matrix. The site energies of a and b atoms are the same and assumed to be zero, i.e., $\langle a_{m\mathbf{k}}|H_0|a_{m\mathbf{k}}\rangle = \langle b_{n\mathbf{k}}|H_0|b_{n\mathbf{k}}\rangle = 0$. The nonvanishing Hamiltonian matrix element is given by

$$\langle b_{n\mathbf{k}}|H_0|a_{m\mathbf{k}}\rangle = \gamma_0 \exp[\, i\mathbf{k}\cdot(\mathbf{R}_m - \mathbf{R}_n)\,] \equiv \sum_{i=1,2,3} t_{i\mathbf{k}}, \tag{4.1}$$

where γ_0(=2.56 eV) [1] is the atom-atom interaction between two nearest-neighbor atoms

at $\mathbf{R}_m$ and $\mathbf{R}_n$. The three hopping integrals are, respectively, $t_{1\mathbf{k}} = \gamma_0 \exp[(ik_x b'/2 + ik_y\sqrt{3}b'/2)]$, $t_{2\mathbf{k}} = \gamma_0 \exp[(ik_x b'/2 - ik_y\sqrt{3}b'/2)]$, and $t_{3\mathbf{k}} = \gamma_0 \exp(-ik_x b')$, where $b' = 1.42$ $\mathring{A}$ is the C-C bond length.

A single-layer graphene is assumed to exist in a modulated electric potential $V(x) = V_0 \cos(2\pi x/l_E)$ along the armchair direction, as shown in Fig. 4.1(a). V_0 is the strength of a modulated electric potential. The Hamiltonian is $H = H_0 + U$, where H_0 is the Hamiltonian without the external field. $l_E = 3b'R_E$ is the periodic length, where parameter R_E is useful in describing the dimensionality of the Hamiltonian matrix. An enlarged rectangular unit cell includes $4R_E$ carbon atoms ($2R_E$ a atoms and $2R_E$ b atoms). The wave function composed of the $4R_E$ Bloch functions is presented as

$$|\Psi_{\mathbf{k}}^{c,v}\rangle = \sum_{n=1}^{2R_E} C_{a\mathbf{k}}^n |a_{n\mathbf{k}}\rangle + C_{b\mathbf{k}}^n |b_{n\mathbf{k}}\rangle. \tag{4.2}$$

When the period is large enough, the effects of the electric potential on the three nearest-neighboring hopping integrals are negligible. The site energies would be changed into

$$\langle a_{n\mathbf{k}}|H|a_{n\mathbf{k}}\rangle = V_0 \cos[(n-1)\pi/R_E] \equiv V_n; \tag{4.3a}$$

$$\langle b_{n\mathbf{k}}|H|b_{n\mathbf{k}}\rangle = V_0 \cos[(n-2/3)\pi/R_E] \equiv V_{n+1/3}. \tag{4.3b}$$

For convenience, the base functions are chosen as the following sequence $\{|a_{1\mathbf{k}}\rangle, |b_{2R_E\mathbf{k}}\rangle, |b_{1\mathbf{k}}\rangle, |a_{2R_E\mathbf{k}}\rangle, |a_{2\mathbf{k}}\rangle, |b_{2R_E-1\mathbf{k}}\rangle, |b_{2\mathbf{k}}\rangle, |a_{2R_E-1\mathbf{k}}\rangle, \ldots |a_{R_E-1\mathbf{k}}\rangle, |b_{R_E+2\mathbf{k}}\rangle, |b_{R_E-1\mathbf{k}}\rangle, |a_{R_E+2\mathbf{k}}\rangle, |a_{R_E\mathbf{k}}\rangle, |b_{R_E+1\mathbf{k}}\rangle, |b_{R_E\mathbf{k}}\rangle; |a_{R_E+1\mathbf{k}}\rangle\}$. The Hamiltonian matrix becomes

a band-like Hermitian matrix

$$\begin{pmatrix} V_1 & q^* & p^* & 0 & \dots & \dots & 0 & 0 \\ q & V_{2R_E+1/3} & 0 & p & 0 & \dots & \dots & 0 \\ p & 0 & V_{4/3} & 0 & q & 0 & \dots & 0 \\ 0 & p^* & 0 & \ddots & 0 & q^* & 0 & 0 \\ \vdots & \ddots & q^* & 0 & \ddots & \ddots & \ddots & 0 \\ \vdots & \dots & \ddots & q & \ddots & \ddots & 0 & p \\ 0 & \vdots & \vdots & \ddots & \ddots & 0 & V_{R_E+1/3} & q \\ 0 & 0 & 0 & 0 & 0 & p^* & q^* & V_{R_E+1} \end{pmatrix}, \tag{4.4}$$

where $p \equiv t_{1\mathbf{k}} + t_{2\mathbf{k}}$ and $q \equiv t_{3\mathbf{k}}$.

The π-electronic structure is strongly affected by the direction of a modulated electric potential, which mainly results from the anisotropic structure of a 2D monolayer graphene. For the zigzag direction (Fig. 4.1(b)), the similar equations could be also derived. The three hopping integrals are $t'_{1\mathbf{k}} = \gamma_0 \exp(ik_x\sqrt{3}b'/2 + ik_y b'/2)$, $t'_{2\mathbf{k}} = \gamma_0 \exp(-ik_x\sqrt{3}b'/2 + ik_y b'/2)$, and $t'_{3\mathbf{k}} = \gamma_0 \exp(-ik_y b')$, respectively. The Hamiltonian matrix elements are further given by

$$\langle b_{m\mathbf{k}}|H|a_{n\mathbf{k}}\rangle = t'_{1\mathbf{k}}\delta_{m,n+1} + t'_{2\mathbf{k}}\delta_{m,n-1} + t'_{3\mathbf{k}}\delta_{m,n}, \tag{4.5a}$$

$$\langle a_{n\mathbf{k}}|H|a_{n\mathbf{k}}\rangle = \langle b_{n\mathbf{k}}|H|b_{n\mathbf{k}}\rangle = V_0 \cos[(n-1)\pi/R_E] \equiv V_n. \tag{4.5b}$$

With the base functions $\{|a_{1\mathbf{k}}\rangle, |b_{2R_E\mathbf{k}}\rangle, |b_{1\mathbf{k}}\rangle, |a_{2R_E\mathbf{k}}\rangle, |b_{2\mathbf{k}}\rangle, |a_{2R_E-1\mathbf{k}}\rangle, |a_{2\mathbf{k}}\rangle, |b_{2R_E-1\mathbf{k}}\rangle, \dots |b_{R_E-1\mathbf{k}}\rangle, |a_{R_E+2\mathbf{k}}\rangle, |a_{R_E-1\mathbf{k}}\rangle, |b_{R_E+2\mathbf{k}}\rangle, |a_{R_E\mathbf{k}}\rangle, |b_{R_E+1\mathbf{k}}\rangle, |b_{R_E\mathbf{k}}\rangle; |a_{R_E+1\mathbf{k}}\rangle\}$, the $4R_E \times 4R_E$

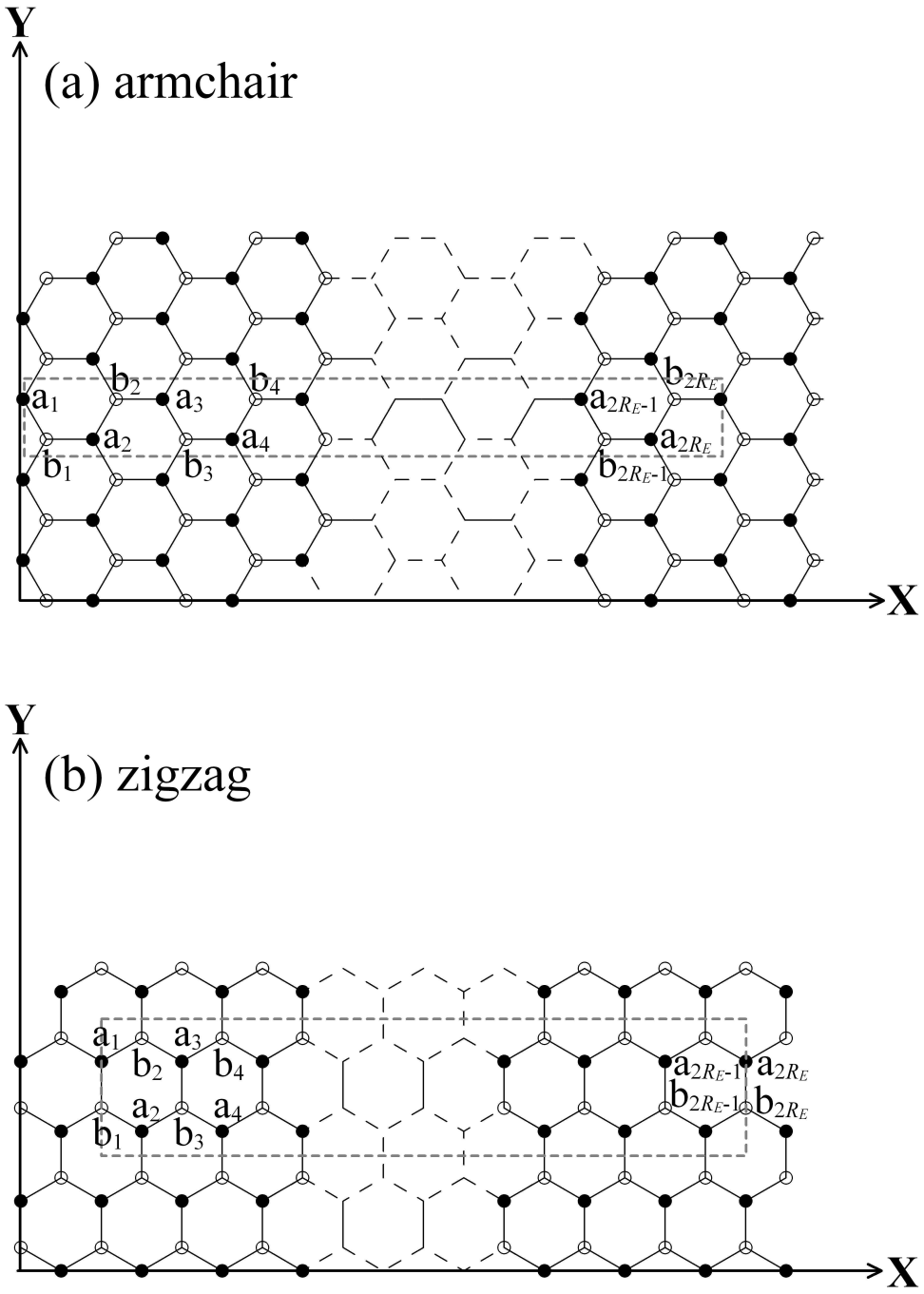

Figure 4.1. The primitive unit cells of a monolayer graphene in a modulated electric field along the (a) armchair direction and (b) zigzag direction.

band-like Hamiltonian matrix for the zigzag direction is

$$\begin{pmatrix}
V_1 & t'^{*}_{2\mathbf{k}} & t'^{*}_{3\mathbf{k}} & 0 & t'^{*}_{1\mathbf{k}} & 0 & \dots & 0 & 0 & 0 \\
t'_{2\mathbf{k}} & V_{2R_E} & 0 & t'_{3\mathbf{k}} & 0 & t'_{1\mathbf{k}} & 0 & 0 & 0 & 0 \\
t'_{3\mathbf{k}} & 0 & V_1 & t'_{1\mathbf{k}} & \ddots & \ddots & \ddots & \ddots & 0 & 0 \\
0 & t'^{*}_{3\mathbf{k}} & t'^{*}_{1\mathbf{k}} & V_{2R_E} & \ddots & & & \ddots & 0 & \vdots \\
t'_{1\mathbf{k}} & 0 & \ddots & \ddots & \ddots & & & \ddots & t'^{*}_{1\mathbf{k}} & 0 \\
0 & t'^{*}_{1\mathbf{k}} & \ddots & & & \ddots & \ddots & \ddots & 0 & t'_{1\mathbf{k}} \\
\vdots & 0 & \ddots & & & \ddots & V_{R_E} & t'^{*}_{1\mathbf{k}} & t'^{*}_{3\mathbf{k}} & 0 \\
0 & 0 & \ddots & \ddots & \ddots & \ddots & t'_{1\mathbf{k}} & V_{R_E+1} & 0 & t'_{3\mathbf{k}} \\
0 & 0 & 0 & 0 & t'_{1\mathbf{k}} & 0 & t'_{3\mathbf{k}} & 0 & V_{R_E} & t'_{2\mathbf{k}} \\
0 & 0 & 0 & \dots & 0 & t'^{*}_{1\mathbf{k}} & 0 & t'^{*}_{3\mathbf{k}} & t'^{*}_{2\mathbf{k}} & V_{R_E+1}
\end{pmatrix}. \tag{4.6}$$

4.3 π-electronic properties

By diagonalizing the band-like Hamiltonian matrix, the energy bands are obtained. Since the unoccupied conduction bands (E^c's) and occupied valence bands (E^v's) are symmetric about the Fermi level ($E_F = 0$), only the former are discussed. Because the range of the first Brillouin zone along the modulated direction ($k_x \leq \pi/(3b'R_E)$) is much shorter than the other one ($k_y \leq \pi/\sqrt{3}b'$), the energy dispersions along the modulated direction are not shown here, and thus only the k_y-dependent energy bands are discussed.

The low-energy bands without an external field are shown by the small solid circles in Fig. (4.2) at $R_E = 500$ (≈ 200 nm). There are two nondegenerate linear bands intersecting at $E_F = 0$ and many parabolic bands with double degeneracy at other energies. Each energy band owns two original band-edge states $k_y^{pp} = 2\pi/3\sqrt{3}b'$ and $k_x^{pp} = 0$. It should be

noticed that the two band-edge states are the Fermi-momentum states (k_F's) of the linear conduction and valence bands. Although the range of the wave vector along the modulated direction is narrow, the k_x-dependence of energy bands is still considerable. That is to say, the energy bands of a monolayer graphene at $V_0 = 0$ exhibit two-dimensional dispersions. There are only four Fermi-momentum states at $E_F = 0$ (including two spin states).

The modulated electric field leads to drastic changes in the energy dispersions, state degeneracy, band-edge states, and dimensionality. The energy bands of $V_0 = 0.1\gamma_0$ at $R_E = 500$ are shown by the large solid circles in Fig. (4.2). They display oscillatory energy dispersions near k_y^{pp}. The doubly degenerate parabolic bands become singly degenerate. Each energy band might have several band-edge states, and most of them are not located at k_y^{pp}. Such band-edge states could induce the prominent peaks in the density of states (DOS) and optical absorption spectra. For convenience, these band-edge states are further divided into two categories, μ and ν states, as indicated in Fig. (4.2). The two μ (ν) states at the left- and right-hand sites of k_y^{pp} might have different energies; that is, one side of the parabolic bands might be asymmetric to the other about the original band-edge state. Concerning the states near the Fermi-level, the different Fermi-momentum states exist at $E_F = 0$. The energy dispersions near k_F's are linear for the k_y-dependence, while they are completely flat for the k_x-dependence (not shown). The dispersionless feature means that the number of k_F's is finite. The k_x-dependence could be neglected in the lower parabolic bands. As a result, the low-frequency energy bands, with $E^c \leq V_0$, are regarded as one-dimensional bands.

The strength, period, and direction of a modulated electric field strongly affect the electronic structure. The modulation effects are diminished by decreasing the field strength,

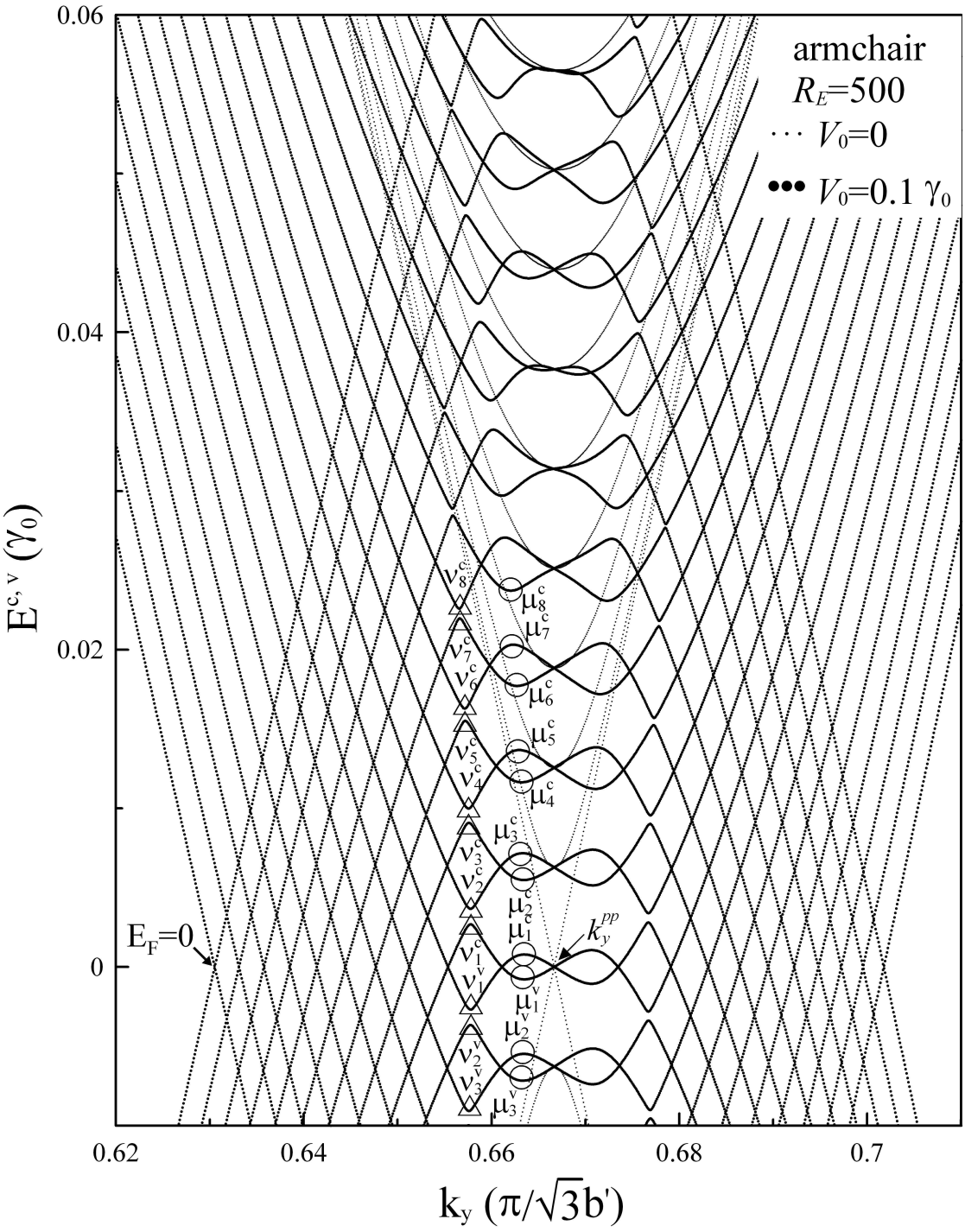

Figure 4.2. The low-energy bands for $R_E = 500$ along the armchair direction at $V_0 = 0$ and $V_0 = 0.1\ \gamma_0$.

as shown in Fig. 4.3(a) at $R_E = 500$ $V_0 = 0.05$ γ_0. The range of k_y and the number of oscillatory bands are reduced. As the period lessens, the energy spacing between two band-edge states is enlarged, as shown in Fig. 4.3(b) at $R_E = 250$ $V_0 = 0.1$ γ_0. However, the range of k_y is weakly dependent on R_E. As to the zigzag direction, the energy bands display the similar features to those of the armchair direction (Fig. 4.3(c)). It is noticeable that the band-edge states of two modulated directions might have different energies, i.e., the modulated electric field could induce the anisotropic properties in the electronic structure.

Density of states (DOS) is closely related to the essential features of the electronic structure. It is defined as

$$D(\omega) = \sum_{\sigma,\, h=c,v} \int_{1stBZ} \frac{dk_x dk_y}{(2\pi)^2} \frac{\Gamma}{\pi} \frac{1}{[\omega - E^h(k_x, k_y)]^2 + \Gamma^2}\,, \tag{4.7}$$

where Γ ($= 5 \times 10^{-4}$ γ_0) is a phenomenological broadening parameter. The low-frequency DOS without fields is proportional to ω, as shown by the crosses in Fig. 4.4(a). It has no special structures. The vanishing DOS at $\omega = 0$ indicates that a monolayer graphene is a zero-gap semiconductor. On the other hand, the modulated electric field leads to many asymmetric peaks and a finite DOS at $\omega = 0$ (Figs. 4.4(a) and 4.4(b)). The peak structures primarily come from the band-edge states of parabolic bands (Figs. 4.2(b)). Such peaks could be further classified into the prominent square-root divergent and inconspicuous peaks. They, respectively, mainly originate in the μ and ν states, as shown in Fig. 4.4(a). Furthermore, there are some pairs of prominent peaks (indicated by the arrows in Fig. 4.4(a)), and each pair is associated with the asymmetry of the 1D parabolic bands about k_y^{pp} (discussed earlier in Fig. (4.2)). The frequency, number, and height of peaks are sensitive to the changes in the field strength and period. The value of DOS at $\omega = 0$ grows as the field strength increases, and it is weakly dependent on the period. The peak

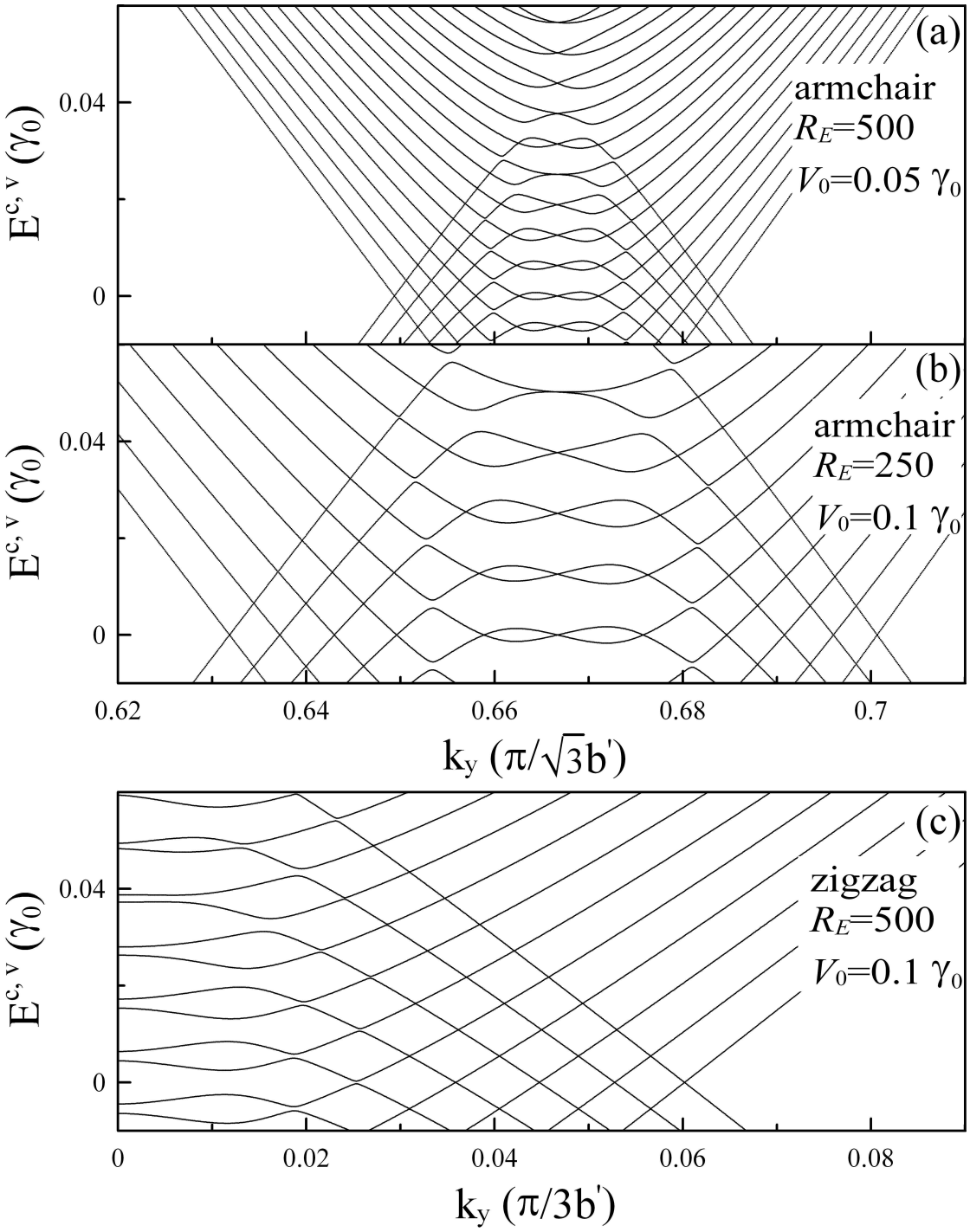

Figure 4.3. The low-energy bands along the armchair direction at (a) $R_E = 500$, $V_0 = 0.05$ γ_0, (b) $R_E = 250$, $V_0 = 0.1$ γ_0, and (c) those along the zigzag direction at $R_E = 500$, $V_0 = 0.1$ γ_0.

heights are, respectively, enhanced and reduced by increasing V_0 and R_E. The peak number increases as the period increases, and it is weakly related to the field strength. The 1D linear bands have finite Fermi-momentum states, so the monolayer graphene in the presence of a modulated electric field is a semimetal. The free carriers in a semimetallic graphene are deduced to cause the low-frequency plasmon [54]. The experimental measurements on the energy loss spectra could be utilized to examine the predicted electronic properties.

The frequencies of asymmetric peaks in DOS deserve a closer investigation. The frequency of the peak resulting from the μ (ν) state is denoted as ω_μ (ω_ν). The relation between the first four ω_μ's (ω_ν's) and the field strength at $R_E = 500$ is shown in Fig. 4.5(a) (Fig. 4.5(b)). ω_μ's and ω_ν's correspond to the band-edge states at the left-hand neighborhood of k_y^{pp} (Fig. (4.2)). Both ω_μ's and ω_ν's are weakly related to the field strength. Figs. 4.5(c) and 4.5(d), respectively, show the dependence of ω_μ's and ω_ν's on the period at $V_0 = 0.1\ \gamma_0$. The former presents somewhat oscillatory behavior, and the latter declines as R_E increases. Such dependence might be reflected by the optical absorption spectra.

4.4 Optical absorption spectra

The optical excitations can directly present the main features of electronic properties. Based on the Fermi's golden rule, the optical absorption function is given by

$$A(\omega) \propto \sum_{c,v,\widetilde{n},\widetilde{n}'} \int_{1stBZ} \frac{d\mathbf{k}}{(2\pi)^2} \left| \left\langle \Psi^c\left(\mathbf{k},\widetilde{n}\right) \left| \frac{\widehat{\mathbf{E}}\cdot\mathbf{P}}{m_e} \right| \Psi^v\left(\mathbf{k},\widetilde{n}'\right) \right\rangle \right|^2 \times Im\left[\frac{f\left(E^c\left(\mathbf{k},\widetilde{n}\right)\right) - f\left(E^v\left(\mathbf{k},\widetilde{n}'\right)\right)}{E^c\left(\mathbf{k},\widetilde{n}\right) - E^v\left(\mathbf{k},\widetilde{n}'\right) - \omega - i\Gamma} \right], \tag{4.8}$$

where $f\left(E\left(\mathbf{k},\widetilde{n}\right)\right)$ is the Fermi-Dirac distribution function, and $\widehat{\mathbf{E}}$ is the unit vector of an

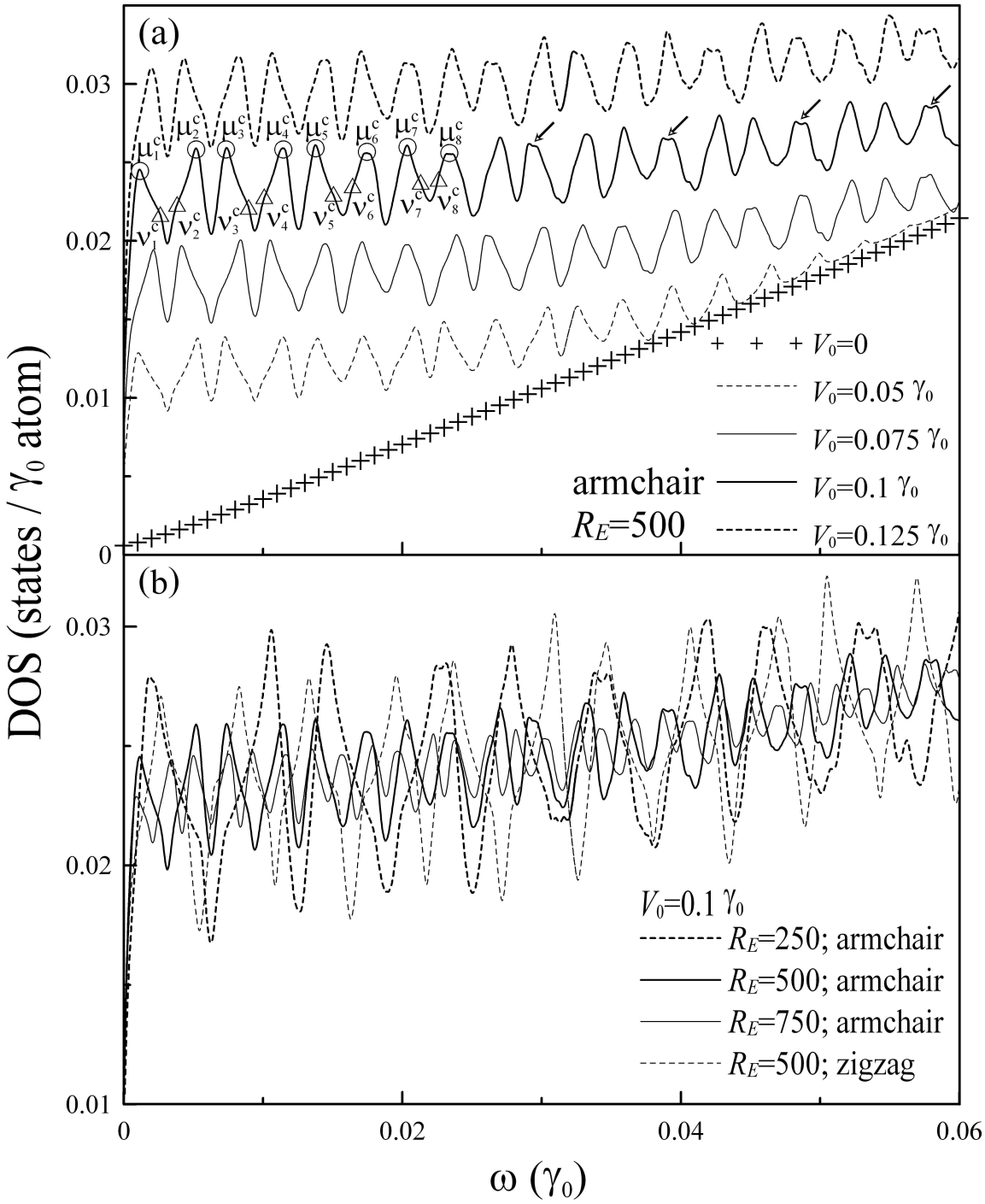

Figure 4.4. (a) The low-frequency density of states for $R_E = 500$ at different field strengths, and (b) for $V_0 = 0.1\ \gamma_0$ at different periods. DOS along the zigzag direction for $R_E = 500$ at $V_0 = 0.1\ \gamma_0$ is also shown in (b).

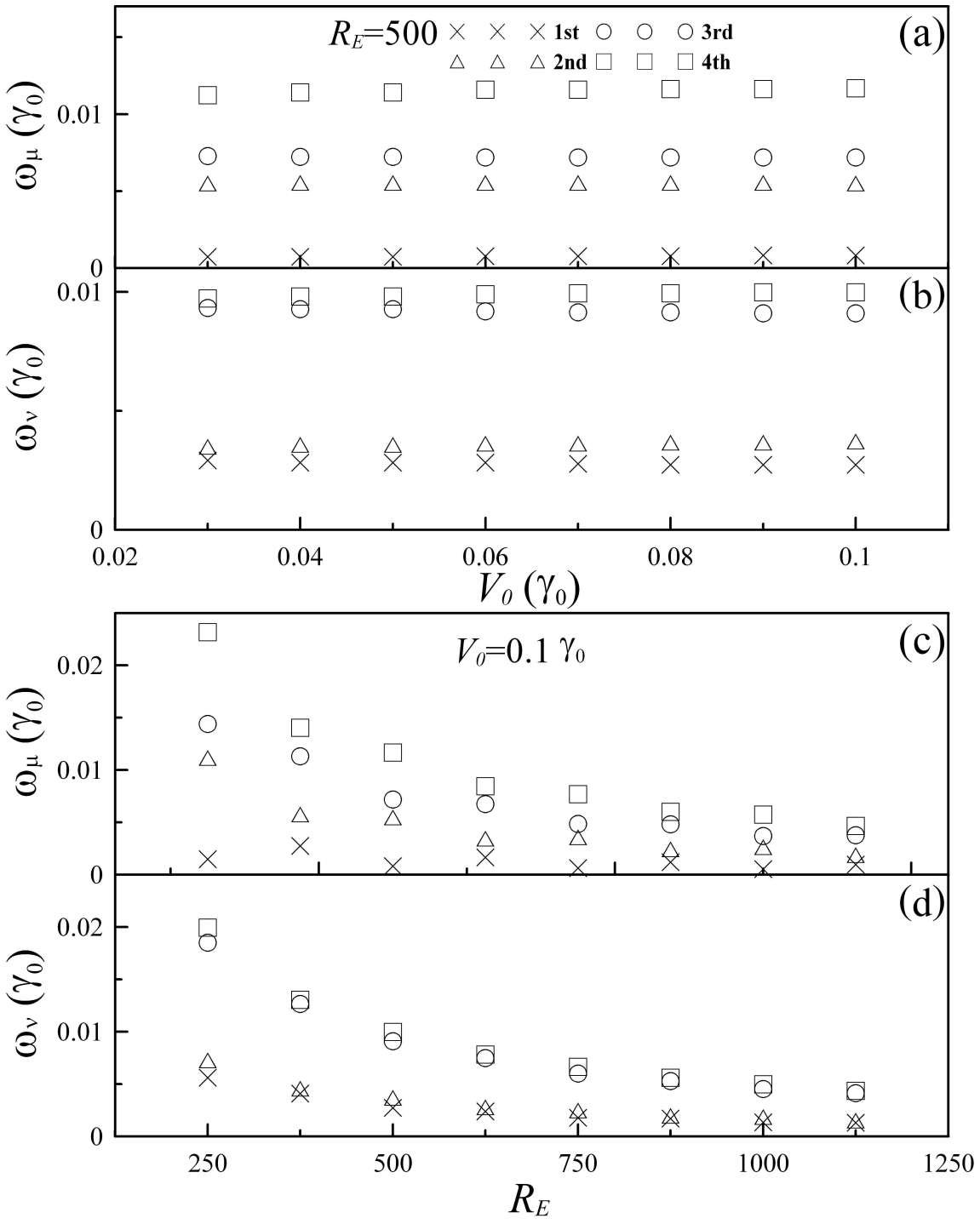

Figure 4.5. Energies of the first four μ and four ν band-edge states at the left-hand neighborhood of k_y^{pp}. (a) and (b) are their dependence on the field strength; (c) and (d) are the dependence on the period.

electric polarization. With an electric polarization $\widehat{\mathbf{E}} \perp \widehat{x}$, the electromagnetic field excites electrons from the occupied valence to unoccupied conduction bands (the inter-π-band excitations) at zero temperature. The optical selection rule due to the vertical transitions is $\Delta \mathbf{k}_y = \mathbf{0}$, which is mainly determined by the zero momentum of photon. The velocity matrix element $M^{cv} = \left\langle \Psi^c(\mathbf{k}, \widetilde{n}) \left| \widehat{\mathbf{E}} \cdot \mathbf{P}/m_e \right| \Psi^v(\mathbf{k}, \widetilde{n}') \right\rangle$ is evaluated within the gradient approximation [14, 51-53]. It is approximated by taking the gradient of the Hamiltonian matrix element versus the wave vector k_y.

The joint density of states (D_J) can reflect all the possible inter-π-band excitation channels. D_J is obtained by setting the velocity matrix element in Eq. (4.8) to one, and strongly affected by the modulated electric field. Fig. 4.6(a) shows the low-energy D_J's for $R_E = 500$ at different field strengths along the armchair direction. In the $V_0 = 0$ case, D_J has no special structures (by the crosses in Fig. 4.6(a)). It grows linearly with the increasing frequency and vanishes at $\omega = 0$. As the field strength increases, D_J exhibits many prominent peaks. Such peaks mainly result from the transition channels between two μ (ν) states, and they are enhanced by increasing the field strength. Some excitations from these states have nearly the same energy, and thus their peaks would be undistinguishable. It is worth noticing that most of the conspicuous peaks with stronger intensity primarily originate in the channels from μ_n^v to μ_{n+1}^c (μ_{n+1}^v to μ_n^c) and from ν_n^v to ν_{n+1}^c (ν_{n+1}^v to ν_n^c), as indicated in Fig. 4.6(a). The peak heights of such channels are relatively higher than those of other channels. Because the occupied valence and unoccupied conduction bands are symmetric about the Fermi level, the excitations from μ_n^v to μ_{n+1}^c (ν_n^v to ν_{n+1}^c) and from μ_{n+1}^v to μ_n^c (ν_{n+1}^v to ν_n^c) own the same frequency. Besides, the excitation between μ_n^v and μ_{n+1}^c has nearly the same energy as that between ν_n^v and ν_{n+1}^c. Based on the above-

mentioned reasons, the peaks resulting from the excitations of μ_n^v to μ_{n+1}^c, μ_{n+1}^v to μ_n^c, ν_n^v to ν_{n+1}^c, and ν_{n+1}^v to ν_n^c, might be undistinguishable. In addition to the period, D_J's also strongly depend on the modulated period and direction, as shown in Fig. 4.6(b). The peak height rises with the increase of the period. The peak number is approximately an inverse proportion to the period. As to the zigzag direction, D_J also shows rich peaks, while their height and frequency are different from those of the armchair direction.

The optical absorption spectra might be very different from the joint density of states after including the velocity matrix element. For $R_E = 500$, $A(\omega)$'s of different field strength along the armchair direction are shown in Fig. 4.7(a). In the absence of field strengths, $A(\omega)$ grows linearly with the increase of frequency (by the crosses in Fig. 4.7(a)). It vanishes at $\omega = 0$ and has no special structures. On the other hand, $A(\omega)$ would be strongly modulated in the presence of field strengths. Most of the transition channels from $\mu_n^v \to \mu_{n+1}^c$ ($\nu_n^v \to \nu_{n+1}^c$) leading to the prominent peaks in Fig. 4.6(a) could also result in the conspicuous peaks in the optical absorption spectra (Figs. 4.7(a) and 4.7(b)). However, such optical absorption peaks do not reveal an absolute relation between their height and the field strength. It is noted that some channels corresponding to the inconspicuous peaks in D_J's could exhibit the manifest peaks in the optical absorption spectra, as labeled by the open circles in Fig. 4.7(a). The optical absorption spectra of $V_0 = 0.1\ \gamma_0$ at different modulated periods and at $R_E = 500$ along the zigzag direction are shown in Fig. 4.7(b). $A(\omega)$'s at different R_E's along the armchair direction present similar features to the optical absorption spectra in Fig. 4.7(a). Nevertheless, $A(\omega)$ of the zigzag direction shows different peak frequencies and peak heights from those of the armchair direction, i.e., the anisotropic property in the modulated direction could be reflected by the optical absorption

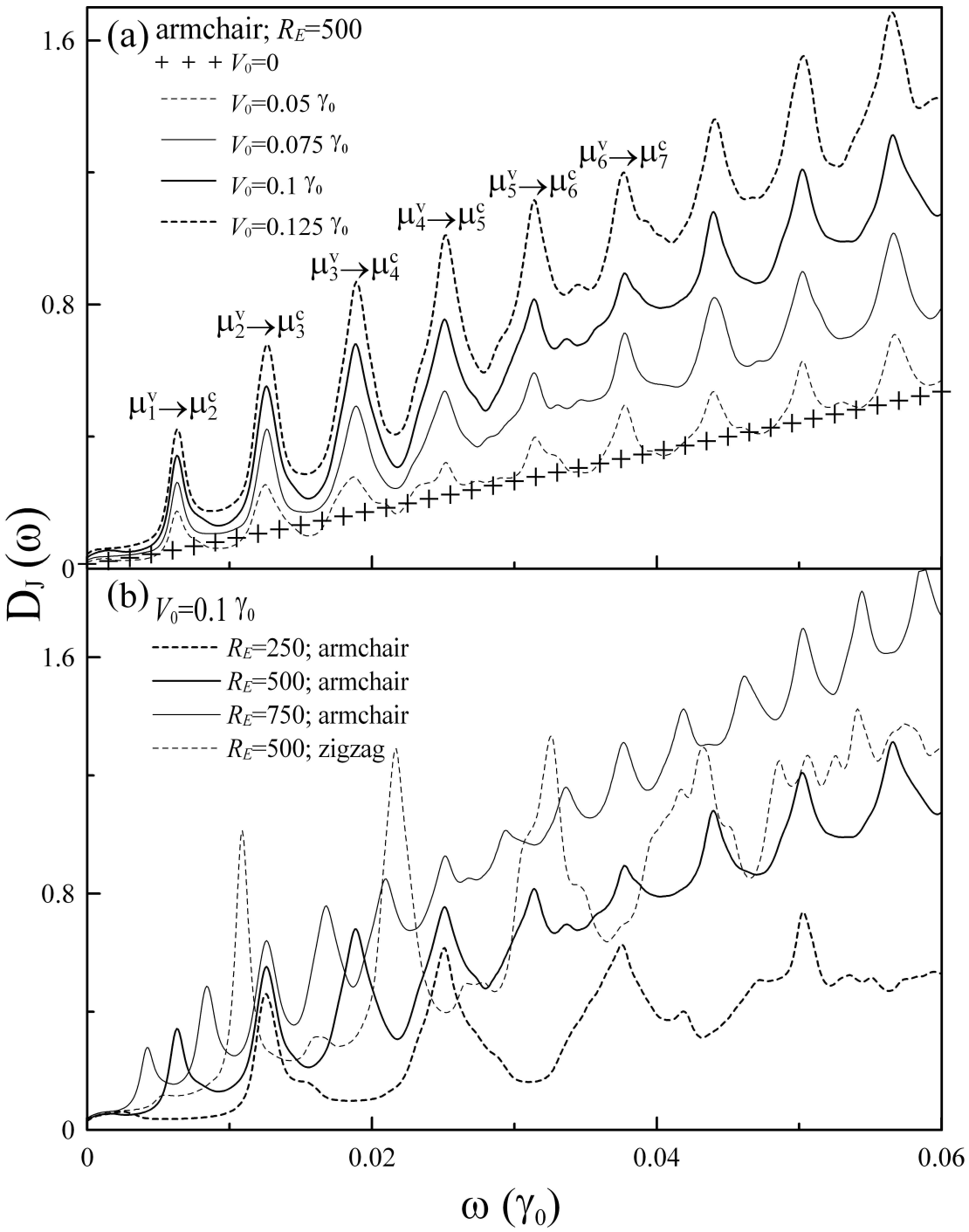

Figure 4.6. The optical joint density of states for a modulated electric field along the armchair direction at (a) $R_E = 500$ and different V_0's; (b) $V_0 = 0.1\ \gamma_0$ and different R_E's. D_J for the zigzag direction is also evaluated at (b) $V_0 = 0.1\ \gamma_0$ and $R_E = 500$.

spectra. Furthermore, the optical absorption spectra for both modulated directions could not indicate a certain selection rule. The fact that the velocity matrix element between two band-edge states does not follow a positive relation with modulated electric fields might cause no obvious selection rules in the optical absorption spectra.

4.5 Conclusions

In summary, the electronic structure and optical absorption spectra of a monolayer graphene in the presence of a modulated electric field are investigated by the tight-binding model and gradient approximation. The low-energy electronic and optical properties are strongly affected by the field strength and period, while the high-energy electronic and optical properties weakly related to those. The similar results are obtained in different modulation directions. The modulated electric field could modify the energy dispersions, destroy the state degeneracy, reduce the dimensionality, create the two kinds of extra band-edge states (μ and ν) about k_y^{pp}, and induce the asymmetry of energy bands. It should be noticed that there are many extra Fermi-momentum states at $E_F = 0$. Density of states exhibits many prominent square-root divergent and inconspicuous peaks. They are, respectively, mainly owing to the μ and ν states. Their frequencies (ω_μ's and ω_ν's) are weakly related to the field strength. On the other hand, ω_μ's display oscillatory dependence on the period, while ω_ν's decrease with the increase of R_E. The finite value of DOS at Fermi level indicates the existence of free carriers. That is to say, a semiconducting graphene monolayer becomes a semimetallic one by applying a modulated electric potential. The free electrons are expected to cause the low-frequency plasmon. The joint density of states presents many conspicuous peaks resulting from the μ and ν states. The peak heights

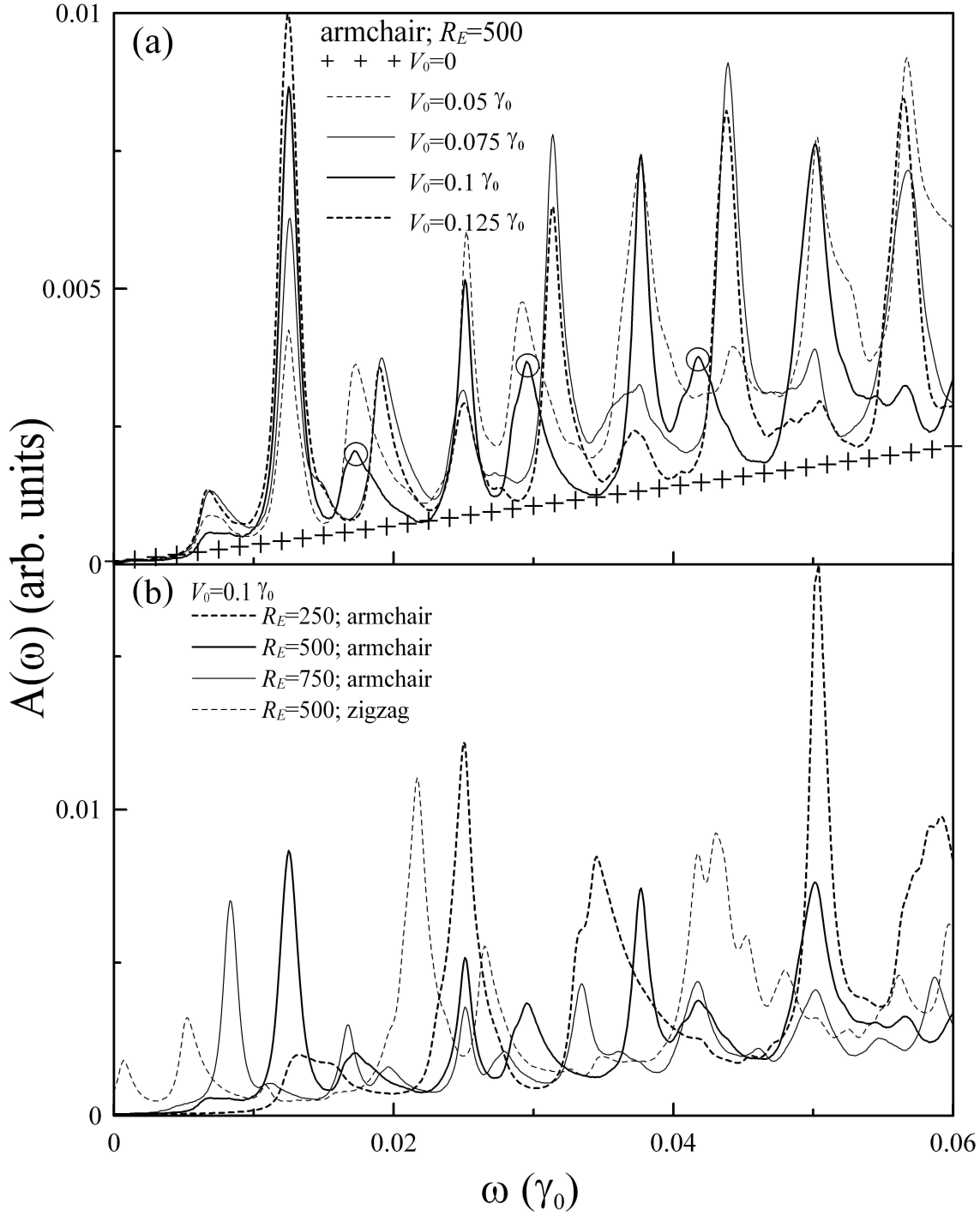

Figure 4.7. Same plot as Fig. 6, but shown for the optical absorption spectra.

originating in the excitations of μ_n^v to μ_{n+1}^c (μ_{n+1}^v to μ_n^c) and ν_n^v to ν_{n+1}^c (ν_{n+1}^v to ν_n^c) are relatively stronger than those of other excitations. The peak intensity is enhanced by the increase of the field strength and period. Most of the prominent peaks in D_J's could also show significant peaks in the optical absorption spectra. Nevertheless, the optical absorption peaks do not have apparent relations with the field strength and period. Such absorption peaks could not be ascribed to an obvious selection rule. It is worth noting that the optical absorption spectra could display the anisotropic feature in the modulation direction. The experiment of energy-loss spectra and optical measurements could be used to verify the above-mentioned theoretical prediction.

References

[1] P. R. Wallace, Phys. Rev. **71**, 622 (1947).

[2] F. L. Shyu, and M. F. Lin, J. Phys. Soc. Jpn. **69**, 607 (2000).

[3] E. J. Duplock, M. Scheffler, P. J. D. Lindan, Phys. Rev. Lett. **92**, 225502 (2004).

[4] F. Ortmann, W. G. Schmidt, F. Bechstedt, Phys. Rev. Lett. **95**, 186101 (2005).

[5] J. M. D. Coey, M. Venkatesan, C. B. Fitzgerald, A. P. Douvalis, and I. S. Sanders, Nature **420**, 156 (2002).

[6] A. Hashimoto, K. Suenaga, A. Gloter, K. Urita, S. Iijima, Nature **430**, 870 (2004).

[7] E. T. Jesen, R. E. Palmer, W. Allison, and J. F. Annett, Phys. Rev. Lett. **66**, 492 (1991).

[8] H. Kempa, P. Esquinazi, and Y. Kopelevich, Phys. Rev. B **65**, 241101 (2002).

[9] Y. Zhang, J. P. Small, M. E. S. Amori, and P. Kim, Phys. Rev. Lett. **94**, 176803 (2005).

[10] K. S. Novoselov, A. K. Geim, S. V. Morozov, D. Jiang, Y. Zhang, S. V. Dubonos, I. V. Grigorieva, A. A. Firsov, Science **306**, 666 (2004).

[11] K. S. Novoselov, A. K. Geim, S. V. Morozov, D. Jiang, M. I. Katsnelson, I. V. Grigorieva, S. V. Dubonos, and A. A. Firsov, Nature **438**, 197 (2005).

[12] C. Berger, Z. M. Song, T. B. Li, X. B. Li, A. Y. Ogbazghi, R. Feng, Z. T. Dai, A. N. Marchenkov, E. H. Conrad, P. N. First, and W. A. de Heer, J. Phys. Chem. B **108**, 19912 (2004).

[13] C. Berger, Z. Song, X. Li, X. Wu, N. Brown, C. Naud, D. Mayou, T. Li, J. Hass, A. N. Marchenkov, E. H. Conrad, P. N. First, and W. A. de Heer, Science **312**, 1191 (2006).

[14] C. P. Chang, C. L. Lu, F. L. Shyu, R. B. Chen, Y. K. Fang and M. F. Lin, Carbon **42**, 2975 (2004).

[15] S. Latil and L. Henrard, Phys. Rev. Lett. **97**, 036803 (2006).

[16] Y. Zheng and T. Ando, Phys. Rev. B **65**, 245420 (2002).

[17] E. McCann, Phys. Rev. B **74**, 161403 (2006).

[18] C. L. Lu, C. P. Chang, Y. C. Huang, J. M. Lu, C. C. Hwang, and M. F. Lin, Journal of Physics: Condensed Matter **18**, 5849 (2006).

[19] F. Guinea, A. H. C. Neto, and N. M. R. Peres, Phys. Rev. B **73**, 245426 (2006).

[20] E. McCann, K. Kechedzhi, V. I. Falko, H. Suzuura, T. Ando, and B. L. Altshuler, Phys. Rev. Lett. **97**, 146805 (2006).

[21] B. Partoens and F. M. Peeters, Phys. Rev. B **74**, 075404 (2006).

[22] M. Koshino and T. Ando, Phys. Rev. B **76**, 085425 (2007)

[23] C. L. Lu, C. P. Chang, J. H. Ho, C. C. Tsai, and M. F. Lin, Physica E **32**, 585 (2006).

[24] J. H. Ho, Y. H. Lai, S. J. Tsai, J. S. Hwang, C. P. Chang, and M. F. Lin, J. Phys. Soc. Jpn. **75**, 114703 (2006).

[25] E. McCann and V. I. Fal'ko, Phys. Rev. Lett. **96**, 086805 (2006).

[26] J. M. Pereira, F. M. Peeters, and P. Vasilopoulos, Phys. Rev. B **76**, 115419 (2007).

[27] N. Nemec and G. Cuniberti, Phys. Rev. B **75**, 201404 (2007).

[28] J. H. Ho, Y. H. Lai, Y. H. Chiu, and M. F. Lin, Nanotechnology **19**, 035712 (2008).

[29] Y. H. Chiu, Y. H. Lai, J. H. Ho, D. S. Chuu, and M. F. Lin, Phys. Rev. B **77**, 045407 (2008).

[30] E. V. Castro, K. S. Novoselov, S. V. Morozov, N. M. R. Peres, J. M. B. Lopes dos Santos, J. Nilsson, F. Guinea, A. K. Geim, and A. H. Castro Neto, Phys. Rev. Lett. **99**, 216802 (2007).

[31] Y. H. Lai, J. H. Ho, C. P. Chang, and M. F. Lin, Phys. Rev. B **77**, 085426 (2008).

[32] F. L. Shyu and M. F. Lin, J. Phys. Soc. Jpn. **69**, 607 (2000).

[33] J. H. Ho, C. P. Chang and M. F. Lin, Phys. Lett. A **352**, 446 (2006).

[34] J. H. Ho, C. L. Lu, C. C. Hwang, C. P. Chang and M. F. Lin, Phys. Rev. B **74**, 085406 (2006).

[35] X. F. Wang and T. Chakraborty, Phys. Rev. B **75**, 041404 (2007).

[36] Y. Zhang, Y. W. Tan, H. L. Stormer, and P. Kim, Nature **438**, 201 (2005).

[37] K. S. Novoselov, Z. Jiang, Y. Zhang, S. V. Morozov, H. L. Stormer, U. Zeitler, J. C. Maan, G. S. Boebinger, P. Kim, and A. K. Geim, Science **315**, 1379 (2007).

[38] K. S. Novoselov, E. McCann, S. V. Morozov, V. I. Fal'ko, M. I. Katsnelson, U. Zeitler, D. Jiang, F. Schedin, and A. K. Geim, Nat. Phys. **2**, 177 (2006).

[39] V. P. Gusynin and S. G. Sharapov, Phys. Rev. B **73**, 245411 (2006).

[40] V. P. Gusynin, V. A. Miransky, S. G. Sharapov, and I. A. Shovkovy, Phys. Rev. B **74**, 195429 (2006).

[41] M. Koshino and T. Ando, Phys. Rev. B 73, 245403 (2006).

[42] J. Nilsson, A. H. Castro Neto, F. Guinea, and N. M. R. Peres, Phys. Rev. Lett. **97**, 266801 (2006).

[43] N. M. R. Peres, F. Guinea, and A. H. Castro Neto, Phys. Rev. B **73**, 125411 (2006).

[44] M. L. Sadowski, G. Martinex, and M. Potemski, C. Berger, and W. A. de Heer, Phys. Rev. Lett. **97**, 266405 (2006).

[45] D. S. L. Abergel and Vladimir I. Fal'ko, Phys. Rev. B **75**, 155430 (2007).

[46] R. S. Deacon, K.-C. Chuang, R. J. Nicholas, K. S. Novoselov, and A. K. Geim, Phys. Rev. B **76**, 081406 (2007).

[47] D. S. L. Abergel, A. Russell, and Vladimir I. Fal'ko, Appl. Phys. Lett. **91**, 063125 (2007).

[48] C. L. Lu, C. P. Chang, Y. C. Huang, R. B. Chen, and M. F. Lin, Phys. Rev. B **73**, 144427 (2006).

[49] C. L. Lu, H. L. Lin, C. C. Hwang, J. Wang, C. P. Chang, and M. F. Lin, Appl. Phys. Lett. **89**, 221910 (2006).

[50] Z. Jiang, E. A. Henriksen, L. C. Tung, Y.-J. Wang, M. E. Schwartz, M. Y. Han, P. Kim, and H. L. Stormer, Phys. Rev. Lett. **98**, 197403 (2007).

[51] M. F. Lin and Kenneth W.-K. Shung, Phys. Rev. B **50**, 17744 (1994).

[52] Y. C. Huang, M. F. Lin, and C. P. Chang, J. App. Phy. **103**, 073709 (2008).

[53] J. Blinowski, N. H. Hau, C. Rigaux, J. P. Vieren, R. L. Toullee, G. Furdin, A. Herold, and J. Melin, J. Phys. (Paris) **41**, 47 (1980).

[54] M. F. Lin, D. S. Chuu, and K. W. -K. Shung, Phys. Rev. B **56**, 1430 (1997).

Chapter 5

Summary and future research

The dissertation aims to investigate the physical properties of a single-layer graphene in the presence of modulated magnetic and periodic electric fields. The π-electronic properties (including the energy dispersions, band-edge states, symmetry of energy bands, changes of degeneracy, reduction of dimensionality, anisotropy of modulated direction, wave functions, and density of states) are calculated by the tight-binding model. The Hamiltonian matrix is very huge for a large period, and becomes a band-like Hamiltonian matrix with a appropriate arrangement of specific base functions. By diagonalizing the band-like Hamiltonian matrix, the energy bands are obtained. The optical absorption spectra are evaluated by the gradient approximation, and they could directly reflect the electronic properties.

In a spatially modulated magnetic field, the magnetoelectronic structure of a graphene monolayer is drastically changed. For the modulated magnetic field along the armchair direction, there are partial flat bands at $E_F = 0$ and parabolic bands at others. The two kinds of bands, respectively, make the density of states exhibit a delta-function-like structure at Fermi level and asymmetric prominent peaks at others. Each parabolic band owns one original band-edge and four extra band-edge states. The strength, period, and direction of a modulated magnetic field dominate the main features of electronic properties. Such a field could reduce dimensionality by one, alter energy dispersions, cause anisotropy at low energy, induce composite behavior in state degeneracy, produce extra band-edge states, and destroy the symmetry of energy bands about the original band-edge state. Energies of the original band-edge state are weakly dependent on the period, while those of the extra

band-edge states are strongly related to the period. Nevertheless, both of them grow with the increase of the strength. As to the zigzag direction, energy bands display different state degeneracies, and DOS shows different peak frequencies and peak intensity. It means that the electronic properties are anisotropic in the modulation direction. In addition, a spatially modulated magnetic field contrasts sharply with a uniform perpendicular magnetic field in energy dispersion, state degeneracy, and dimensionality. The important differences between a single-layer graphene and a 2DEG mainly lie in the partial flat bands at zero energy, dependence on the modulation direction, and wave vectors of band-edge states, which results from the hexagonal symmetry.

The main features of wave functions shed light on understanding the optical absorption spectra. For the armchair direction, the doubly degenerate energy bands close to k_y^{pp} are regarded as the quasi-Landau levels because their wave functions present similar characteristics to those of LLs resulting from a uniform magnetic field, e.g., the same effective quantum number, oscillatory behavior, and distribution width. Concerning the nondegenerate energy bands at k_y^{sp}'s, their wave functions exhibit different features from those of QLLs. The α and β subbands display different spatial symmetries, and their wave functions show overlap behaviors. The different spatial symmetries and overlap behaviors would induce the anisotropic features and extra excitations in the optical absorption spectra. As to the zigzag direction, the characteristics of wave functions are similar to those of armchair direction.

The optical absorption spectra present a plenty of prominent asymmetric peaks. These peaks could be classified into the principal peaks ω_P's and subpeaks ω_S's, which primarily come from the original band-edge and extra band-edge states, respectively. The optical

excitations are strongly affected by the modulated magnetic field and the polarization direction of an EM wave. The peak height of ω_P's grows by increasing the field strength and period. The energy of each principal peak rises with the increase of B, and it would be weakly related to the period as R_B becomes large enough. The selection rule of ω_P's is simply represented by $|\Delta n| = 1$, which is the same with that of the LLs resulting from a uniform perpendicular magnetic field. The underlying cause is that the main features of wave functions at k_y^{pp} resemble those of $\mathbf{B}_0$. Nevertheless, the low-energy absorption spectra of QLLs and LLs still have some differences, e.g., the peak type, peak intensity, and anisotropic behavior. As to the subpeaks, ω_S's could be further divided into two subgroups, ω_S^a's and ω_S^b's, because of the two kinds of subbands α and β. They originate in the excitations of α (β) to β (α) and of α (β) to α (β), respectively. The two kinds of subpeaks are strongly related to the field strength and period. ω_s's display a different selection rule from that of principal peaks, i.e., $|\Delta n| = 1$ and $|\Delta n| = 0$. Such an important difference is mainly owing to the fact that the wave functions overlap at k_y^{sp}'s. The overlap behavior induces the extra excitations with $|\Delta n| = 0$, which is forbidden in the principal peaks. Furthermore, the optical absorption spectra could reveal anisotropy in the modulated direction and electric polarization direction. The selection rule and anisotropic features of the optical absorption spectra originating in a modulated magnetic field are very different from those in a uniform perpendicular magnetic field or in the absence of an external field.

In addition to modulated magnetic fields, modulated electric potentials could also strongly influence the electronic properties of a graphene monolayer. The low-frequency energy bands are drastically changed by a modulated electric field, whereas the high-frequency energy bands weakly dependent on that. The similar results are obtained in different modu-

lation directions. The modulated electric field could modify the energy dispersions, destroy the state degeneracy, reduce the dimensionality, create the two kinds of extra band-edge states (μ and ν) about k_y^{pp}, and induce the asymmetry of energy bands. The two kinds of band-edge states make DOS exhibit the prominent square-root divergent and the inconspicuous peaks. Their peak frequencies (ω_μ's and ω_ν's) are weakly related to the field strength. However, ω_μ's show oscillatory dependence on the period, and ω_ν's diminish with the increase of R_E. It should be noticed that there are many extra Fermi-momentum states at $E_F = 0$. The finite value of DOS at Fermi level corresponding to Fermi-momentum states indicates the existence of free carriers. That is to say, a semiconducting single-layer graphene changes into a semimetallic one by applying a modulated electric potential. The free electrons are expected to result in the low-frequency plasmon.

The optical absorption spectra could reflect the electronic properties. The joint density of states presents many conspicuous peaks resulting from the extra band-edge states. The peak heights originating in the excitations of μ_n^v to μ_{n+1}^c (μ_{n+1}^v to μ_n^c) and ν_n^v to ν_{n+1}^c (ν_{n+1}^v to ν_n^c) are relatively stronger than those of other excitations. The peak intensity is enhanced by the increase of the field strength and period. Most of the prominent peaks in D_J's could also show significant peaks in the optical absorption spectra. However, the optical absorption peaks do not have manifest relations with the field strength and period. These absorption peaks could not be ascribed to an obvious selection rule. It is worth noting that the optical absorption spectra could display the anisotropic feature in the modulation direction.

Related to the single-layer and bilayer graphenes in the presence of external fields, some suggestions for future research are as follows:

(1) electronic properties of a graphene monolayer under a uniform magnetic field and a modulated electric potential.

(2) optical properties of a graphene monolayer under a uniform magnetic field and a modulated electric potential.

(3) optical properties of a graphene monolayer under a uniform magnetic field and a modulated magnetic field.

(4) Coulomb excitations of a graphene monolayer under a modulated magnetic field.

(5) Coulomb excitations of a graphene monolayer under a modulated electric potential.

(6) transport properties of a graphene monolayer under a modulated magnetic field.

(7) transport properties of a graphene monolayer under a modulated electric field.

(8) electronic properties of a bilayer graphene under a modulated magnetic field.

(9) optical properties of a bilayer graphene under a modulated magnetic field.

(10) electronic properties of a bilayer graphene under a modulated electric field.

(11) optical properties of a bilayer graphene under a modulated electric field.

Appendix: Band-like Hamiltonian matrix

For example, a 8×8 real symmetric matrix is expressed as follows

$$A = \begin{pmatrix} 5 & 2 & 1 & 3 & 0 & 0 & 0 & 0 \\ 2 & 6 & 3 & 2 & 3 & 0 & 0 & 0 \\ 1 & 3 & 6 & 4 & 3 & 3 & 0 & 0 \\ 3 & 2 & 4 & 6 & 5 & 4 & 3 & 0 \\ 0 & 3 & 3 & 5 & 6 & 6 & 5 & 3 \\ 0 & 0 & 3 & 4 & 6 & 6 & 7 & 6 \\ 0 & 0 & 0 & 3 & 5 & 7 & 6 & 8 \\ 0 & 0 & 0 & 0 & 3 & 6 & 8 & 5 \end{pmatrix}. \tag{A.1}$$

The matrix elements are denoted as A_{ij}, and symmetric about the diagonal ($A_{ij} = A_{ji}$). All the nonzero elements centralize around the diagonal, and the elements are zero at others. Such a matrix is called as a real symmetric band-like matrix. Because of the symmetry, we can choose the matrix elements above the diagonal (including the diagonal elements) to describe A. The matrix becomes

$$A' = \begin{pmatrix} 0 & 0 & 0 & A_{14} & A_{25} & A_{36} & A_{47} & A_{58} \\ 0 & 0 & A_{13} & A_{24} & A_{35} & A_{46} & A_{57} & A_{68} \\ 0 & A_{12} & A_{23} & A_{34} & A_{45} & A_{56} & A_{67} & A_{78} \\ A_{11} & A_{22} & A_{33} & A_{44} & A_{55} & A_{66} & A_{77} & A_{88} \end{pmatrix} = \begin{pmatrix} 0 & 0 & 0 & 3 & 3 & 3 & 3 & 3 \\ 0 & 0 & 1 & 2 & 3 & 4 & 5 & 6 \\ 0 & 2 & 3 & 4 & 5 & 6 & 7 & 8 \\ 5 & 6 & 6 & 6 & 6 & 6 & 6 & 5 \end{pmatrix}. \tag{A.2}$$

Accordingly, for a $n \times n$ real symmetric band-like matrix, if there are m lines symmetric

about the diagonal (including the diagonal), the matrix can be reduced into a $m \times n$ matrix

$$A' = \begin{pmatrix} 0 & \cdots & \cdots & \cdots & \cdots & A_{1,m} & \cdots & \cdots & A_{n-m+1,n} \\ \vdots & & & & & \vdots & & & \vdots \\ & & & \vdots & & & & & \\ & & \vdots & 0 & \cdots & \vdots & & & \\ \vdots & \vdots & 0 & A_{14} & \cdots & A_{m-3,m} & \cdots & & A_{n-3,n} \\ 0 & 0 & A_{13} & A_{24} & \cdots & A_{m-2,m} & \cdots & \cdots & A_{n-2,n} \\ 0 & A_{12} & A_{23} & A_{34} & \cdots & A_{m-1,m} & \cdots & \cdots & A_{n-1,n} \\ A_{11} & A_{22} & A_{33} & A_{44} & \cdots & A_{m,m} & \cdots & \cdots & A_{n,n} \end{pmatrix}. \tag{A.3}$$

Such a matrix can save much time in our calculations.

In chapter 2, a monolayer graphene is assumed to exist in a spatially modulated magnetic field $\mathbf{B} = B\sin(Kx)\hat{z}$ along the armchair direction. The wave function and the Hamiltonian matrix element are, respectively, given by

$$|\Psi_{\mathbf{k}}\rangle = \sum_{n=1}^{2R_B} C_{a\mathbf{k}}^n |a_{n\mathbf{k}}\rangle + C_{b\mathbf{k}}^n |b_{n\mathbf{k}}\rangle; \tag{A.4a}$$

$$\langle b_{m\mathbf{k}}|H_{\mathbf{B}}|a_{n\mathbf{k}}\rangle = [t_{1\mathbf{k}}(n) + t_{2\mathbf{k}}(n)]\delta_{m,n} + t_{3\mathbf{k}}(n)\delta_{m,n-1}. \tag{A.4b}$$

$C_{a\mathbf{k}}^n = C_{a\mathbf{k}}^{n+2R_B}$ and $C_{b\mathbf{k}}^n = C_{b\mathbf{k}}^{n+2R_B}$ are derived because of the periodical boundary condition. For the three nearest-neighbor atoms, their hopping integrals are, respectively, $t_{1\mathbf{k}}(n) = \gamma_0 \exp[\,(ik_x b'/2 + ik_y\sqrt{3}b'/2) + G_n\,]$, $t_{2\mathbf{k}}(n) = \gamma_0 \exp[\,(ik_x b'/2 - ik_y\sqrt{3}b'/2) - G_n\,]$, and $t_{3\mathbf{k}}(n) = \gamma_0 \exp(-ik_x b'\,)$, where $G_n = -i[6(R_B)^2\Phi/\pi]\cos[\pi(n-5/6)/R_B]\sin(\pi/6R_B)\,]$. The normal arrangement of bases is $\{|a_{1\mathbf{k}}\rangle,\ |b_{1\mathbf{k}}\rangle,\ |a_{2\mathbf{k}}\rangle,\ |b_{2\mathbf{k}}\rangle,\ |a_{3\mathbf{k}}\rangle,\ |b_{3\mathbf{k}}\rangle,\ |a_{4\mathbf{k}}\rangle,\ |b_{4\mathbf{k}}\rangle,\ \ldots\ |a_{2R_B-3\mathbf{k}}\rangle,\ |b_{2R_B-3\mathbf{k}}\rangle,\ |a_{2R_B-2\mathbf{k}}\rangle,\ |b_{2R_B-2\mathbf{k}}\rangle,\ |a_{2R_B-1\mathbf{k}}\rangle,\ |b_{2R_B-1\mathbf{k}}\rangle,\ |a_{2R_B\mathbf{k}}\rangle;\ |b_{2R_B\mathbf{k}}\rangle\}$. The $4R_B \times 4R_B$

Hamiltonian matrix is

$$H = \begin{pmatrix} 0 & p_1 & 0 & 0 & \cdots & \cdots & \cdots & 0 & q \\ p_1^* & 0 & q^* & 0 & 0 & \cdots & \cdots & \cdots & 0 \\ 0 & q & 0 & p_2 & 0 & \ddots & 0 & \cdots & 0 \\ 0 & 0 & p_2^* & 0 & 0 & \ddots & 0 & 0 & 0 \\ \vdots & \ddots & \ddots & 0 & 0 & \ddots & \ddots & \ddots & 0 \\ \vdots & & & & \ddots & & p_{2R_B-1} & \ddots & \vdots \\ \vdots & \ddots & \ddots & \ddots & \ddots & p_{2R_B-1}^* & \ddots & q^* & 0 \\ 0 & \vdots & \vdots & \ddots & \ddots & \ddots & q & \ddots & p_{2R_B} \\ q^* & 0 & 0 & 0 & 0 & \cdots & 0 & p_{2R_B}^* & 0 \end{pmatrix}, \tag{A.5}$$

where $p_n \equiv t_{1\mathbf{k}}(n) + t_{2\mathbf{k}}(n)$ and $q \equiv t_{3\mathbf{k}}$. Most of the matrix elements are centerlized about the diagonal except the two elements $H_{1,2R_B} = q$ and $H_{2R_B,1} = q^*$. To get the band-like Hamiltonian matrix, the base functions are assigned as the following sequence $\{|a_{1\mathbf{k}}\rangle$, $|b_{2R_B\mathbf{k}}\rangle$, $|b_{1\mathbf{k}}\rangle$, $|a_{2R_B\mathbf{k}}\rangle$, $|a_{2\mathbf{k}}\rangle$, $|b_{2R_B-1\mathbf{k}}\rangle$, $|b_{2\mathbf{k}}\rangle$, $|a_{2R_B-1\mathbf{k}}\rangle$, $\ldots$ $|a_{R_B-1\mathbf{k}}\rangle$, $|b_{R_B+2\mathbf{k}}\rangle$, $|b_{R_B-1\mathbf{k}}\rangle$, $|a_{R_B+2\mathbf{k}}\rangle$, $|a_{R_B\mathbf{k}}\rangle$, $|b_{R_B+1\mathbf{k}}\rangle$, $|b_{R_B\mathbf{k}}\rangle$; $|a_{R_B+1\mathbf{k}}\rangle\}$. The Hamiltonian matrix is expressed as

$$\begin{pmatrix} 0 & q^* & p_1^* & 0 & \ldots & \ldots & 0 & 0 \\ q & 0 & 0 & p_{2R_B} & 0 & \ldots & \ldots & 0 \\ p_1 & 0 & 0 & 0 & q & 0 & \ldots & 0 \\ 0 & p_{2R_B}^* & 0 & 0 & 0 & q^* & 0 & 0 \\ \vdots & \ddots & q^* & 0 & 0 & \ddots & \ddots & 0 \\ \vdots & \ldots & \ddots & q & \ddots & \ddots & 0 & p_{R_B+1} \\ 0 & \vdots & \vdots & \ddots & \ddots & 0 & \ddots & q \\ 0 & 0 & 0 & 0 & 0 & p_{R_B+1}^* & q^* & 0 \end{pmatrix}. \tag{A.6}$$

However, the matrix elements are complex number, and this matrix is not a real symmetric band-like matrix. To solve this problem, both the Hamiltonian and wave funtions are divided into the real and imaginary parts, i.e., $H = U + iV$ and $\Psi_{\mathbf{n}} = X + iY$. The relation between the Hamiltonian matrix and eigen energy becomes

$$H\Psi_{\mathbf{n}} = \begin{bmatrix} U & -V \\ V & U \end{bmatrix} \begin{bmatrix} X \\ Y \end{bmatrix} = \begin{bmatrix} Re(H) & -Im(H) \\ Im(H) & Re(H) \end{bmatrix} \begin{bmatrix} X \\ Y \end{bmatrix} = E_n \begin{bmatrix} X \\ Y \end{bmatrix}. \tag{A.7}$$

It implies that the original Hamiltonian matrix elements will be a 2×2 matrix. For example, the matrix element q in Eq. (A.6) is thus represented as $\begin{bmatrix} Re(q) & -Im(q) \\ Im(q) & Re(q) \end{bmatrix}$,

and q^* would be $\begin{bmatrix} Re(q) & Im(q) \\ -Im(q) & Re(q) \end{bmatrix}$. Eq. (A.6) is rewritten as follows

$$\begin{bmatrix}
0 & 0 & q^{Re} & q^{Im} & p_1^{Re} & p_1^{Im} & 0 & \dots & & \dots & 0 \\
0 & 0 & -q^{Im} & q^{Re} & -p_1^{Im} & p_1^{Re} & 0 & \dots & & & \vdots \\
q^{Re} & -q^{Im} & 0 & 0 & 0 & 0 & & & & & \\
q^{Im} & q^{Re} & 0 & 0 & & & & & & & \\
p_1^{Re} & -p_1^{Im} & 0 & 0 & \ddots & & & & & \vdots & \vdots \\
p_1^{Im} & p_1^{Re} & 0 & 0 & \ddots & & & \ddots & & 0 & 0 \\
0 & 0 & & \ddots & \ddots & & & \ddots & 0 & 0 & p_{R_B}^{Re} & -p_{R_B}^{Im} \\
\vdots & \vdots & & & & & & \ddots & 0 & 0 & p_{R_B}^{Im} & p_{R_B}^{Re} \\
 & & & & & & & \ddots & 0 & 0 & q^{Re} & -q^{Im} \\
 & & & & & 0 & 0 & 0 & 0 & 0 & q^{Im} & q^{Re} \\
\vdots & & & & 0 & p_{R_B}^{Re} & p_{R_B}^{Im} & q^{Re} & q^{Im} & 0 & 0 \\
0 & \dots & & & \dots & 0 & -p_{R_B}^{Im} & p_{R_B}^{Re} & -q^{Im} & q^{Re} & 0 & 0
\end{bmatrix}, \quad \text{(A.8)}$$

where the superscripts Re and Im, respectively, indicate the Real and imaginary parts. The $4R_B \times 4R_B$ complex band-like matrix in Eq. (A.6) enlarges to be a $8R_B \times 8R_B$ real symmetric band-like matrix in Eq. (A.8). There are six symmetric lines about the diagonal (including the diagonal) in the matrix, and it can be thus reduced as a $6 \times 8R_B$ matrix.

Publications

A. Referred Papers: (Published or Accepted)

[1] C. W. Chiu, **Y. H. Chiu**, F. L. Shyu, C. P. Chang, D. S. Chuu, and M. F. Lin*, "Temperature-dependent carrier dynamics in metallic carbon nanotubes", Phys. Lett. A **346**, 347-354 (2005).

[2] **Y. H. Chiu**, Y. H. Lai, J. H, Ho, D. S. Chuu†, and M. F. Lin*, "Electronic structure of a two-dimensional graphene monolayer in a spatially modulated magnetic field: Peierls tight-binding model", Phys. Rev. B **77**, 045407 (6) (2008).

[3] **Y. H. Chiu**, Y. H. Lai, J. H. Ho, D. S. Chuu†, and M. F. Lin*, "Magnetic energy bands of a 2D graphite layer in the spatially modulated magnetic field", Physica E, (2008) (accepted).

[4] J. H. Ho, Y. H. Lai, **Y. H. Chiu**, and M. F. Lin*, "Landau levels in graphene", Physica E, (2008) (accepted).

[5] J. H. Ho, Y. H. Lai, **Y. H. Chiu**, and M. F. Lin*, "Modulation effects on Landau levels in a monolayer graphene", Nanotechnology **19**, 035712 (6) (2008).

[6] **Y. H. Chiu**, J. H. Ho, C. P. Chang, D. S. Chuu†, and M. F. Lin*, "Low-frequency magneto-optical excitations in a monolayer graphene", (submitted to Phys. Rev. B).

[7] J. Y. Wu†, **Y. H. Chiu**, J. Y. Lien, and M. F. Lin*, "The effects of the modulated magnetic fields on electronic structures of graphene nonoribbons", (submitted to Journal of Nanoscience and Nanotechnology).

B. Conference Papers: (Published or Accepted)

[1] J. H. Ho, Y. H. Lai, **Y. H. Chiu**, S. J. Tsai, and M. F. Lin*, "Landau levels of graphene", **The 17th International Conference on the Electronic Properties of Two-Dimensional Systems** (2007).

[2] **Y. H. Chiu**, Y. H. Lai, J. H. Ho, M. F. Lin*, and D. S. Chuu, "Magnetic energy bands of a 2D graphite layer in the spatially modulated magnetic field", **The 13th International Conference on the Modulated Semiconductor Structures** (2007).

[3] **Y. H. Chiu**, Y. H. Lai, J. H. Ho, D. S. Chuu, and M. F. Lin*, "Electronic structure of a 2D monolayer graphene in a spatially modulated magnetic field", **Annual Meeting of the Physical Society of the ROC** (2008).